University of Alberta

Application of spectral mixture analysis to hyperspectral imagery for lithological mapping

by

Derek M. Rogge

A thesis submitted to the Faculty of Graduate Studies and Research
in partial fulfillment of the requirements for the degree of

Doctor of Philosophy

Department of Earth and Atmospheric Sciences

Edmonton, Alberta
Spring, 2007

Library and
Archives Canada

Published Heritage
Branch

395 Wellington Street
Ottawa ON K1A 0N4
Canada

Bibliothèque et
Archives Canada

Direction du
Patrimoine de l'édition

395, rue Wellington
Ottawa ON K1A 0N4
Canada

Your file Votre référence
ISBN: 978-0-494-29729-2
Our file Notre référence
ISBN: 978-0-494-29729-2

NOTICE:
The author has granted a non-exclusive license allowing Library and Archives Canada to reproduce, publish, archive, preserve, conserve, communicate to the public by telecommunication or on the Internet, loan, distribute and sell theses worldwide, for commercial or non-commercial purposes, in microform, paper, electronic and/or any other formats.

The author retains copyright ownership and moral rights in this thesis. Neither the thesis nor substantial extracts from it may be printed or otherwise reproduced without the author's permission.

AVIS:
L'auteur a accordé une licence non exclusive permettant à la Bibliothèque et Archives Canada de reproduire, publier, archiver, sauvegarder, conserver, transmettre au public par télécommunication ou par l'Internet, prêter, distribuer et vendre des thèses partout dans le monde, à des fins commerciales ou autres, sur support microforme, papier, électronique et/ou autres formats.

L'auteur conserve la propriété du droit d'auteur et des droits moraux qui protège cette thèse. Ni la thèse ni des extraits substantiels de celle-ci ne doivent être imprimés ou autrement reproduits sans son autorisation.

In compliance with the Canadian Privacy Act some supporting forms may have been removed from this thesis.

While these forms may be included in the document page count, their removal does not represent any loss of content from the thesis.

Conformément à la loi canadienne sur la protection de la vie privée, quelques formulaires secondaires ont été enlevés de cette thèse.

Bien que ces formulaires aient inclus dans la pagination, il n'y aura aucun contenu manquant.

Canada

University of Alberta

Library Release Form

Name of Author: Derek Michael Rogge

Title of Thesis: Application of spectral mixture analysis to hyperspectral imagery for lithological mapping

Degree: Doctor of Philosophy

Year this Degree Granted: 2007

Permission is hereby granted to the University of Alberta Library to reproduce single copies of this thesis and to lend or sell such copies for private, scholarly or scientific research purposes only.

The author reserves all other publication and other rights in association with the copyright in the thesis, and except as herein before provided, neither the thesis nor any substantial portion thereof may be printed or otherwise reproduced in any material form whatsoever without the author's prior written permission.

Signature

January 16th, 2007

ABSTRACT

Hyperspectral reconnaissance mapping methods have become attractive to geological surveys to address the time intensive process of producing regional geological maps for Arctic regions. These sensors can discriminate spectral features associated with common rock-forming and alteration minerals. Three topics relevant to the analysis of such data are addressed in this thesis: 1) image endmember extraction; 2) spectral mixture analysis (SMA); and, 3) generation of a predictive lithological map.

Most of the previous work that deals with image endmember extraction discriminates between pixels using spectral characteristics alone, ignoring their spatial characteristics. High contrast endmembers are easy to identify, whereas low contrast endmembers are more problematic. Improving the potential for identification of low contrast endmembers can be accomplished by analyzing a scene using spatial subsets, thus, taking advantage of the relative spectral contrast between endmembers within a given subset region. Spatial spectral endmember extraction (SSEE) was applied to hyperspectral data and successfully extracted physically significant low contrast endmembers that were not selected by other well known spectral-based methods.

Fractional abundances predicted for a given pixel using SMA are most accurate when only the endmembers that comprise it are used, with larger errors occurring if inappropriate endmembers are included in the mixing process. To address this problem an iterative implementation of SMA (ISMA) was developed to optimize per-pixel endmember sets. ISMA was tested using simulated data with results showing lower abundance errors compared with that of published unmixing methods. ISMA was also

effective at obtaining abundance fractions that are physically realistic for a real hyperspectral data set.

A remote predictive lithological map was generated for an area in southern Baffin Island, which comprises a diverse selection of rock types and represents a typical arctic environment with extensive lichen cover. This was accomplished by applying SSEE and ISMA to generate fractional abundance maps, which were subsequently combined into a single map. The predictive map correlates well with the existing published map, including more extensive exposures of potentially economic peridotite and carbonate units. This work also showed that lichen-rock mixtures could be used to map quartzofeldspathic units that have thick lichen coatings.

Acknowledgments

I would like to acknowledge first and foremost my supervisor Dr. Benoit Rivard, for his constant support, encouragement, insight, availability, flexibility and thoughtful criticism during the course of my degree. I would also like to thank him for the opportunities he has made available to me, from working at the Flight Research Laboratory (National Research Council of Canada) to hiking the barren arctic wilderness.

There are several other individuals I would like to acknowledge for their support. From the Geological Survey of Canada, Dr. Jeff Harris, for his logistical support and comments on my research. Dr. George Leblanc, at the Flight Research Laboratory, for his early support and scientific insight. At the EOSL I would like to particularly acknowledge Dr. Arturo Sánchez-Azofeifa, Dr. Jinkai Zhang, and Dr. Jilu Feng for their input and constructive suggestions throughout my research. Dr, Terry Caelli for his knowledge of computer vision that helped me develop some of my research ideas. Dr. Tom Chacko for his mineralogical expertise. Thank-you also to my family and friends for their continued support.

Lastly, I would like to acknowledge the GEOIDE (GEOmatics for Informed DEcisions) Network of Centres of Excellence of Canada and the National Science and Engineering Research Council of Canada for their financial support of this research. Dr. Karl Staenz of the Canada Center for Remote Sensing for access to ISDAS; Dr. M. St-Onge and Dr. Dave Scott of the Geological Survey of Canada for their help in gaining a better understanding of the geology of the southern Baffin Island; and, Michael Peshko for allowing me to be part of the Baffin Island Hyperspectral Survey.

Table of Contents

List of Tables

List of Figures

List of Abbreviations

Chapter 1: Introduction

1.1 Thesis goal and objectives 1

1.2 Background 1

1.3 Key research avenues 3

1.3.1 Spatial-spectral endmember extraction 3

1.3.2 Iterative spectral mixture analysis 4

1.3.3 Predictive geological mapping 4

1.4 Thesis outline 4

REFERENCES

Chapter 2: Spatial-spectral integration for extraction of low spectral contrast endmembers

2.1 Introduction 10

2.2 PPI, IEA and AMEE algorithms 12

2.3 Description of the spatial-sepctral endmember extraction algorithm 14

2.3.1 SSEE step 1 14

2.3.2 SSEE step 2 15

2.3.3 SSEE step 3 15

2.3.4 SSEE step 4 16

2.4 Data sets and testing methodology 17

2.4.1 Cuprite data set 17

2.4.2 Cuprite testing methodology 18

2.4.3 Baffin data set 18

2.4.4 Baffin Island testing methodology 18

2.5 Results 20

2.5.1 Cuprite 20

2.5.2 Baffin Island 23

2.6 Discussion 29

2.6.1 SSEE parameters, processing speed and performance 29

2.6.2 Comparison with PPI 30

2.6.3 Local vectors versus local candidate pixels 31

2.7 Conclusions 31

REFERENCES

Chapter 3: Iterative spectral unmixing for optimizing per-pixel endmember sets

3.1 Introduction 35

3.2 Background 36

3.3 Iterative spectral mixture analysis 38

3.4 Testing methodology 39

3.5 Hyperspectral data sets 41

3.5.1 Simulated data set 41

3.5.2 AVIRIS Cuprite hyperspectral data set 41

3.6 Results 42

3.6.1 Example for 1 mixture 42

3.6.2 Results for simulated data 43

3.6.2.1 RMS profile characteristics 43
3.6.2.2 Proportion of correctly selected endmembers 43
3.6.2.3 Average fractional abundance errors 45
3.6.2.4 Dependency of the error on the number of endmembers in the mixture 46
3.6.2.5 Dependency of the error on multiple endmembers for the same mineral 46
3.6.3 Results for the AVIRIS Cuprite data set 49
3.7 Discussion 50
3.8 Conclusions 56
REFERENCES

Chapter 4: Application of hyperspectral data for remote predictive lithological mapping, Baffin Island, Canada

4.1 Introduction 61
4.2 Study area 62
4.3 Hyperspectral data set 63
4.4 Generating a remote predictive lithological map 64
4.4.1 Spectral mixture analysis 64
4.4.2 Endmember extraction 66
4.4.3 Predictive map generation 67
4.5 Results 67
4.5.1 Image endmember set and spectral identification 67
4.5.2 Fractional abunadance and maps 72
4.5.3 Predictive lithological maps 73

4.6 Discussion 75

4.6.1 Quality of geological endmembers 75

4.6.2 Lichen and mixture as endmembers 76

4.6.3 Mapping with abundance fractions 76

4.6.4 Spectroscopic imaging 76

4.6.5 Economic context 77

4.7 Conclusions 77

REFERENCES

Chapter 5: Conclusions

5.1 Summary and Contributions 83

5.2 Avenues for future work 85

REFERENCES

List of Tables

Chapter 2:

Table 2.1 Result details for demonstration 1: Cuprite data. 20

Table 2.2 Endmember classes derived from SSEE and IEA candidate endmember spectra and PPI representative spectra for different k and t. 24

Chapter 3:

Table 3.1 List of endmember spectra (from USGS Spectral Library (Clark et al., 1993)) used to generate the simulated data set. Minerals with multiple endmembers (EM) spectra are in bold. 42

Table 3.2 Average number of endmembers selected, proportion correctly selected, and average number of endmembers missed for ISMA and the method given in (Ramsey and Christensen, 1998). Values are reported as averages for all mixtures at a given SNR. 44

Chapter 4:

Table 4.1 Details of image endmembers with best corresponding field and laboratory spectra. 71

List of Figures

Chapter 1:

Figure 1.1 Examples of absorption features for common rock forming minerals in the 500 – 2500 nm range of the electromagnetic spectrum. 2

Chapter 2:

Figure 2.1 2-dimensional scatterplot of endmember assemblage A, B, and C (A); and, B, C, and D (B) located at the vertices of the simplex. In (A) all other pixels (black dots) can be represented as a linear mixture of the 3 endmembers with pixel M an equal mixture of A, B, and C. The relative spectral contrast for C changes for the 2 assemblages, whereby C has an equivalent contrast with A and B in assemblage 1 and a lower contrast in assemblage 2. 10

Figure 2.2 (A) Image region showing three endmembers (i, j, and k), where mixing occurs between i and k, j and k, but not i and j. Spatial groups shown with dotted square in (A). (B) 2-dimensional scatter-plot where endmembers i and j are difficult to discriminate. (C) and (D) show scatter-plots for the two spatial group allowing for better discrimination of endmembers i and j. Dotted lines in (B), (C), and (D) are the eigenvectors related to the largest eigenvalue for each distribution. 12

Figure 2.3 SSEE step 1: (A) Image region showing three image components (i, j, and k). (B) Four image subsets. (C) Compiled basis vectors from all subset shown in (B). 14

Figure 2.4 SSEE step 2: (A) Image region showing three image components (i, j, and k). (B) Image data in 2-D space. (C) Projection of entire image data onto 1 of the eigenvectors derived from step 1. (D) Spatial distribution of candidate endmember pixels. 15

Figure 2.5 SSEE step 3: (A) Candidate endmember pixels showing spatial distribution with respect to units i, j, and k. (B) Updated candidate endmember pixels. (C) Spatial averaging process using a sliding window centered on each updated candidate endmember pixel. (D) Spectral distribution in 2-D space for bands x and y. (E) First iteration of spatial-spectral averaging. Averaged pixels shown as solid lines, with original pixels shown as dashed circles. Pixel number 2 (see C) is averaged with 1 and 3, but not 4, which is averaged with pixel 3. (F) Second iteration of spatial-spectral averaging of pixel 2, which now takes into account the influence of pixel 4 on 3, thus, condensing the spectral cluster further. Continued iterations will compress endmembers i and j into clusters with negligible variance, which now represent two distinct spectral endmembers. Note that for endmember k, only two pixels are average as the third pixel is outside the averaging window. 16

Figure 2.6 Subset region of Airborne Visible/Infrared Imaging Spectrometer (AVIRIS) hyperspectral data over Cuprite, Nevada. 17

Figure 2.7 Regional geology of south-western Baffin Island and enlargement of local geology of the study area (1:100 000) (modified from St-Onge et al., 1999). Hyperspectral data shown at far right with field locations shown as white circles. Note only the area above the dotted line was used in this study. 19

Figure 2.8 Endmember spectra derived from SSEE using a subset size of 20x20 and an s value of 0.01. Refer to Table 1 for endmember abbreviations. 21

Figure 2.9 Fractional abundance maps for the 12 endmembers derived from SSEE using a subset size of 20x20 and an s value of 0.01. 22

Figure 2.10 Thirty endmember classes derived from the SSEE endmember candidate library spectra (solid line) and equivalent IEA endmember (dashed line), when available. 25

Figure 2.11 SSEE rock and lichen-rock endmember classes (solid line) with best matching field spectra. 27

Figure 2.12 Fractional abundance maps for rock 5, 6, 12, and 13; and, lichen-rocks 3 and 4. For rocks 5, 6, and 13 boxes highlight occurrences. Note high abundance is given as black, whereas low abundance is white. This is necessary to visualize the rock endmembers. 28

Chapter 3:

Figure 3.1 Schematic representation of the ISMA. Input data sets include the hyperspectral image and the derived image endmember set. Steps 1 through 8 are applied pixel by pixel. Part 1 (steps 1 through 4) of the ISMA iteratively removes endmembers from the pixel endmember set based on minimum abundance until only 1 endmember and shade remain. Part 2 (steps 5 through 8) of the ISMA determines the critical iteration from the RMS profile generated in Part 1. The optimal pixel endmember set is used to unmix the given pixel spectrum, with results for all pixels output as endmember fractional abundance images. 40

Figure 3.2 Graphical representation of the RMS error as a function of the number of iterations for a mixture of 5 endmembers (A) showing critical point at iteration 25 (it_{25}) and local minima at it_{27}-it_{28} (C). Note the RMS variability for the early iterations where an excess of endmembers are used to unmix the given mixture. (B) and (D) show a comparison between actual endmember abundance (solid line) and estimated abundance for it_1 (all endmembers) and it_{25} (critical point), respectively. Note negative and false positive abundances in (B) for the endmember set used in it_1, which is equivalent to results from an unconstrained unmixing using the 29 available endmembers and shade listed in Table 1. Note that the abundances using the endmembers at it_{25} (D) are within <0.01 of the actual fractions and sum to 0.98. 44

Figure 3.3 Average RMS profile for all mixtures at SNR of 100:1, 50:1, 25:1, and 12:1. On average each pixel can be effectively modeled with 3 to 4 endmembers. 45

Figure 3.4 Average fractional abundance error between actual and estimated abundances for all endmembers and pixels calculated for the method of [29] (R&C 1998); constrained and unconstrained (inset) unmixing using all 30 endmembers; and, the ISMA. 46

Figure 3.5 Average fractional abundance error at a SNR of 50:1 for each endmember for all mixtures for the method of [29] (R&C 1998); constrained and unconstrained unmixing using all endmembers; and the ISMA. The inset includes results for the unconstrained unmixing approach. Refer to Table 1 for the mineral corresponding to the endmember number. 47

Figure 3.6 Selection of endmember spectra with differing spectral contrast. Endmembers with numerous spectral features (almandine, alunite, zoisite) result in low fractional abundance errors (Figure 5), whereas high fractional abundance error is associated with endmembers with few spectral features (albite, anorthite, quartz). 47

Figure 3.7 Histograms distribution of the sum of fractional abundances obtained from the ISMA for each of the 10000 mixtures at SNR of 100:1, 50:1, 25:1, and 12:1. 48

Figure 3.8 Average fractional abundance error as a function of the number of endmembers in a given mixture for SNR of (a) 100:1, (b) 50:1, (c) 25:1, and (d) 12:1. Unconstrained unmixing included in inset of (a) for SNR of 100:1. 48

Figure 3.9 Average fractional abundance error for mixtures containing multiple endmembers for the same mineral (refer to Table 1). Act=actinolite, cal=calcite, goe=goethite, kao=kaolinite, mus=muscovite. 49

Figure 3.10 Selected endmember fractional abundance maps for a subset of the image. Fully constrained unmixing (left column), ISMA (right column). (A) Chalcedony 1, (B) Kaolinite, (C) Alunite 1, (D) Buddingtonite, (E) Chalcedony 2, (F) Montmorillonite, (G) Alunite 2, (H) desert varnish. Images are linearly stretched from 0 – 0.5. 51

Figure 3.11 Histogram showing the distribution of total fractional abundance (excluding shade) for fully constrained and ISMA unmixing methods using the Cuprite hyperspectral data. 52

Figure 3.12 Histograms of fractional abundance values for each endmember for fully constrained (A) and ISMA (B) unmixing results of the Cuprite data set. Note vertical and horizontal scales are different for the two plots. 52

Figure 3.13 Scatter plots of fractional abundances obtained using fully constrained unmixing (left column) and ISMA (right column). (A) Kaolinite and Alunite 1; (B) Alunite 1 and 2; (C) Chalcedony 1 and 2 (refer to figure 10). Note the vertical and horizontal scales in the left and right columns and ISMA results that include a few negative and > 1 values. 53

Chapter 4:

Figure 4.1 Regional geology of south-western Baffin Island and zoom of local geology of the study area (1:100 000) (modified from St-Onge et al., 1999). 63

Figure 4.2 Probe I hyperspectral data of the study area. Circles represent ground locations for field spectra and sample collection. 64

Figure 4.3 Schematic representation of processing steps involved in generating fractional abundance maps using SMA (Step 1), and subsequent steps to generate a predictive geological map (Step 2). 66

Figure 4.4 Reflectance spectra of snow, water, vegetation, and lichen endmembers. Blank areas represent bands excluded owing to noise or water absorption features. 68

Figure 4.5 Geological image endmember spectra (solid line in each graph) and best corresponding sample field/laboratory spectra. Refer to Table 1 for details about sample spectra. Blank areas represent bands excluded owing to noise or water absorption features. 70

Figure 4.6 Lichen image endmember spectra (solid line) and best corresponding sample field/laboratory spectra. Blank areas represent bands excluded owing to noise or water absorption features. 72

Figure 4.7 Fractional abundance maps for vegetation 1 (A), vegetation 2 (B), vegetation 3 (C), and lichen (D) endmembers. Black – low abundance; white – high abundance. Images are linearly scaled to best show abundance variation and spatial distribution. 73

Figure 4.8 Fractional abundance maps for peridotite 1 and 2 (A, B), Fe oxide/hydroxide (C), varnish (D), metased 1 - 3 (E - G), c.g. quartzite/granite (H), carbonate 1 and 2 (I, J), and lichen-rock mixtures 1 and 2 (K, L) endmembers. Black – low abundance; white – high abundance. Images are linearly scaled to best show abundance variation and spatial distribution. 74

Figure 4.9 Predictive geological map showing all eleven geological endmember units (A); units of economic interest shown separately (B); the existing 1:100 000 geological map (St-Onge et al., 1999) (C); and, (D) predictive map with units grouped for comparison with the existing 1:100 000 geological map (e.g. metased 1, 2, 3, and c.g. quartzite/granite grouped into 1 unit representing the psammite, semipelite, monzogranite-tonalite unit (yellow)). 75

List of Abbreviations

AMEE	*Automated morphological endmember extraction*
ANC	*Abundance non-negative*
ASC	*Abundance sum to 1*
ASD	*Analytical spectral devices*
AVIRIS	*Airborne Visible/Infrared Imaging Spectrometer*
CCA	*Convex cone analysis*
CCRS	*Canadian Centre for Remote Sensing*
EM	*Endmember*
FIPPI	*Fast iterative pixel purity index*
GSC	*Geological Survey of Canada*
HyMap	*Hyperspectral mapper*
ICE	*Iterated constrained endmembers*
IEA	*Iterative error analysis*
ISDAS	*Imaging Spectrometer Data Analysis System*
ISMA	*Iterative spectral mixture analysis*
PCA	*Principle component analysis*
PPI	*Pixel purity index*
MESMA	*Multiple endmember spectral mixture analysis*
MEST	*Manual endmember selection tool*
MNF	*Minimum noise fraction*
ORASIS	*Optical real-time adaptive spectral identification system*
RMS	*Root mean square*

SSEE	*Spatial spectral endmember extraction*
SMA	*Spectral mixture analysis*
SNR	*Signal to noise ratio*
SPA	*Sequential projection algorithm*
SVD	*Singular value decomposition*
SWIR	*Short wave infrared*
TM	*Thematic mapper*
USGS	*United States Geological Survey*
VCA	*Vertex component analysis*
VIS	*Visible*
VNIR	*Visible and near-infrared*
WNNLS	*Weighted non-negative least squares approach*
XRD	*X-ray diffraction*

CHAPTER 1
INTRODUCTION

1.1 Thesis goal and objectives

The main goal of my research is to advance the analysis of hyperspectral imaging data for lithological identification and mapping in the Canadian Arctic. The research objectives focus on methodological limitations relating to spectral unmixing and image endmember extraction; and, the process of generating a predictive lithological map. This research, although focusing on regional lithological mapping in the Arctic, should also be beneficial to mineral exploration, land cover surveys, environmental monitoring, and forestry.

1.2 Background

The use of remotely sensed data for lithological mapping is not new. Data types used include air photos, airborne electro-magnetic, synthetic aperture radar, radiometric, and reflectance and thermal imagery. With respect to reflectance imagery (~ 400 – 2500 nm), multi-spectral systems have been in use since the early 1980's (e.g. Podwysocki et al., 1983; Smith et al., 1985; Sultan et al., 1987; Griffiths et al., 1987; Kaufmann, 1988; and Loughlin, 1991). These systems comprise a limited number of broad spectral channels, which can only be used to distinguish between broad lithological units (e.g. fe-rich and fe-poor) using simple analysis methods, such as band ratios (Sabins, 1999). However, identifying specific minerals or rock types is not possible with the limited spectral information available with these types of sensors. Unlike multispectral sensors, such as the Landsat TM satellite which has 7 broad spectral bands, hyperspectral sensors collect data over hundreds of contiguous channels with spectral resolution on the order of 10 - 20 nm. This allows for a greater ability to identify specific spectral features, such as absorption features associated with particular elements or molecules (e.g. Fe^{2+}, Fe^{3+}, Cr^{3+}, Ti^{4+}, H_2O, OH, Al-OH, Mg-OH, Fe-OH, CO_3, HSO_4) found in common rock-forming minerals (Figure 1.1) (e.g. Hunt, 1977; Clark et al., 1990; Vitorello and Galvao, 1996). Hyperspectral systems are becoming increasingly available for lithological mapping, where potential cost savings, large aerial coverage, and relatively quick map production, make the data particularly attractive.

Lithological mapping methods using hyperspectral data include unsupervised classification (e.g. ISO Data and K-means clustering), supervised classification (e.g. minimum distance, parallelepiped, maximum likelihood), neural networks, spectral angle, and spectral mixture analysis (SMA) (Richards, 1999). These mapping methods, excluding SMA, analyze each pixel and assign it to a single class based on a set of criteria. Such approaches are useful for determining the dominant per-pixel land cover type. However, from a lithological mapping perspective locating all pixels that contain rock, regardless of the amount, is critical to producing accurate lithological maps. For this reason the above methods can adversely result in large areas of a classified image showing no lithological information. To get around this problem the analysis must focus on obtaining information at a scale below that of a pixel footprint, which is possible with SMA.

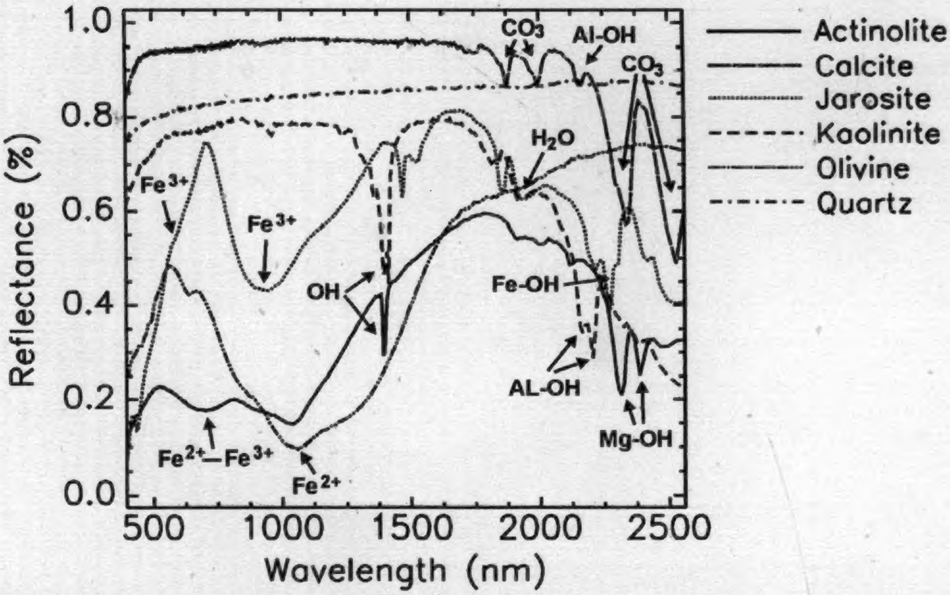

Figure 1.1 Examples of absorption features for common rock forming minerals in the 500 – 2500 nm range of the electromagnetic spectrum. Mineral spectra taken from the USGS spectral library (Clark et al., 1993).

The ability of SMA (Adams et al., 1986; Adams et al., 1993) to obtain sub-pixel information is possible owing to the common characteristic of spectral mixing found in remote sensing data. Spectral mixing, which is caused by the combined measured reflectance of components within the sensors field of view, results in few image pixels containing "pure" spectra (Settle, 1993). SMA addresses the problem of spectral mixing by deconvolving each pixel spectra into abundance fractions of its surface constituent components, or end member spectra. This approach allows the user to obtain approximate proportions of certain surface components (e.g. rock units) for each pixel and generate a classified image for those surface components. Examples of SMA for lithological mapping can be found in studies by Mustard and Pieters (1987), Kruse et al (1990), Zmudio and Atkinson (1990), Blount et al (1990), Murphy (1995), Bierwirth et al (1999), Asner and Heidebrecht (2002), and Neville et al. (2003).

To obtain accurate sub-pixel fractional abundances, SMA requires a set of endmember spectra that are representative of the various surface components within the given scene. Endmembers can be taken from existing spectral libraries, acquired in the field, or extracted from the image itself. Image endmembers are commonly used because they have the advantage of being directly associated with surface components within the scene, whereas available field spectra are not necessarily acquired under the same conditions as airborne or satellite image data and important surface components may not be represented. For this reason much work has been presented in the literature with respect to extracting image endmembers (e.g. Boardman et al., 1995; Bateson and Curtiss, 1996; Winter, 1999; Bowles et al., 1995; Ifarraguerri and Chang, 1999; Neville et al., 1999; Plaza et al., 2002; Berman, et al., 2004; Nascimento and Dias, 2005; Chang and Plaza, 2006). Many of these approaches focus on convex geometry, where endmembers represent the vertices of a simplex in n-dimensional space. These endmember spectra may represent "pure" materials, or they may be spectra that represent a mixture at some more fundamental scale (Adams and Gillespie, 2006). This means that depending on the scale of the sensor endmembers for the same scene may vary. This has direct implications for lithological mapping, where the resulting fractional abundance maps may include endmembers that represent a mineral, a rock unit comprising several minerals, or a mixture of lithological and non-lithological materials such as a granite with partial lichen coating.

1.3 Key research avenues

The research presented in this thesis considers specific limitations of existing SMA algorithms and image endmember extraction tools. For SMA, the ways in which the algorithms use an image endmember set to unmix the pixels in an image is examined. For image endmember extraction, the tools presented in the literature primarily make use of traditional techniques in spectroscopy, which rely on the spectral domain. Thus, the tools ignore the inherent spatial information available within a given scene when searching for endmembers. Lastly, the fractional abundance maps resulting from SMA, although useful, are more practical for lithological mapping if they are presented in a format that is similar to existing lithological maps. The following gives a brief overview of the key research avenues identified in this thesis.

1.3.1 Spatial-spectral endmember extraction

The majority of image endmember extraction tools listed in section 1.2 search for endmembers independently of their spatial characteristics. For the spectral-based methods the ability to successfully extract endmembers hinges on the degree of spectral contrast between them. Thus, endmembers that are spectrally similar can be difficult to distinguish and may result in only one being selected, or the two being represented by a single averaged spectrum. This can have a negative impact on our ability to accurately map the distribution of geological units in a given region, specifically if the units differ only in small variations in mineralogy, but are significant with respect to obtaining an accurate geological interpretation of an area.

Chapter 2 explores how spatial information can be integrated into the search for endmembers. Spectral contrast can be considered variable depending on the spatial neighborhoods, where for each neighborhood the assemblage of endmembers may change. By focusing on image subsets we can take advantage of the spatial characteristics of each endmember, which may then result in a given endmember having higher spectral contrast in a specific image subset, thus facilitating its extraction. A spatial-spectral endmember extraction tool (SSEE) is presented in this chapter and is demonstrated using an Airborne Visible/Infrared Imaging Spectrometer (AVIRIS) scene of Cuprite, Nevada, which is available free of charge through the United States Geologial Survey (USGS) website. SSEE is also demonstrated using Probe I hyperspectral data of an area in southern Baffin Island, which was made available by the Geological Survey of Canada (GSC). The resulting endmembers extracted from the Baffin cube are compared with two well known spectral-based extraction tools to test whether SSEE is capable of extracting similar endmembers, but also unique endmembers that show subtle spectral variability with physical significance.

1.3.2 Iterative spectral mixture analysis

Spectral unmixing has been shown to be a useful tool for geological mapping. However, in many images the number of lithological and non- lithological endmembers can vary substantially (Gillespie, 1992) depending on the spectral complexity of a scene, the spatial scale, spectral resolution, and the number of bands in the image. Commonly this number is greater than the number of endmembers required to unmix any given pixel in the scene. Abundances predicted using linear SMA are most accurate when only the endmembers that comprise a given pixel are used, with larger abundance errors occurring when either too few or too many endmembers are used (Heinz and Chang, 2001; Sabol et al., 1992). Chapter 3 addresses this characteristic of spectral unmixing and develops a novel approach that optimizes per-pixel endmember sets using an iterative approach, such that abundance errors are reduced. The iterative spectral mixture analysis (ISMA) algorithm was tested on a simulated hyperspectral cube to verify the methods ability to improve unmixing errors compared with other published unmixing algorithms. ISMA was also run on the AVIRIS Cuprite data set to demonstrate that the method can also produce realistic abundance fractions using real hyperspectral data.

1.3.3 Predictive lithological mapping

The overall objective of this thesis is to demonstrate the usefulness of hyperspectral data for lithological mapping in the Arctic environment. This environment is known for extensive lichen cover, which presents a challenge for lithological remote mapping. Chapter 4 is a case study where a predictive geological map is generated for the Baffin Island hyperspectral cube. This study also makes use of the SSEE and ISMA algorithms developed in Chapters 2 and 3, to obtain an endmember set and produce fractional abundance maps, respectively. Combining the information from the fractional maps into a single map that is similar to traditional lithological maps is a more practical approach for predictive mapping. The focus of Chapter 4 is: 1) the development of a methodology to generate a predictive lithological map from fractional abundance maps; 2) the lithologic identification of the endmember spectra based on a comparison with field spectra and known mineral absorption features; and, 3) to showcase the economic potential of particular endmember distribution maps within the study area. This study is designed to demonstrate the useful application of hyperspectral data for lithological mapping in the Arctic environment, where the ability to capture the spectral diversity related to bedrock geology, even in the presence of lichen, can result in predictive maps that are comparable with the existing published maps.

1.4 Thesis outline

This thesis is presented in paper format, such that each of Chapters 2, 3, and 4 represent stand-alone manuscripts. The titles and publication details of the three papers, as of the December 14th, 2006, are listed below. Chapter 2 has been submitted for publication and is undergoing review, but an extended abstract of this paper has been published and was presented at the International Association for Mathematical Geology, 11th International Congress held in Liege, Belgium (Rogge et al., 2006). Chapter 3 has been published in the December, 2006, issue of IEEE Transactions on Geoscience and Remote Sensing. Chapter 4 has been submitted for publication and is undergoing review.

An abstract of this work has been published and presented at the annual meeting of the Geological and Mineralogical Associations of Canada in Halifax, Nova Scotia (Rogge et al., 2005). All data processing, analysis and interpretation, and the writing of the chapters/papers, were my own work. The one exception was the help of Jinkai Zhang and Jilu Feng in writing some of the more complex parts of the IDL code necessary to run the algorithms. Co-authors provided critiques and editing of the manuscript drafts.

Chapter 2: Rogge, D.M., Rivard, B., Zhang, J., Harris, J., Feng, J., and A. Sanchez (*submitted*). Integration of spatial-spectral information for endmember extraction.

Chapter 3: Rogge, D.M., Rivard, B., Zhang, J., Feng, J (2006). Iterative spectral unmixing for optimizing per-pixel endmember sets. *IEEE Transactions on Geoscience and Remote Sensing*, 44, 3725-3736.

Chapter 4: Rogge, D.M., Rivard, B., Harris, J., and Zhang, J (*submitted*). Application of hyperspectral data for remote predictive mapping, Baffin Island, Canada, *submitted to a special volume on Hyperspectral Remote Sensing for Economic Geology*.

Chapter 5: This chapter includes a summary of the thesis, contributions and their significance, and suggestions for further work.

REFERENCES

Adams, J.B., Smith, M.O., & Johnson, P.E. (1986). Spectral mixture modeling: a new analysis of rock and soil types at the Viking Lander 1 site. *Journal of Geophysical Research*, 91, 8098-8112.

Adams, J.B., Smith, M.O., & Gillespie, A.R. (1993). Imaging spectroscopy: Interpretation based on spectral mixture analysis, In: C.M. Pieters & P.A. Englert (Eds.), *Remote Geochemical Analysis: Elemental and Mineralogical Composition,* Cambridge University Press, Cambridge, 145-166.

Adams, J.B., & Gillespie, A.R. (2006). *Remote sensing of landscapes with spectral images: A physical modeling approach.* Cambridge University Press, New York, 362.

Asner G.P., & Heidebrecht, K.B. (2002). Spectral unmixing of vegetation, soil and dry carbon cover in arid regions: comparing multispectral and hyperspectral observations. *International Journal of Remote Sensing*, 23, 3939-3958.

Bateson A., and Curtiss, B. (1996). A method for manual endmember selection and spectral unmixing. *Remote Sensing of Environment,* 55, 229-243.

Berman, M., Kiiveri, H., Lagerstrom, R., Ernst, A., Dunne, R., & Huntington, J.F. (2004). ICE: A statistical approach to identifying endmembers in hyperspectral images. *IEEE Transactions on Geoscience and Remote Sensing*, 42, 2085-2095.

Bierwirth, P., Huston, D., & Blewett, R. (2002). Hyperspectral mapping of mineral assemblages associated with gold mineralization in the Central Pilbara, Western Australia. *Economic Geology*, 97, 819-826.

Blount, G., Smith, M.O., Adams, J.B., Greeley, R., & Christensen, P. R. (1990). Regional Aeolian dynamics and sand mixing in the Gran Desierto: Evidence from Landsat Thematic Mapper images. *Journal of Geophysical Research*, 95, 15463-15482.

Boardman, J.W. (1993). Automating spectral unmixing of AVIRIS data using convex geometry concepts. *Summaries of the fourth Annual JPL airborne Geoscience Workshop*, JPL Publication 93-26, 1, 11-14.

Bowles, J., Palmadesso, P.J., Antoniades, J.A., Baumback, M.M., & Rickard, L.J. (1995). Use of filter vectors in hyperspectral data analysis. *Proceedings SPIE Infrared Spaceborne Remote Sensing III,* 148-157.

Chang, C-I., & Plaza, A. (2006). A fast iterative algorithm for implementation of Pixel Purity Index. *IEEE Transactions on Geoscience and Remote Sensing Letters*, 3, 63-67.

Clark, R.N., King, T.V.V., Klejwa, M., & Swayze, G.A. (1990). High spectral resolution reflectance spectroscopy of minerals. *Journal of Geophysical Research*, 95, 12653-12680.

Clark, R.N., Swayze, G.A., Gallagher, A.J., King, T.V.V., & Calvin, W.M. (1993). The U. S. Geological Survey, Digital Spectral Library: Version 1: 0.2 to 3.0 microns. *U.S. Geological Survey,* Open File Report 93-592.

Gillespie, A.R. (1992). Spectral mixture analysis of multispectral thermal infrared images. *Remote Sensing of Environment*, 42, 137-145.

Griffiths, P.S., Curtis, P.A.S., Fadul, S.E.A., & Scholes P.D. (1987). Reconnaissance geological mapping and mineral exploration in northern Sudan using satellite remote sensing. *Geology Journal*, 22, 225-249.

Heinz, D.C., & Chang, C-I. (2001). Fully constrained least squares linear spectral mixture analysis method for material quantification in hyperspectral imagery. *IEEE Transactions on Geoscience and Remote Sensing*, 39, 529-545.

Hunt, G. R. (1977). Spectral signatures of particulate minerals in the visible and near infrared. *Geophysics*, 42, 501-513.

Ifarraguerri, A., & Chang, C-I. (1999). Multispectral and hyperspectral image analysis with convex cones. *IEEE Transactions on Geoscience and Remote Sensing,* 37, 756-770.

Kaufmann, H., (1988). Mineral exploration along the Aqaba-Levant structure by use of TM data; concepts, processing, and results. *International Journal of Remote Sensing*, 9, 1639-1658.

Kruse, F. A., Kierein-Young, K.S., & Boardman, J.W. (1990). Mineral mapping at Cuprite, Nevada with a 63 channel imaging spectrometer. *Photogrammetric Engineering and Remote Sensing*, 56, 83-92.

Loughlin, W.P. (1991). Principal component analysis for alteration mapping. *Photogrammetric Engineering and Remote Sensing*, 57, 1163-1169.

Murphy, R.J. (1995). Mapping of jasperiod in the Cedar Mountains, Utah, U.S.A., using imaging spectrometer data. *International Journal of Remote Sensing*, 16, 1021-1041.

Mustard J.F., & Pieters, C.M. (1987). Abundance and distribution of ultramafic microbreccia in Moses Rock dike - Quantitative application of mapping spectroscopy. *Journal of Geophysical Research*, 92, 10376-10390.

Nascimento, J.M.P., & Dias, J.M.B. (2005). Vertex component analysis: a fast algorithm to unmix hyperspectral data. *IEEE Transactions on Geoscience and Remote Sensing*, 43, 898-910.

Neville, R.A., Staenz, K., Szeredi, T., Lefebvre, J., & Hauff, P. (1999). Automatic Endmember Extraction from Hyperspectral Data for Mineral Exploration. *Fourth International Airborne Remote Sensing Conference and Exhibition / 21st Canadian Symposium on Remote Sensing*, Ottawa, Ontario, Canada, 21-24 June.

Neville, R.A., Levesque, J., Staenz, K., Nadeau, P., Hauff, P., & Borstad, G.A. (2003). Spectral unmixing of hyperspectral imagery for mineral exploration: comparison of results from SFSI and AVIRIS. *Canadian Journal of Remote Sensing*, 29, 99-110.

Plaza, A., Martinez, P., Perez, R., & Plaza, J. (2002). Spatial/spectral endmember extraction by multidimensional morphological operations", *IEEE Transactions on Geoscience and Remote Sensing*, 40, 2025-2041.

Podwysocki, M.H., Segal, D.B., & Abrams, M.J. (1983). Use of Multispectral Scanner images for assessment of hydrothermal alteration in the Marysvale, Utah, Mining Area. *Economic Geology*, 78, 675-687.

Richards, J., & Jia, X. (1999). *Remote Sensing Digital Image Analysis*, third revised and enlarged edition Edition, Springer-Verlag, Berlin, Heidelberg, New York.

Rogge, D., Rivard, B., Zhang, J., Feng, J., & Harris, J. (2006). Integration of spatial-spectral information for endmember extraction. *International Association for Mathematical Geology*, 11th International Congress, University de Leige, Belgium, September 3-8.

Rogge, D., Rivard, B., Zhang, J., & Harris, J. (2005). Remote predictive geological mapping using airborne hyperspectral data, Baffin Island. *Annual Meeting of Geological Association of Canada*. Halifax Nova Scotia, May15-18.

Sabol, D.E., Adams, J.B., & Smith, M.O. (1992). Quantitative sub-pixel spectral detection of targets in multispectral images. *Journal of Geophysical Research*, 97, 2659-2672.

Smith, M.O., Jonhson, P.E., & Adams, J.B. (1985). Quantitative determination of mineral types and abundances from reflectance spectra using principal component analysis. *Proceedings of the Fifteeth Lunar and Planetary Science Conference, Part 2, Journal of Geophysical Research*, 90, Supplement, C797-C804.

Sultan, M., Arvidson, R.E., Sturchio, N.C., & Guiness, E.A. (1987). Lithologic mapping in arid regions with Landsat Thematic Mapper data: Meatiq dome, Egypt. *Geological Society of America Bulletin*, 99, 748-762.

Sabins, F.F. (1999). Remote sensing for mineral exploration. *Ore Geology Reviews*, 14, 157-183.

Settle, J.J., & Drake, N.A. (1993). Linear mixing and the estimation of ground cover proportions. *Inernational Journal of Remote Sensing*, 14, 1159-1177.

Vitorello, I., & Galvao, L.S. (1996). Spectral properties of geologic materials in the 400- to 2500 nm range: Review for applications to mineral exploration and lithological mapping. *Photo-Interpretation*, 2, 77-96.

Winter, M.E. (1999) Fast autonomous spectral endmember determination in hyperspectral data. *Proceedings of the Thirteenth International Conference on Applied Geologic Remote Sensing*, Vancouver, B.C., Canada, II, 337-344.

Zamudio, J.A. and Atkinson, W.W. Jr. (1990). Analysis of AVIRIS data for spectral discrimination of geologic materials in the Dolly Varden Mountains, Nevada. *JPL AVIRIS Workshop Proceedings*, 162-166.

CHAPTER 2
INTEGRATION OF SPATIAL-SPECTRAL INFORMATION FOR THE IMPROVED EXTRACTION OF ENDMEMBERS[1]

2.1 Introduction

Spectral mixing is a problem inherent to remote sensing data and results in few image pixel spectra representing "pure" targets (Settle and Drake, 1993). Linear spectral mixture analysis (SMA) (Adams et al., 1986; Adams et al., 1993) is designed to address the problem of mixed pixels. It assumes that the pixel-to-pixel variability in a scene results from varying proportions of spectral endmembers. The spectrum of a mixed pixel can then be calculated as a linear combination of the endmember spectra weighted by the area coverage of each endmember within the pixel, if the scattering and absorption of electromagnetic radiation is derived from a single component on the surface (Keshava and Mustard, 2002).

Image endmembers (referred simply as endmembers hence forth) are pixel spectra that lie at the vertices of the image simplex in n-dimensional space (Figure 2.1A). The extraction of endmembers from an image has benefits over the use of spectra measured in the field or laboratory. Library and field spectra are rarely acquired under the same conditions as airborne or satellite data; and they may not adequately represent all important endmembers. On the other hand field and laboratory spectra are usually collected from surfaces one wants to map, and thus, they have direct physical meaning for mapping purposes. Imagery may provide similarly meaningful endmembers that can be considered "pure", or relatively "pure" spectra, meaning that little or no mixing with other endmembers has occurred within a given pixel.

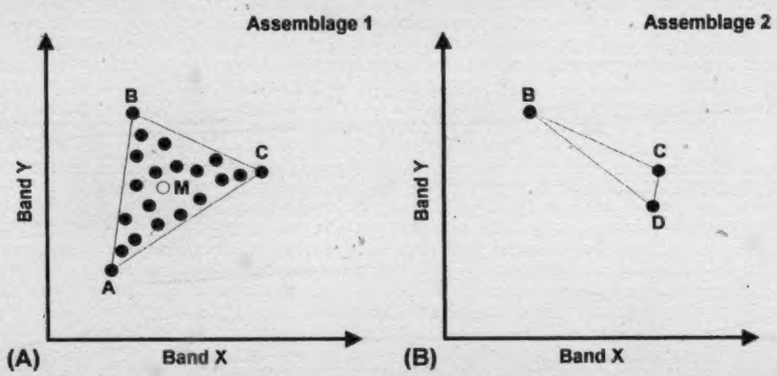

Figure 2.1 2-dimensional scatterplot of endmember assemblage A, B, and C (A); and, B, C, and D (B) located at the vertices of the simplex. In (A) all other pixels (black dots) can be represented as a linear mixture of the 3 endmembers with pixel M an equal mixture of A, B, and C. The relative spectral contrast for C changes for the 2 assemblages, whereby C has an equivalent contrast with A and B in assemblage 1 and a lower contrast in assemblage 2.

---

[1] An extended abstract of this chapter has been published. Rogge, D., Rivard, B., Zhang, J., Feng, J., & Harris. J. (2006). Intergration of spatial-spectral information for endmember extraction. *International Association for Mathematical Geology*, 11th International Congress, University de Leige, Belgium, September 3-8.

To obtain accurate unmixing results the endmembers selected must be representative of surface components that occur in relatively pure form (Adams and Gillespie, 2006). For this reason much literature has focused on the subject of endmember extraction and includes methods such as, the pixel purity index (PPI) (Boardman et al., 1995), the manual endmember selection tool (MEST) (Bateson and Curtiss, 1996), N-FINDR (Winter, 1999), the optical real-time adaptive spectral identification system (ORASIS) (Bowles et al., 1995), convex cone analysis (CCA) (Ifarraguerri and Chang, 1999), iterative error analysis (IEA) (Neville et al., 1999), the automated morphological endmember extraction (AMEE) (Plaza et al., 2002), the iterated constrained endmembers (ICE) (Berman, et al., 2004), and vertex component analysis (VCA) (Nascimento and Dias, 2005). With the exception of AMEE, the above methods select endmembers by discriminating between pixels using their spectral characteristics. This is done independent of neighboring pixels, the spatial distribution of endmembers, and the characteristic spatial mixing relationships between endmembers (e.g. do endmembers mix).

The selection of endmembers becomes more problematic as their spectral contrast approaches the detection limits of the given sensor (e.g. SNR). The "pixel-to-pixel" spectral contrast can be calculated using the Euclidean distance between two vectors (Adams and Gillespie, 2006). Image components such as snow, water, vegetation and sand have high contrast when compared to one another, whereas the spectral contrast between different species of vegetation can be considered low. Improving the spectral contrast between pixels in an image can be accomplished using spectral-based methods such as transforms (e.g. PCA, MNF)(Adams and Gillespie, 2006), derivative analysis (Tsai and Philpot, 1998), and normalization (Cudahy, 1999).

Masking can also be used to improve spectral contrast by removing spectrally dominant image components resulting in a relative increase in spectral contrast for the remaining image components. However, masking will only be effective in cases where spectral mixing is minimal, which is not commonly the case for natural environments. Masking does illustrate that spectral contrast is variable in an image depending on the spatial neighborhoods, where for each spatial neighborhood the assemblage of endmembers may change. Figure 2.1 provides such an illustration showcasing endmember C as observed in two different spatial neighborhoods, each with a distinct endmember assemblage. In case 1, C is equivalently distinct from both A and B and can be considered to have high spectral contrast relative to A and B. However, in case 2, C is spectrally similar to D, and thus has lower relative spectral contrast compared with case 1. By conducting the image extraction on image subsets we can take advantage of the spatial characteristics of each endmember, which may result in a given endmember having higher spectral contrast in a specific image subset, thus facilitating its extraction. Figure 2.2 illustrates a geological example where two lithologic units are spectrally similar, but spatially independent. Obtaining endmembers for each lithologic unit can be improved by analysing image subsets.

Averaging pixels that lie near the vertices of a simplex is common practice to generate representative endmember spectra (e.g. in IEA). However, spectral-based endmember extraction methods do not take into account the spatial relationships between the pixels. Thus, spectrally similar pixels that are spatially independent can be averaged together (e.g. Figure 2.2 endmember i and j) to provide a representative endmember. By constraining the averaging process to include only spatially associated pixels it should be possible to reduce spectral contamination of spatially unrelated but spectrally similar endmembers.

This paper presents a spatial-spectral endmember extraction algorithm (SSEE) that makes use of the spectral and spatial characteristics of image pixels during the search for image endmembers. The spatial characteristics are used to increase the spectral contrast between spectrally similar, but spatially independent endmembers, thus improving the potential of findings these endmembers. We also impose spatial constraints when averaging spectrally similar pixels to preserve similar but distinct endmembers that occupy unique image regions. The output is an image endmember library, where the individual endmembers are defined based on spectral and spatial characteristics. Section 2 gives a brief overview of three relevant endmember extraction methods. It is followed by a detailed description of the SSEE algorithm (section 3) and two demonstrations of SSEE for airborne hyperspectral data.

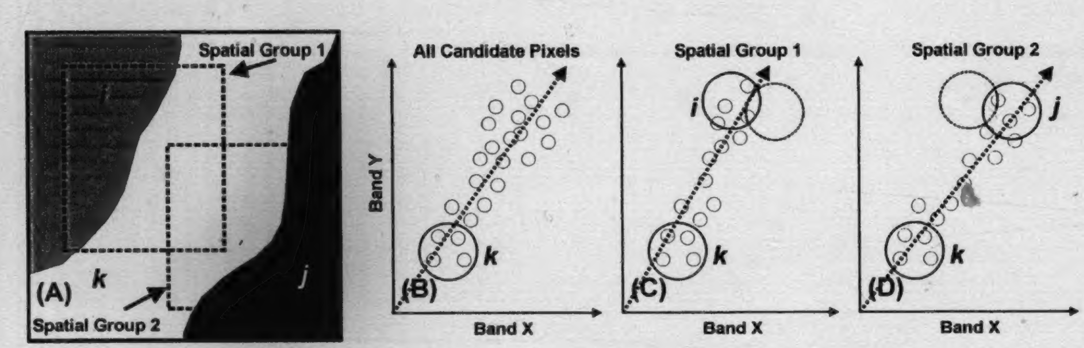

Figure 2.2 (A) Image region showing three endmembers (i, j, and k), where mixing occurs between i and k, j and k, but not i and j. Spatial groups shown with dotted square in (A). (B) 2-dimensional scatter-plot where endmembers i and j are difficult to discriminate. (C) and (D) show scatter-plots for the two spatial group allowing for better discrimination of endmembers i and j. Dotted lines in (B), (C), and (D) are the eigenvectors related to the largest eigenvalue for each distribution.

2.2 PPI, IEA, and AMEE algorithms

By far the most commonly used endmember extraction tool is PPI, which searches for vertices that define the data volume in n-dimensional space. Commonly the first step of PPI is to apply a principal component analysis (PCA) or minimum noise transform (MNF) to reduce the dimensionality of the data set. The assumption here is that the image endmembers lie within the first few principal component axes, whereas the remaining axes are related to noise. However, some image components have weak signals and contribute little energy to the eigenvalues, and thus, determining the cutoff threshold between the eigenvalues caused by signal and noise is problematic (Chang and Du, 2004).

PPI is semi-automated and obtains endmember candidate pixels by projecting the transformed data onto a high number of randomly oriented vectors (k) in n-dimensional space. Those pixels that lie at either end of a given random vector are assigned a "hit". The total number of hits are tallied for each pixel, for all random vectors. Pixels that receive more hits than a set cutoff threshold (t) are considered candidate endmember pixels, or "pure" pixels. This cutoff threshold is commonly a fixed empirical value (e.g. 2 or 10), or based on statistical parameters, such as the mean hits value (Plaza et al., 2004). The candidate endmember pixels are then loaded into a n-dimension visualization tool, such that the user can visually identify the extreme pixels in the data cloud. This last step requires a significant degree of human intervention from an experienced operator. PPI is particularly sensitive to the input parameters k and t (Chang and Plaza, 2006). Owing to the fact that the vectors are randomly generated, results may not be repeatable. In order to obtain results that are close to repeatable, PPI requires k to be sufficiently large (e.g 10^4), such that the number of endmember candidate pixels selected levels off asymptotically as a function of the number of vectors used.

IEA is implemented in the Imaging Spectrometer Data Analysis System (ISDAS) (Staenz et al., 1998), and is based on the residual error image generated when a data set is unmixed using a Weighted Nonnegative Least Squares approach (WNNLS) (Haskell et al., 1981). This method has been used in endmember comparative studies (e.g. Winter and Winter 2000; Plaza et al., 2004) and was shown to be a robust extraction tool. IEA works by performing a series of constrained unmixing operations on the image, such that the residual error is minimized. The mean spectrum of the scene is used as the starting endmember to initialize the unmixing process. The residual error image is essentially a distance measurement in n-dimensional space (n = number of bands) between the mean spectra and each pixel spectrum in the image. Pixels (within a predetermined solid angle θ) that encompass the largest errors form a new endmember, with the initial mean spectra discarded. This process is repeated, where each new endmember is added to the existing endmember set until the number of endmembers specified by the user is reached or until a specified average error tolerance condition is met. The main drawback to IEA is that it is computationally intensive, specifically as the number of endmembers required increases.

AMEE is significantly different from spectral-based methods as it integrates spatial information in order to extract endmembers from an image. AMEE runs on the full data cube with no dimensionality reduction. The algorithm begins by searching spatial neighborhoods around each pixel in the image for the most spectrally pure and mostly highly mixed pixel. This task is accomplished using mathematical morphology operators dilation and erosion, respectively. Each spectrally pure pixel is assigned an "eccentricity" value, which is calculated as the distance between the most spectrally pure and mostly highly mixed pixel for the given spatial neighborhood. This process is repeated iteratively for larger spatial neighborhoods up to a maximum size that is predetermined. At each iteration the "eccentricity" value of the selected pixels is updated. The final endmember set is obtained by applying a threshold to the resulting greyscale "eccentricity" image. There are some limitations to AMEE, particularly a significant increase in processing time as the maximum size of the spatial neighborhood becomes large; and, the algorithms ability to select only one pixel per spatial neighborhood (Plaza et al., 2002). However, AMEE has been shown to produce results that are comparable to better with other endmember extraction methods (Plaza et al., 2002; Plaza et al., 2004).

2.3 Description of the spatial-spectral endmember extraction (SSEE) algorithm

The SSEE algorithm comprises four steps: 1) application of singular value decomposition (SVD) to determine a set of eigenvectors that describe most of the spectral variance of image subsets; 2) projection of the entire image data onto the eigenvectors to determine a set of candidate endmember pixels; 3) use of spatial constraints to combine and average spectrally similar candidate endmember pixels; and, 4) listing of candidate endmembers in order of spectral similarity.

2.3.1 SSEE Step 1

Step 1 makes use of SVD, which is very efficient in obtaining a set of eigenvectors that explain most of the spectral variability of a given scene (Healey and Slater, 1999; Thai et al., 1999). SVD, along with PCA and MNF, are projection techniques commonly used in remote sensing. SVD and PCA are equivalent in the case of zero-mean data, and PCA is equivalent to MNF in the case of white noise (Jolliffe, 1986; Green et al., 1988; Scharf, 1991).

SSEE obtains a set of candidate endmember pixels by applying SVD to subsets of an image (Figure 2.3 B and C). The SVD is calculated using the SVDC routine in IDL™ 6.1, which is based on the routine svdcmp described in Press et al (1992). Basis vectors that explain > 1% of the spectral variance, using a minimum SNR of 100:1, are retained from each subset and compiled into one vector file. These vectors will likely be related to the local high contrast endmembers. For each subset the minimum number of vectors is set to 2, whereas the maximum is defined by the 1% cutoff threshold. The minimum size of the subset that can be used is defined by the square root of the number of bands, whereas the maximum size is that of the entire image. The SSEE algorithm in its present form makes use of subsets that are equal in size, are square, and do not overlap.

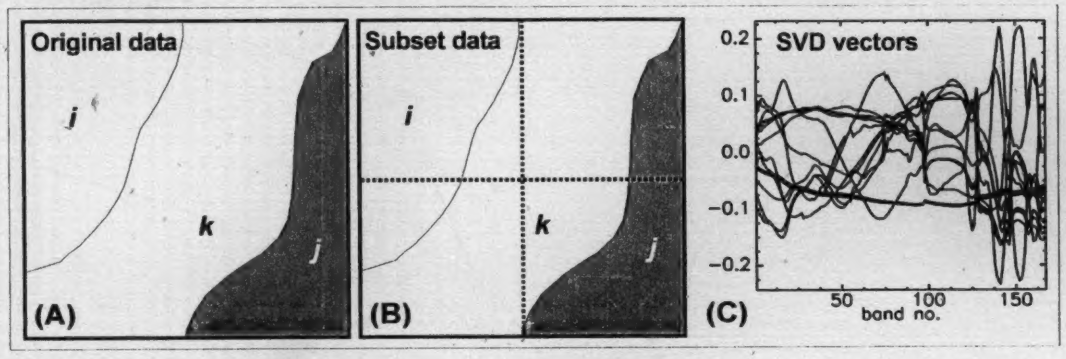

Figure 2.3 SSEE step 1: (A) Image region showing three image components (i, j, and k). (B) Four image subsets. (C) Compiled basis vectors from all subset shown in (B).

2.3.2 SSEE Step 2

In step 2, the entire image data (Figure 2.4B) is projected onto the compiled vector set with the pixels that lie at either extreme of the vectors retained (Figure 2.4C). These pixels (Figure 2.4D) represent the candidate pixel endmember set, which is used in step 3.

2.3.3 SSEE Step 3

Step 3 analyzes the spatial and spectral characteristics of the candidate endmember set to average spectrally similar endmember candidates that are spatially related. Step 3 scans the image with a sliding window of size equal to the subset size used in step 1. Step 3 begins by updating the candidate pixel endmember set by comparing each candidate endmember to all other spatially associated pixels (defined by the window size). All pixels that are similar, based on a minimum spectral angle or root mean square error (RMS), are added to the candidate endmember set (Figure 2.5B). This process is similar to retaining more than 1 pixel at either extreme of the eigenvectors. However, using this approach we only retain spectrally similar pixels that are spatially related. RMS is primarily used for very low reflectance signatures such as water, because the minimum spectral angle is commonly exceeded when candidate water spectra are compared.

Step 3 continues by averaging each of the candidate endmember pixels with all other endmember candidates within the window (Figure 2.5 C-F). This averaging process is repeated for x number of iterations, with the objective to: 1) reduce the effects of noise; and, 2) find image pixels that are spectrally similar, but spatially related within the window (Figure 2.5). Multiple iterations allow the algorithm to compare and average pixels that are farther than the window size, but are related by other candidate pixels that lie spatially between them (Figure 2.5C-F). This iterative approach allows the user to compress endmember clusters, such that they have negligible variance (Figure 2.5F). The end product is a set of endmembers that are defined both spectrally and spatially, and take into account local spectral variance.

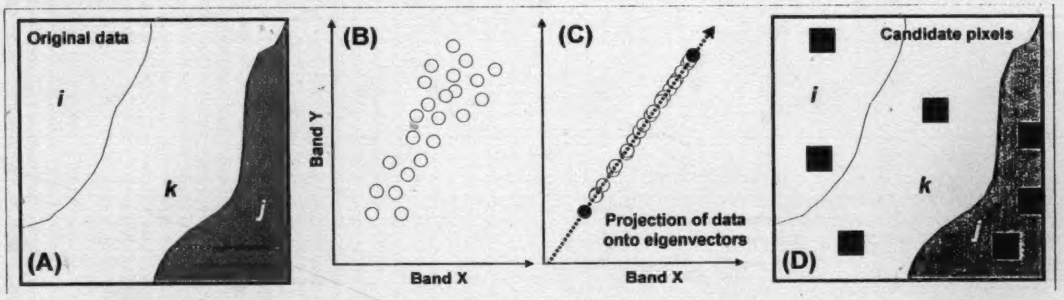

Figure 2.4 SSEE step 2: (A) Image region showing three image components (i, j, and k). (B) Image data in 2-D space. (C) Projection of entire image data onto 1 of the eigenvectors derived from step 1. (D) Spatial distribution of candidate endmember pixels.

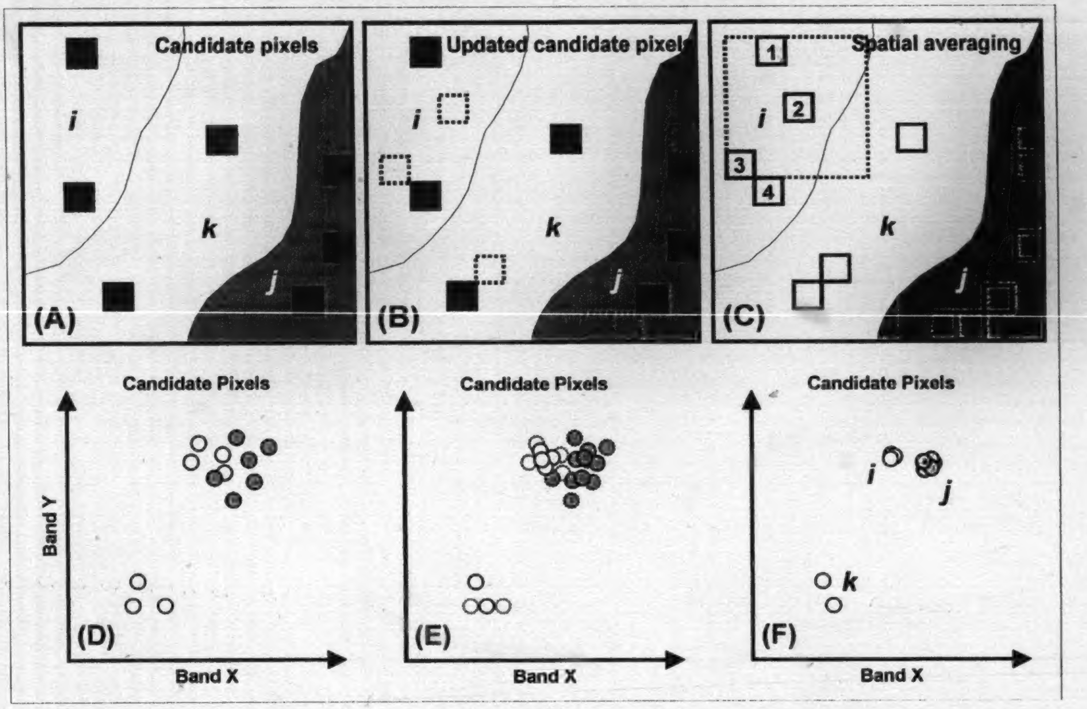

Figure 2.5 SSEE step 3: (A) Candidate endmember pixels showing spatial distribution with respect to units i, j, and k. (B) Updated candidate endmember pixels. (C) Spatial averaging process using a sliding window centered on each updated candidate endmember pixel. (D) Spectral distribution in 2-D space for bands x and y. (E) First iteration of spatial-spectral averaging. Averaged pixels shown as solid lines, with original pixels shown as dashed circles. Pixel number 2 (see C) is averaged with 1 and 3, but not 4, which is averaged with pixel 3. (F) Second iteration of spatial-spectral averaging of pixel 2, which now takes into account the influence of pixel 4 on 3, thus, condensing the spectral cluster further. Continued iterations will compress endmembers i and j into clusters with negligible variance, which now represent two distinct spectral endmembers. Note that for endmember k, only two pixels are average as the third pixel is outside the averaging window.

2.3.4 SSEE Step 4

The final endmember set derived from step 3 is reordered based on spectral angle. The first endmember in the existing library is assigned as the first spectra and compared to all other endmembers, with the most similar assigned the next position in the list. This process is repeated recursively until all spectra have been ordered. The finalized list allows the user to quickly view those endmembers that are spectrally similar, but spatially independent. Owing to the iterative spatial averaging process a number of the reordered spectra will be duplicates (e.g. Figure 2.5F). The endmembers retain their image coordinates.

2.4 Data sets and evaluation methodology

Two evaluations of the SSEE algorithm were conducted with hyperspectral imagery. The first evaluation is for data from Cuprite Nevada, and is designed to demonstrate the characteristics of SSEE using different spatial subset and averaging window sizes. We examine the link between subset size, eigenvectors retained, and the resulting number of endmembers selected from the image. The second evaluation is for data of Baffin Island, northern Canada. We examine the endmembers related to bedrock geology obtained by SSEE, IEA and PPI in the context of field spectra and also examine unmixing results in the context of the spatial distribution of the endmembers. A comparison with AMEE was not conducted as the algorithm is not readily available.

2.4.1 Cuprite data set

The Cuprite imagery was acquired on June 19th, 1997 by the Airborne Visible InfraRed Imaging Spectrometer (AVIRIS) which has 224 channels covering the 0.37 to 2.51 μm spectral range with an average spectral resolution of ~10 nm. Of the 224 atmospherically corrected channels, we use 167 after removal of channels associated with H_2O and OH absorption features near 1.4 and 1.9 μm. The Cuprite area is arid with limited vegetation cover, and has excellent rock exposure comprising alteration zones characterized by the occurrence of key indicator minerals. For this evaluation we use a 200x200 pixel subset that is centered over the eastern hydrothermal alteration zone (Figure 2.6). Within this subset region the following minerals have been validated in the field as occurring in high abundance as documented in Swayze et al. (1992) and Clark et al. (2003): alunite (known variations), chalcedony (OH-quartz), kaolinite (known variations), Na-montmorillonite, and buddingtonite. Minerals that occur in lower abundances and as mixtures include: jarosite, hematite, goethite, and smectite/muscovite (Clark et al., 2003).

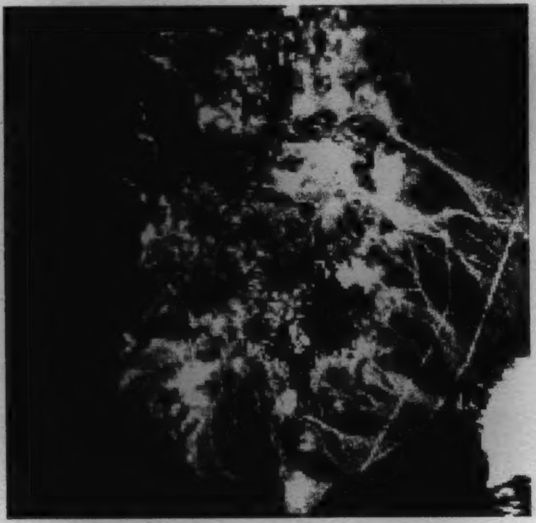

Figure 2.6 Subset region of Airborne Visible/Infrared Imaging Spectrometer (AVIRIS) hyperspectral data over Cuprite, Nevada.

2.4.2 Cuprite evaluation methodology

We evaluate SSEE with subset sizes of 20, 50, 100 and the entire image size of 200x200. For the entire image size SSEE becomes a spectral-based endmember extraction tool with no spatial constraints. At subset sizes of 20, 50, and 100, s (the SVD cutoff threshold) is set to 0.01. For the entire image s is also set to 0.01, but threshold values of 0.001 and 0.0001 are also used. This is done in order to demonstrate that including additional eigenvectors, by using a lower s value, is not equivalent to obtaining additional eigenvectors from multiple subsets. Spatial averaging is constrained to a window size equal to the subset size used to obtain the eigenvectors. For updating and averaging candidate pixels the spectral angle is set to 1.0 degree and the RMS is set to 0.1% of absolute reflectance. The number of spatial-spectral averaging iterations is set to 5.

2.4.3 Baffin Island data set

This region comprises surfaces with very disparate spectral properties such as snow-ice, water, vegetation, lichen and rock units. Within each class of surface material, the spectral contrast can be relatively low. The majority of geological spectral endmembers are defined by mineral assemblages that comprise the various rock types in the area, and not by the occurrence of a dominating mineral.

Airborne hyperspectral data (~3.5 x 7 km) were acquired with the Probe I sensor, which comprises 128 channels from 0.446 – 2.543 um with an average spectral resolution of ~15 nm and a spatial resolution of ~7 m. A vicarious atmospheric correction of the data was performed by the Canada Centre for Remote Sensing using field spectra acquired at the Iqaluit airport concurrently with the overflight. A number of the 128 channels available were not used (874-991, 1082-1171, 1271-1537, 1755-2073, and 2465-2543 nm) for this analysis owing to atmospheric water-absorption and excessive noise. No additional preprocessing (e.g. smoothing filter) was applied to the remaining 86 bands.

Field sampling and collection of spectra took place along traverses oriented perpendicular to the dominant structural and stratigraphic trends (Fig. 2.7). The spectra were acquired with a portable ASD® field spectrometer that has 2151 bands covering the 0.35 – 2.50 um spectral range. A total of 217 spectral measurements were acquired for 56 of 188 sites visited, some of which lie outside, but proximal to the study area, and are representative of the geology shown in Figure 2.7. Multiple measurements were taken at each site for fresh, weathered, polished, and partial to fully lichen coated rock surfaces.

2.4.4 Baffin Island evaluation methodology

First we compared the endmembers extracted by SSEE and IEA to determine whether or not SSEE extracted equivalent endmembers and, unique endmembers of significance. Next we conduct a comparison of PPI with SSEE and IEA using the automated part of PPI because the final steps of PPI require a high degree of human intervention. Endmember candidates determined from PPI using different values of k and t are compared with those derived from IEA and SSEE to determine if PPI was initially successful at extracting all the endmembers found with the other two methods. It is noted here that an automated version of PPI, referred to as Fast Iterative Pixel Purity

Index (FIPPI), has recently been presented by Chang and Plaza (2006). However, this method is not yet widely available to the community and was not implemented here.

The next test is a comparison with bedrock spectra acquired in the field and from samples returned to the laboratory. This comparison allows us to test if the unique SSEE endmembers are physically meaningful. Finally, linear unmixing is applied to the image using the endmembers derived from SSEE to determine if the unique endmembers extracted by SSEE show physically meaningful spatial distribution. In this paper we unmix the image using the iterative spectral unmixing analysis (ISMA) approach of Rogge et al. (2006), which is designed to unmix each pixel using an optimal per-pixel endmember set.

For this test the subset size was set to 25x25. Other parameters for this test include: 1) s = 0.01, based on a SNR of 100:1; 2) a spatial averaging window size equal to the subset size; 3) the spectral angle is set to 1.0 degree and the RMS is set to 0.1% of absolute reflectance; and, 4) the number of spatial-spectral averaging iterations is set to 10.

For this study the PPI algorithm was written using IDL™, within the ENVI™ environment. Prior to endmember extraction a MNF transform was applied to the data, where MNF bands with an eigenvalue > 1 (% of loading) were retained (27 bands of a total of 84). The number of extreme pixels at the ends of the random vectors that are assigned a hit is set to 1. We followed the guidelines of Chang and Plaza (2006) who recommended the use of 10000 random vectors. For purposes discussed latter, PPI was also applied with k equal to the number of vectors generated by SSEE. Cutoff thresholds (t) of 1, 2, and 5 were tested. IEA was implemented using ISDAS, with the number of endmembers extracted from the imagery set to 30 (default value). The maximum number (n) of pixels that fall within a solid angle (θ) that are subsequently averaged and assigned as an endmember was set to the default parameters (n=10 and θ=2.5 degrees).

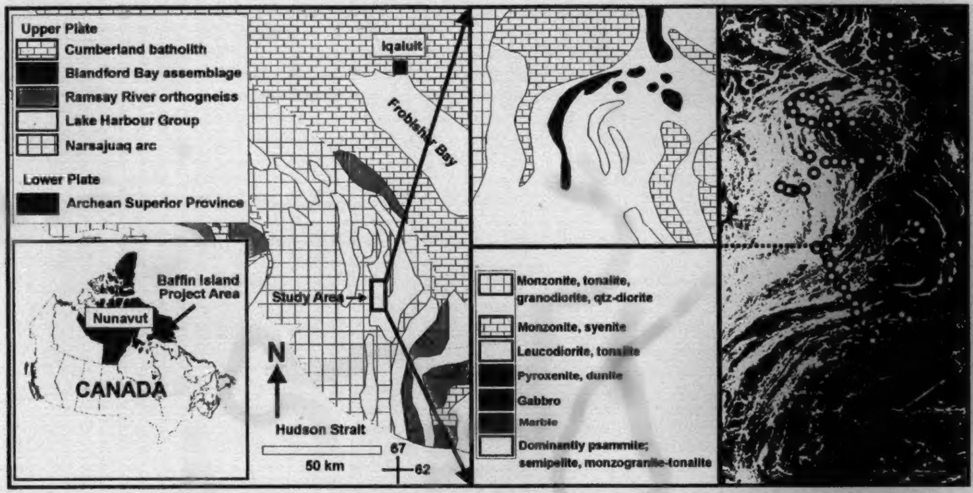
Upper Plate
Cumberland batholith
Blandford Bay assemblage
Ramsay River orthogneiss
Lake Harbour Group
Narsajuaq arc
Lower Plate
Archean Superior Province
Baffin Island Project Area
Nunavut
CANADA
Iqaluit
Frobisher Bay
Study Area
N
Hudson Strait
50 km
67
62
Monzonite, tonalite, granodiorite, qtz-diorite
Monzonite, syenite
Leucodiorite, tonalite
Pyroxenite, dunite
Gabbro
Marble
Dominantly psammite; semipelite, monzogranite-tonalite

Figure 2.7 Regional geology of south-western Baffin Island and enlargement of local geology of the study area (1:100 000) (modified from St-Onge et al., 1999). Hyperspectral data shown at far right with field locations shown as white circles. Note only the area above the dotted line was used in this study.

2.5 Results

2.5.1 Cuprite

Table 2.1 shows that as the subset size decreases the total number of endmembers selected increases; the number of vectors increases; the number of candidate endmember pixels increases; and, the number of updated candidate pixels increases. However, with smaller subsets the processing time decreases significantly, which is primarily controlled by the SVD process. Table 2.1 also shows the effect of using different values of s for the entire image data (200x200). With a smaller s value the number of eigenvectors retained increases, which increases the number of endmembers selected. This, however, is at the expense of more candidate pixels to filter through and greater processing time. The SSEE algorithm was halted using an s value of 0.0001 as the number of candidate and updated candidate pixels made the process impractical.

Table 2.1 Result details for demonstration 1: Cuprite data.

subset size	**200x200**	**200x200**	**200x200**	**100x100**	**50x50**	**20x20**
S (SVD threshold)	0.0001	0.001	0.01	0.01	0.01	0.01
vectors	87	14	4	16	63	356
candidate pixels	144	23	8	13	26	55
updated candidate pixels	23145	299	82	231	390	732
unique candidate pixels (1)	processing	18	7	11	20	32
processing time (2)	halted	856sec	702sec	687sec	403sec	167sec
endmember (3)		8	7	8	10	12
		alu (4)	alu	alu	alu	alu
		cha	cha	cha	cha	cha
		kao	kao		kao	kao
						mon
		bud	bud	bud	bud	bud
					kaoB	kaoB
		kao-hem	kao-hem	kao-hem	kao-hem	kao-hem
					alu-hem	alu-hem
		alu-geo-jar		alu-geo-jar		alu-geo-jar
				mus-hem	mus-hem	mus-hem
		uknA	uknA	uknA	uknA	uknA
		uknB	uknB	uknB	uknB	uknB

(1) No. of unique candidate endmember pixels after iterative spatial averaging. Relates only to candidate pixels not updated candidate pixels.

(2) Spatial averaging window is = subset size used to compile top eigen vectors, excluding the full image (200x200) which uses no spatial constraints.

(3) Derived from the unique candidate endmember pixels.

(4) Mineral abbreviations: alu-alunite;cha-chalcadony;kao-kaolinite;mon-montmorillonite;bud-buddingtonite;kaoB-kaolinite B;hem-hematite;jar-jarosite;goe-goethite; mus-muscovite;uknA-unknown A;uknB-unknown B

Examination of Table 2.1 shows that the number of candidate pixels is less than the number of vectors using subsets of 20, 50, and 100. This is because many of the vectors from adjacent subsets are redundant. However, if we use the entire image data and use a lower s value, the number of candidate pixels is much greater than the number of vectors. In this case each vector is orthogonal, and thus, the projected data returns more candidate pixels. When using spatial constraints more vectors are retained, many of which are redundant, but some are important vectors related to signal that improve the potential of obtaining additional endmembers. Unlike the orthogonal vectors obtained using the entire image many of the vectors retained using spatial constraints will not be orthogonal.

Figure 2.8 shows the twelve endmembers derived using a subset size of 20x20. Ten were labeled as pure minerals or mixtures of minerals based on known mineral absorption features. Two endmembers do not show diagnostic absorption features, but differ in their broad overall shape (continuum). The AVIRIS data set was unmixed using these endmembers as inputs to the ISMA approach of Rogge et al (2006). Figure 2.9 shows the resulting fractional abundance maps. Each endmember defines distinctive spatial regions that are visually consistent with the maps presented by Clark et al (2003).

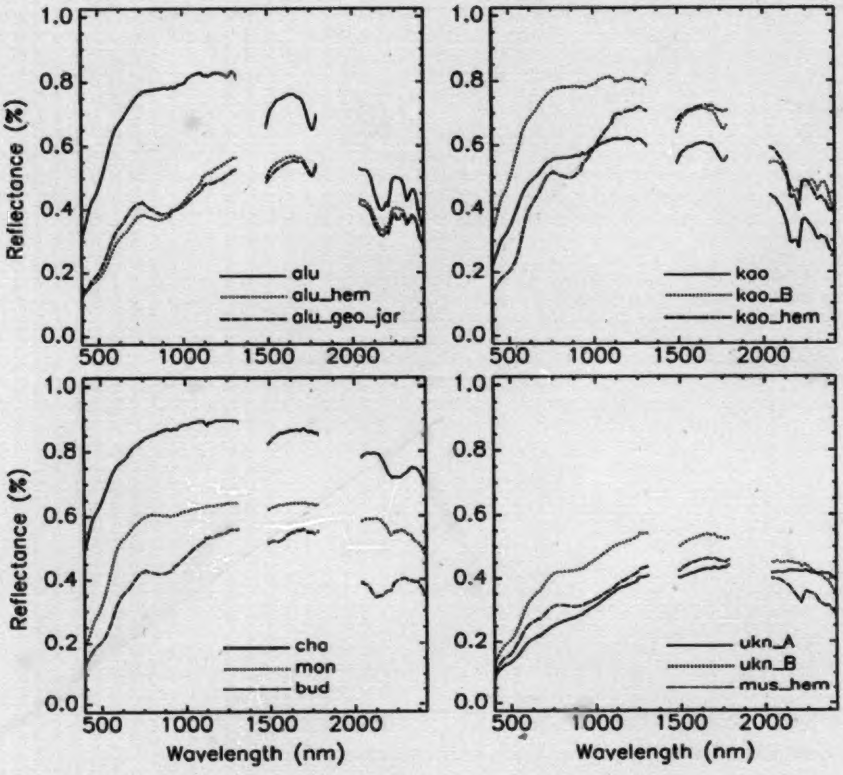

Figure 2.8 Endmember spectra derived from SSEE using a subset size of 20x20 and an s value of 0.01. Refer to Table 1 for endmember abbreviations.

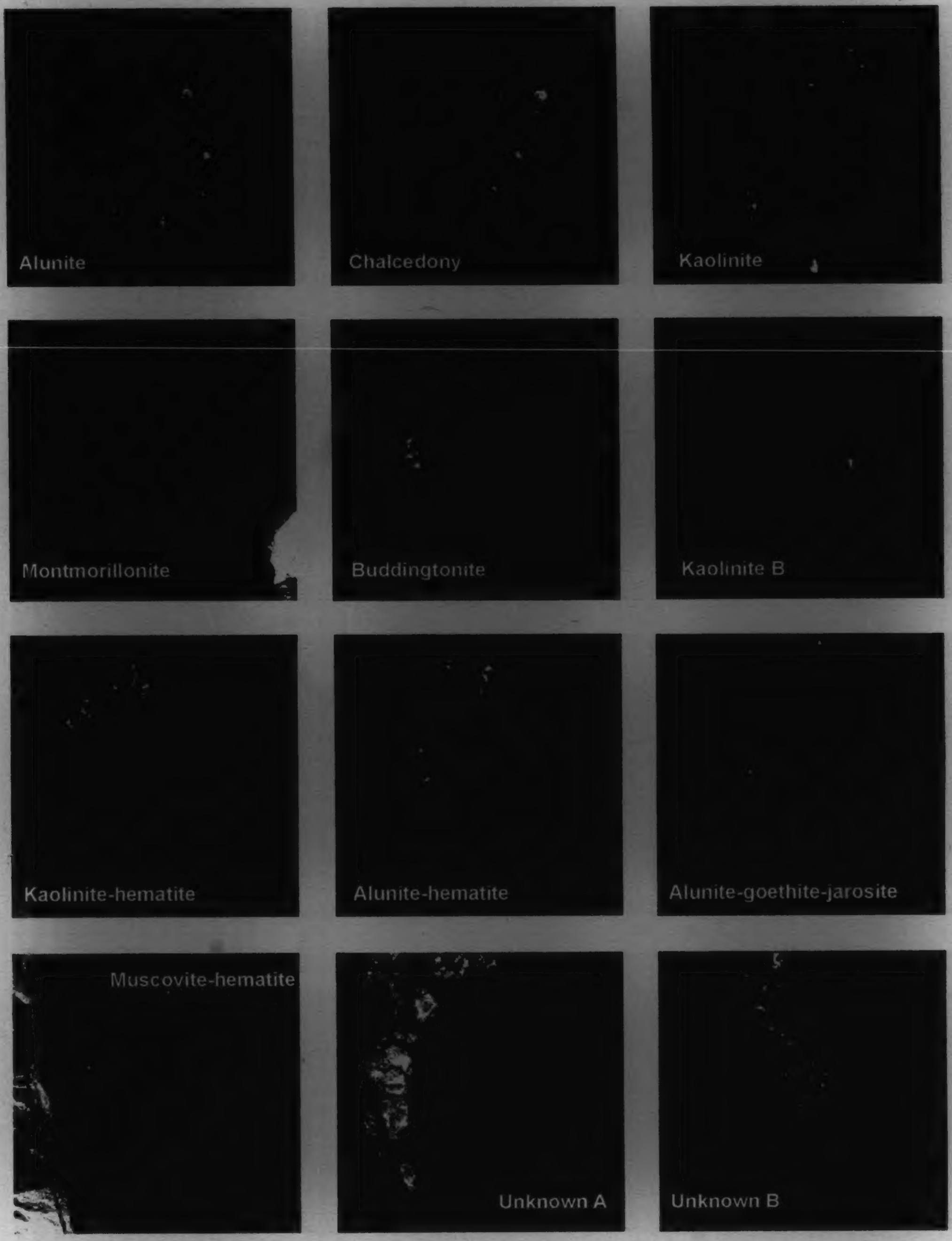
Alunite
Chalcedony
Kaolinite
Montmorillonite
Buddingtonite
Kaolinite B
Kaolinite-hematite
Alunite-hematite
Alunite-goethite-jarosite
Muscovite-hematite
Unknown A
Unknown B

Figure 2.9 Fractional abundance maps for the 12 endmembers derived from SSEE using a subset size of 20x20 and an s value of 0.01.

2.5.2 Baffin Island

The total number of vectors compiled using a subset size of 25x25 was 2184. From these, 148 endmember candidate pixels were extracted, of which 7 were noisy and left out (e.g. 141 total no. of pixels in Table 2.2). Following the spatial averaging procedure 28 of the 148 candidate endmember pixels were exact duplicates. The averaging procedure also results in many of the remaining candidate pixels showing minimal spectral difference, further reducing the number of unique endmembers and allowing the user to quickly group the spectra into endmember classes. This task is made easier by observing the original coordinates of the reordered candidate endmembers based on spectral similarity.

From the reordered library 30 endmembers were determined (Table 2.2), including 2 water, 7 snow, 2 vegetation, 2 lichen, 4 lichen-rock mixtures, and 13 rocks (Figure 2.10). Also shown in Figure 10 are the equivalent IEA endmembers. Table 2.2 lists the number of pixel spectra from SSEE and IEA that fit into each of the endmembers. Of the 30 endmembers, IEA obtained representative spectra for 18 (note 2 IEA endmember spectra were noisy and removed). Thus, SSEE extracted 12 unique endmembers, some of which showed only subtle spectral differences, but are considered unique because they are spatially independent (e.g. endmembers 22 and 23; and, 29 and 30). No unique IEA endmembers were found.

Using the 865 candidate endmember pixels derived from PPI with k = 10000 and t = 1, 29 of the 30 SSEE endmembers were accounted for (Table 2.2). However, this number falls to 24 if t = 5 (266 total candidate endmember pixels). When the equivalent number of random vectors derived by SSEE (2184) are used, 28 of the 30 endmembers were accounted for using t = 1. For t = 5 this number falls to 15. It is interesting to note that the majority of unique SSEE endmembers are part of the lichen, lichen-rock and rock endmembers, which have low overall spectral contrast. These results show that SSEE is effective at extracting a more extensive endmember list compared with IEA and PPI, especially as t increases. However, to assess whether or not the unique SSEE endmembers are physically realistic we conduct a comparison with field and laboratory spectra collected in the region.

Figure 2.11 shows 1 lichen, 2 lichen-rock, and 11 of the rock endmembers with the best matching field and laboratory spectra. Those in Table 2.2 not shown in Figure 2.11 were left out because they are not related to bedrock geology (e.g. varnish) or did not have good spectral matches (lichen 2, lichen-rock 1 and 2). The lack of spectral matches for lichen 2, and lichen-rock 1 and 2, may be attributed to incomplete sampling. The endmembers are represented by a single averaged spectrum derived from those shown in Figure 10. The matching criteria are based first on spectral angle, which highlights similar spectra, followed by a visual inspection to determine the best matches. For a good match the focus was on a good correlation with the broad overall shape (continuum) and the location of diagnostic absorption features, rather than total amplitude.

Table 2.2 Endmember classes derived from SSEE and IEA candidate endmember spectra and PPI representative spectra for different k and t.

Endmembers	Name(1)	IEA(2)	SSEE(2) 25x25	PPI t=1 (3) k=10000	PPI t=2 k=10000	PPI t=5 k=10000	PPI t=1 k=2184	PPI t=2 k=2184	PPI t=5 k=2184
EM 1	Water 1	1	2	*	*	*	*	*	*
EM 2	Water 2		2	*	*	*	*		
EM 3	Snow 1	2	10	*	*	*	*	*	*
EM 4	Snow 2	3	4	*	*	*	*	*	*
EM 5	Snow 3	1	5	*	*	*	*	*	*
EM 6	Snow 4	2	12	*	*	*	*	*	*
EM 7	Snow 5	2	4	*	*	*	*	*	*
EM 8	Snow 6	1	13	*	*	*	*	*	*
EM 9	Snow 7	2	14	*	*	*	*	*	*
EM 10	Vegetation 1	2	11	*	*	*	*	*	*
EM 11	Vegetation 2	3	16	*	*	*	*	*	*
EM 12	Lichen 1	1	6	*	*	*	*		
EM 13	Lichen 2		6	*	*	*	*	*	
EM 14	Lichen-rock 1		2	*	*		*		
EM 15	Lichen-rock 2	2	4	*	*		*	*	
EM 16	Lichen-rock 3	1	2	*	*		*		
EM 17	Lichen-rock 4		2	*	*		*		
EM 18 (rock 1)	Quartzite		1	*	*	*	*	*	
EM 19 (rock 2)	Metased(Al-OH)		1	*	*	*	*		
EM 20 (rock 3)	Metased(Fe, Al-OH)		2	*	*	*	*	*	
EM 21 (rock 4)	Qtz-rich granite		1	*	*	*	*	*	
EM 22 (rock 5)	Carbonate 1	1	4	*	*	*	*	*	*
EM 23 (rock 6)	Carbonate 2		1	*	*	*			
EM 24 (rock 7)	Metased(Fe, Al-OH)	1	3	*	*	*	*	*	*
EM 25 (rock 8)	Metasediment		4	*	*		*	*	
EM 26 (rock 9)	Varnish	1	2	*	*	*	*	*	*
EM 27 (rock 10)	Fe-oxide/hydroxide	1	1						
EM 28 (rock 11)	Vegetation mixture		1	*	*	*	*	*	*
EM 29 (rock 12)	Peridotite 1	1	2	*	*	*	*	*	
EM 30 (rock 13)	Peridotite 2		3	*	*	*	*	*	*
total no.									
of classes		18	30	29	29	24	28	22	15
of pixels			141	865	623	266	489	209	88

(1) Rock name based on work by Rogge et al (submitted) which includes a more detailed discussion of the spectral identification, spatial distribution, and economic significance of the rock units found in the entire hyperspectral data shown in Figure 7.

(2) Number represents the number of spectra extracted that fit into the given class.

(3) * indicates that at least 1 PPI candidate endmember spectra includes a representative spectra of the SSEE/IEA derived endmember class.

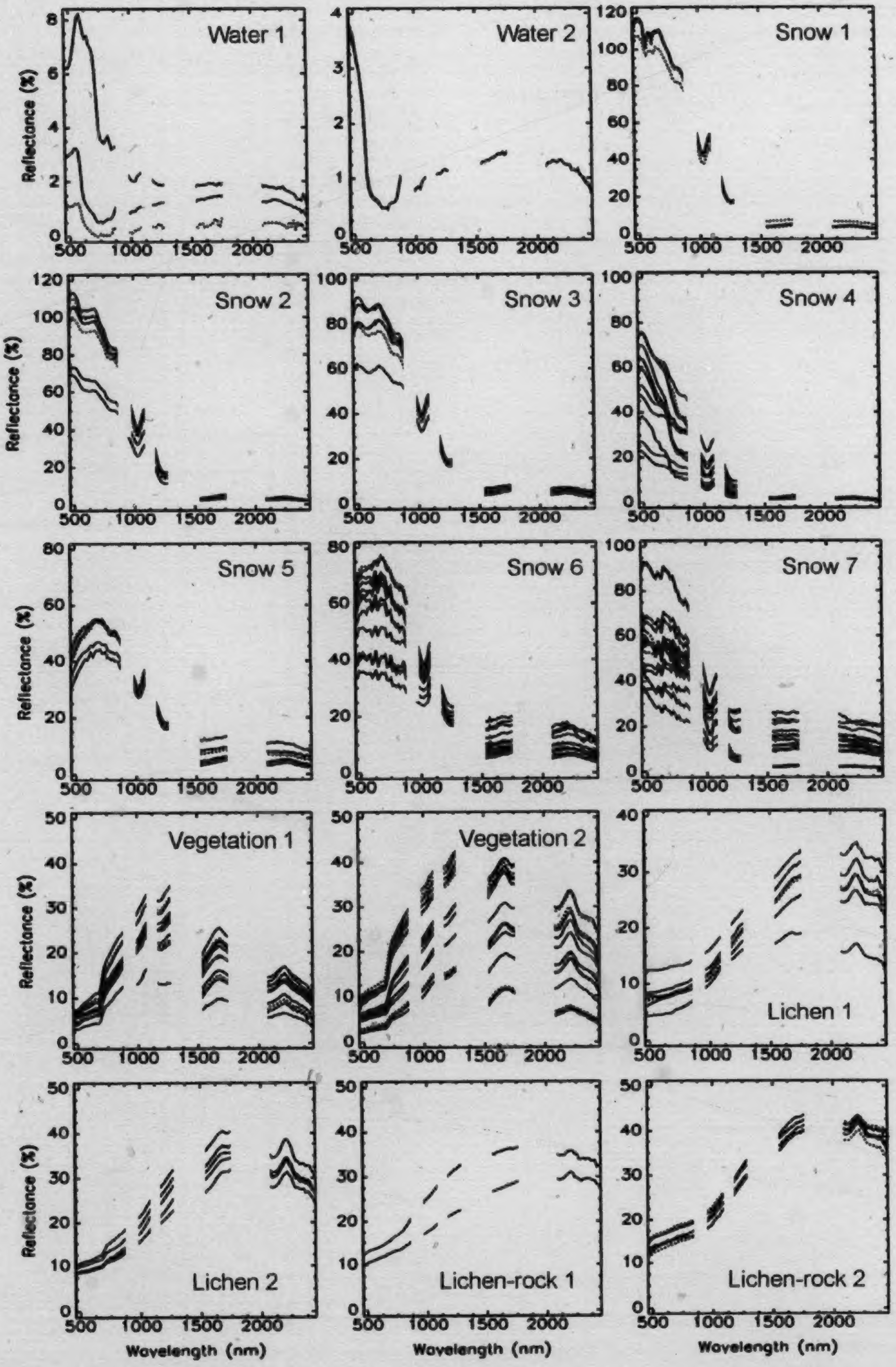

Figure 2.10 Thirty endmember classes derived from the SSEE endmember candidate library spectra (solid line) and equivalent IEA endmember (dashed line), when available.

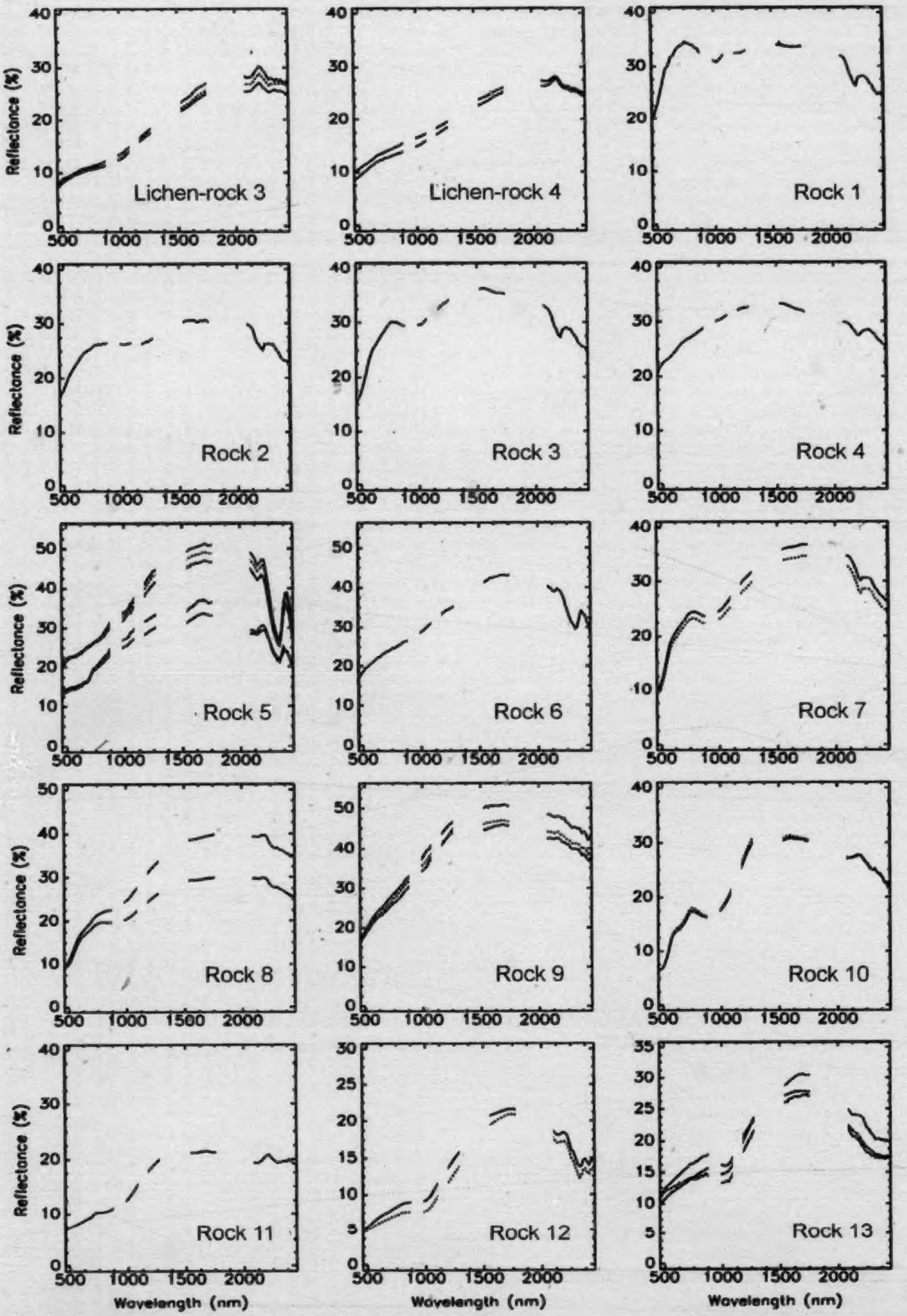

Figure 2.10 cont' Thirty endmember classes derived from the SSEE endmember candidate library spectra (solid line) and equivalent IEA endmember (dashed line), when available.

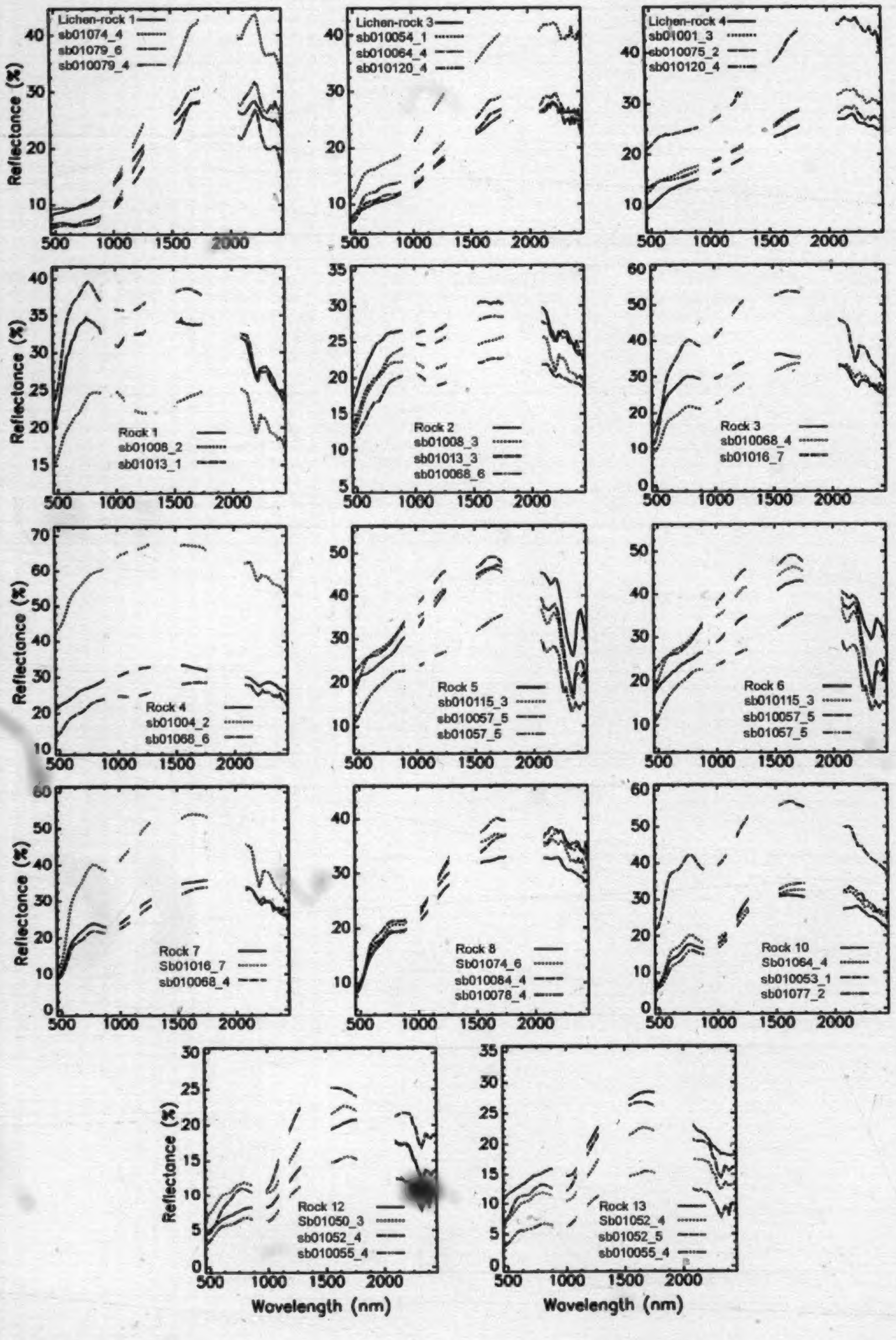

Figure 2.11 SSEE rock and lichen-rock endmember classes (solid line) with best matching field spectra.

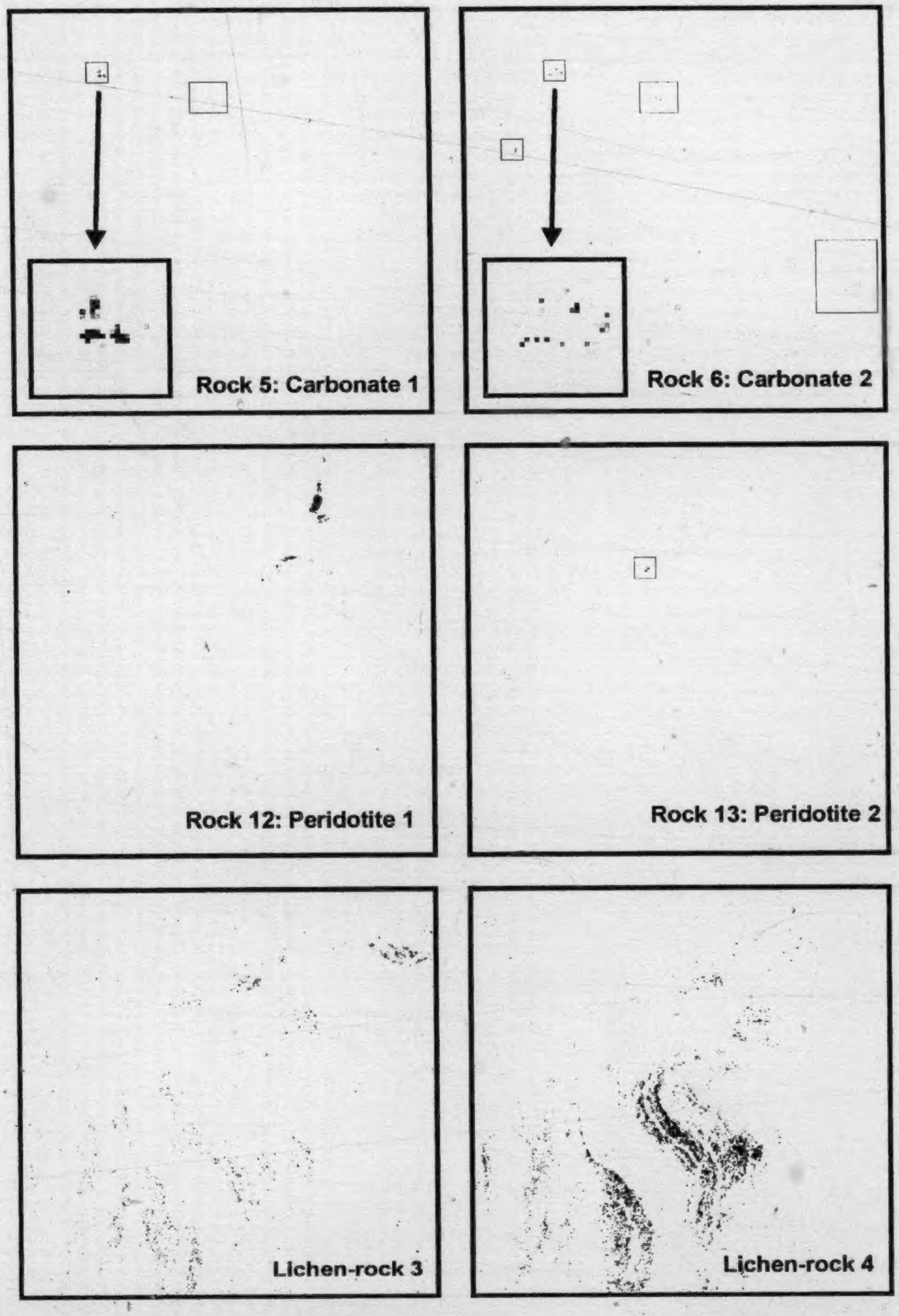
Rock 5: Carbonate 1
Rock 6: Carbonate 2
Rock 12: Peridotite 1
Rock 13: Peridotite 2
Lichen-rock 3
Lichen-rock 4

Figure 2.12 Fractional abundance maps for rock 5, 6, 12, and 13; and, lichen-rocks 3 and 4. For rocks 5, 6, and 13 boxes highlight occurrences. Note high abundance is given as black, whereas low abundance is white. This is necessary to visualize the sparse occurrences of certain rock endmembers.

Examination of the spectral matches shown in Figure 2.11 show that lichen endmembers 1, and lichen-rock 3 and 4; and the rock endmembers 1,2,3,4,5,7,8,10, and 12 show good correlation with field spectra. Of these, rock endmembers 1,2,3,4,8, and 13 were not selected by IEA or PPI using t=5 and k=2184. The best spectral matches for rock 6 and 13 are the same as for rock 5 and 12 respectively, which may indicate that these differences are not significant, or that spectral representations of rocks 6 and 13 were missed in the field. For this reason, the unmixing results were checked to see if these endmembers showed physically meaningful spatial distribution. Figure 2.12 shows the fractional abundance maps for rocks 5, 6, 12, and 13; and for lichen-rocks 3 and 4. Analysis of these maps show that rocks 5 and 6 occur locally together, but also in spatially distinctive regions. Where they do occur together locally they are spatially separated (see zoom windows in Figure 2.12). Rocks 12 and 13 define spatially distinctive regions, although the spatial extent of rock 13 is limited. The fractional abundance maps for lichen-rocks 3 and 4 are also included here as the endmembers are spectrally similar. These two endmembers have some overlap, but for the most part define large spatially continuous regions that are distinct. This indicates that although the two endmembers appear to be rock-lichen mixtures, they include enough unique spectral information that they map out unique spatial regions.

2.6 Discussion

2.6.1 SSEE parameters, processing speed and performance

For SSEE there are a number of input parameters, which affect both processing speed and performance. The 2 key parameters are subset size and s (SVD threshold value). The actual subset size used will depend on the characteristics of the image, particularly the spectral contrast of the endmembers and their spatial distribution. The degree of homogeneity in the scene is also a factor in determining subset size. Larger subsets can be used in cases where endmembers are distributed as large homogeneous regions. For more complex scenes, smaller subsets are required. It may be possible to apply methods such as semi-variograms to help determine the appropriate subset size. If a scene contains only high contrast endmembers there is likely minimal benefit to using SSEE. In addition, SSEE will not be useful in cases where low contrast endmembers are always spatially associated, with respect to the subset size. The real benefit of SSEE comes when spectrally similar endmembers are spatially independent. This is evident with rock endmembers 5 and 6, 12 and 13, and lichen-rocks 3 and 4 as shown in Figure 2.12.

Choosing an appropriate subset size also effects processing speed. When using smaller subsets the number of basis vectors retained increases, such that projecting the data onto these vectors becomes the controlling factor with respect to processing speed. Subset sizes larger than 50x50 pixels significantly reduce processing speed because of the processing time necessary to obtain basis vectors via SVD. With larger subset sizes we also reduce our ability to obtain basis vectors that may be related to low contrast endmembers, therefore reducing performance. Thus, the user must balance information gained by reducing the subset size, knowing that many of the additional vectors are redundant. Based on work in this study we found that a subset size of 20 - 25 pixels was effective. For this analysis subsets did not overlap. However, it may be advantageous to use overlapping subsets, such that each pixel is compared equally to pixels in all directions. Subsets could also be of different sizes and shapes defined by the spatial complexity across the scene (e.g. quadtree decomposition). It may also be useful to preprocess the vectors to remove redundant vectors. However, this must done with care such that important vectors related to subtle spectral variations are not removed.

The second key parameter that affects performance is the parameter s. Values set lower than 0.01 resulted in additional basis vectors, many of which are related to noise and only increased computational time. Values that are set higher than 0.01 result in fewer vectors per subset (minimum of 2 in SSEE), which reduce our ability to select low contrast endmembers. Although more work is required to determine an s value that works best for all data sets, this analysis has shown that s can be determined based on the SNR.

The size of the spatial averaging window was set to be equal to the subset size. This was done originally for consistency. However, for larger subsets an equivalent spatial averaging window had a negative impact on the methodology, in that spatially independent endmembers that are spectrally similar may be averaged. In addition, a larger window can increase the number of updated candidate pixels, which can make spatial averaging impractical (see Table 2.1).

The last two parameters used in SSEE are spectral angle and RMS, which are used to update and average the candidate endmember pixels. For this project we used a spectral angle of 1 degree and an RMS value equal to 1% of absolute reflectance. Higher spectral angle and RMS values result in a larger updated candidate endmember list, but also may lead to the loss of the subtle spectral features that define a low contrast endmember. For this reason we chose to keep these two values to a minimum. Note that RMS is primarily used for dark pixels, such as water.

2.6.2 Comparison with PPI

Of the endmember extraction methods described in section 2, SSEE has most in common with PPI, even though AMEE also uses spatial information. The similarity between SSEE and PPI relates to the projection of the data onto vectors and retaining those pixels that lie at either end of the vectors. The primary benefit of SSEE compared with PPI is the use of non-random vectors. First and foremost is the fact that SSEE is repeatable. Secondly, fewer vectors are required. In addition, many of the vectors derived from adjacent subsets are redundant, so the actual number of important vectors is less than the total compiled and results in a smaller number of candidate pixels that the user must work with, compared with PPI. This is evident from the results, where for an equivalent number of random vectors a total of 489 candidate pixels were selected, as opposed to 148 for SSEE. For PPI, the use of random vectors results in more spectral variability among candidate pixels. For SSEE, basis vectors are only retained for each subset region if they explain a significant percentage of the spectral variance. This reduces the possibility of retaining basis vectors related to noise, and in turn, selecting pixels that are noisy.

Because of the high number and spectral variability of the PPI endmembers this requires a great deal of human intervention to derive a final endmember set. For SSEE human intervention is limited to grouping the non-duplicate endmember candidates. This step is simplified by reordering the list based on spectral similarity, and by using the spatial coordinates of each candidate endmember pixel.

Step 1 and 2 of the SSEE methodology makes use of projecting the data volume onto vectors to derive a set of candidate endmember pixels, as used with PPI. However, the key difference is that for SSEE the vectors are not random, but eigenvectors derived from image subsets. In doing so, the SSEE methodology by-passes the difficulty of setting an adequate threshold of eigenvalues encountered when analyzing an entire image by retaining only the top few vectors related to signal for each subset region. This approach makes use of the fact that eigenvectors are dependent on the scene statistics, and are thus, spatially dependent.

2.6.3 Local vectors versus local candidate pixels

It is possible to use the local vectors to select a set of local candidate pixels for each subset region. However, the key drawback of this approach is the necessity to filter through a much larger number of candidate pixels to determine an endmember set for the full image. These local candidate pixels may also be partial mixtures, which complicate the selection of endmembers. To account for this problem we have chosen instead to use local vectors. Then, in turn, scale up to the full image by projecting the data onto the compiled vector set.

2.7 Conclusions

The spatial-spectral endmember extraction tool (SSEE) presented in this paper makes primary use of spatial information to: 1) select local eigenvectors that relate to both high and low contrast endmembers within the scene; and, 2) to average only spectrally similar endmembers that are also spatially related. This results in a higher number of candidate endmembers that are defined both spectrally and spatially. The evaluation of SSEE has shown that the method is capable of extracting unique endmembers with subtle spectral variability that are not selected by other well known spectral-based methods. These unique endmembers were shown to be spectrally significant owing to comparisons with field spectra and through physically realistic spatial distribution.

The two key parameters that affect the processing speed and performance of SSEE are subset size and s (SVD threshold value). For the two evaluations use in this paper a subset size of 20 to 25 pixels squared and a s value of 0.01 were shown to be effective at selecting both high and low contrast endmembers. The use of local eigenvectors, rather than local endmembers, allows SSEE to retain local information, but also apply that information at the scale of the full image. The use of spatial subsets to select eigenvectors also allows SSEE to by-pass the problems associated with selecting a cutoff threshold between eigenvectors caused by signal versus those related to noise. However, the usefulness of SSEE is dependent on the spectral contrast and spatial distribution of the endmembers within the scene. Thus, SSEE is particularly beneficial for extracting spectrally similar endmembers that are also spatially independent. Overall the SSEE method is quick, repeatable, and requires minimal user input.

REFERENCES

Adams, J.B., Smith, M.O., & Johnson, P.E. (1986). Spectral mixture modeling: a new analysis of rock and soil types at the Viking Lander 1 site. *Journal of Geophysical Research*, 91, 8098-8112.

Adams, J.B., Smith, M.O., & Gillespie, A.R. (1993). Imaging spectroscopy: Interpretation based on spectral mixture analysis, In: C.M. Pieters & P.A. Englert (Eds.), *Remote Geochemical Analysis: Elemental and Mineralogical Composition,* Cambridge University Press, Cambridge, 145-166.

Adams, J.B., & Gillespie, A.R. (2006). *Remote sensing of landscapes with spectral images: A physical modeling approach*. Cambridge University Press, New York, 362.

Bateson A., and Curtiss, B. (1996). A method for manual endmember selection and spectral unmixing. *Remote Sensing of Environment,* 55, 229-243.

Berman, M., Kiiveri, H., Lagerstrom, R., Ernst, A., Dunne, R., & Huntington, J.F. (2004). ICE: A statistical approach to identifying endmembers in hyperspectral images. *IEEE Transactions on Geoscience and Remote Sensing*, 42, 2085-2095.

Boardman, J.W. (1993). Automating spectral unmixing of AVIRIS data using convex geometry concepts. *Summaries of the fourth Annual JPL airborne Geoscience Workshop*, JPL Publication 93-26, 1, 11-14.

Bowles, J., Palmadesso, P.J., Antoniades, J.A., Baumback, M.M., & Rickard, L.J. (1995). Use of filter vectors in hyperspectral data analysis. *Proceedings SPIE Infrared Spaceborne Remote Sensing III*, 148-157.

Chang, C-I., & Du, Q. (2004). Estimation of number of spectrally distinct signal sources in hyperspectral imagery. *IEEE Transactions on Geosciencce and Remote Sensing*, 42, 608-619.

Chang, C-I., & Plaza, A. (2006). A fast iterative algorithm for implementation of Pixel Purity Index. *IEEE Transactions on Geoscience and Remote Sensing Letters*, 3, 63-67.

Clark, R.N., Swayze, G.A., Livo, K.E., Kokaly, R.F., Sutley, S.J., Dalton, J.B., McDougal, R.R., & Gent, C.A. (2003). Imaging spectroscopy: Earth and planetary remote sensing with the USGS Tertracorder and expert systems. *Journal of Geophysical Research*, 108(E12), 5-1 to 5-44.

Cudahy, T. J., Okada, K., Ueda, K., Brauhart, P., Huston, D., Cocks, T., Wilson, J., Mason, J., & Huntington, J.F., (1999). Mapping the Panorama VMS-style Alteration and host rock mineralogy, Pilbara Block, using hyperspectral VNIR-SWIR data. *CSIRO report*.

Haskell K. H., & Hanson, R. J. (1981). An algorithm for C linear least squares problems with equality and C nonnegativity constraints. *Mathematical Programming*, C 21, 98-118.

Healey, G., & Slater, D. (1999) Models and methods for automated material identification in hyperspectral imagery acquired under unknown illumination and atmospheric conditions. *IEEE Transactions on Geosciencce and Remote Sensing*, 37, 2706-2717.

Ifarraguerri, A., & Chang, C-I. (1999). Multispectral and hyperspectral image analysis with convex cones. *IEEE Transactions on Geoscience and Remote Sensing*, 37, 756-770.

Jolliffe, I.T. (1986). *Principal component analysis*, New York, Spriger Verlag.

Keshava, N., & Mustard, J.F. (2002). Spectral unmixing. *IEEE Signal Processing Magazine*, January, 44-57.

Kruse, F.A. (2002). Comparison of AVIRIS and Hyperion for hyperspectral mineral mapping. *Presented at the 11th JPL Airborne Geoscience Workshop*, 4-8 March, Pasadena, California.

Nascimento, J.M.P., & Dias, J.M.B. (2005). Vertex component analysis: a fast algorithm to unmix hyperspectral data. *IEEE Transactions on Geoscience and Remote Sensing*, 43, 898-910.

Neville, R.A., Staenz, K., Szeredi, T., Lefebvre, J., & Hauff, P. (1999). Automatic Endmember Extraction from Hyperspectral Data for Mineral Exploration. *Fourth International Airborne Remote Sensing Conference and Exhibition / 21st Canadian Symposium on Remote Sensing*, Ottawa, Ontario, Canada, 21-24 June.

Plaza, A., Martinez, P., Perez, R., & Plaza, J. (2002). Spatial/spectral endmember extraction by multidimensional morphological operations", *IEEE Transactions on Geoscience and Remote Sensing*, 40, 2025-2041.

Plaza, A., Martinez, P., Perez, R., & Plaza, J. (2004). A quantitative and comparative analysis of endmember extraction algorithms from hyperspectral data. *IEEE Transactions on Geoscience and Remote Sensing*, 42, 650-663.

Press, W.H., Flannery, B.P., Teukolsky, S.A., & Vetterling, W.T. (1992). *Numerical recipes in C: The art of scientific computing*, 2nd edition, Cambridge University Press.

Rogge, D.M., Rivard, B., Zhang, J., Feng, J (2006). Iterative spectral unmixing for optimizing per-pixel endmember sets. *IEEE Transactions on Geoscience and Remote Sensing*, 44, 3725-3736.

Rogge, D.M., Rivard, B., Harris, J., & Zhang, J., (submitted) Application of hyperspectral data for remote predictive mapping, Baffin Island, Canada. *Economic Geology*.

Scharf, L.L., (1991). *Statistical Signal Processing, Detection estimation and time series analysis*. Addison-Wesley Publishing Company.

Settle, J.J., & Drake, N.A. (1993). Linear mixing and the estimation of ground cover proportions. *Inernational Journal of Remote Sensing*, 14, 1159-1177.

Staenz, K., Szeredi, T., & Schwarz, J. (1998). ISDAS - A System for Processing/Analyzing Hyperspectral Data; Technical Note. *Canadian Journal of Remote Sensing*, 24, 99-113.

St-Onge, M.R., Wodicka, N., & Lucas, S.B. (1999). Geology of McKeller Bay-Wight Inlet – Frobisher Bay area, southern Baffin Island, Northwest Territories. *Current Research*, 1998-C, Geological Survey of Canada, 43-53.

G.A. Swayze, R.N. Clark., S. Sutley, and A. Gallagher, Ground –truthing AVIRIS mineral mapping at Cuprite, Nevada, in Summaries of the Third Annual JPL Airborne Geosciences Workshop, Volume 1: AVIRIS Workshop, JPL Publication 92-14, p. 47-49, JPL, Pasadena, California, 1992.

Thai, B., Healey, G., & Slater, D. (1999). Invariant subpixel material identification in AVIRIS imagery. *In Proc. JPL AVIRIS Workshop*, JPL Publication 99-17, Pasadena, California, February.

Tsai, F., & Philpot, W. (1998). Derivative analysis of hyperspectral data. *Remote Sensing of Environment*, 66, 41-51.

Winter, M.E. (1999) Fast autonomous spectral endmember determination in hyperspectral data. *Proceedings of the Thirteenth International Conference on Applied Geologic Remote Sensing*, Vancouver, B.C., Canada, II, 337-344.

Winter, M.E., & Winter, E.M. (2000) Comparison of approaches for determining end-members in hyperspectral data. *IEEE Aerospace conference Proceedings*, 3, 305-313.

CHAPTER 3
ITERATIVE SPECTRAL UNMIXING FOR OPTIMIZING PER-PIXEL ENDMEMBER SETS[2]

3.1 Introduction

In hyperspectral imagery, the spectral signature of each pixel commonly comprises the combined measured reflectance of components within the sensors field of view. Spectral mixing is a problem inherent to remote sensing data, and as a result, few image pixels are spectrally "pure" (Settle and Drake, 1993), which complicates spectral identification and classification. This problem can be addressed by linear spectral mixture analysis (SMA), which classifies mixed pixels (Adams et al., 1986; Adams et al., 1993) by deconvolving (unmixing) each pixel spectrum into fractional abundances of its surface constituents, or endmember spectra. Applying linear SMA to a given mixture requires that endmembers occur as spatially segregated patterns (Keshava and Mustard, 2002), with multiple scattering involving several endmembers (non-linear mixing) being negligible. If this requirement is met, and the endmembers and their spectral signatures are known, linear SMA can be used to estimate fractional abundances for each pixel using approaches such as, the maximum-likelihood setup (Settle, 1996), constrained least squares (Heinz and Chang, 2001), using endmember bundles to address endmember spectral variability (Bateson et al., 2000), and using multiple endmember spectral mixture analysis (MESMA), which addresses per-pixel endmember variability (Roberts et al., 1998). Examples of the application of linear SMA can be found in studies by Sabol et al (2002), Lu et al (2004), Small (2001), Bierwirth et al (1999), Asner and Heidebrecht (2002), and Neville et al (2003).

Commonly endmember spectra used for linear SMA are selected from image data because: 1) available library and field spectra were not necessarily acquired under the same conditions as airborne or satellite image data; 2) important surface components may not be adequately represented in spectral libraries; and, 3) image endmembers have the advantage of being directly associated with surface components detectable in the scene. Selection of image endmembers that are good representations of the surface components is necessary for accurate unmixing. As such, a number of image endmember extraction tools have been developed and include pixel purity index (PPI) (Boardman, 1993), manual endmember selection tool (MEST) (Bateson and Curtiss, 1996), N-FINDR (Winter, 1999), optical real-time adaptive spectral identification system (ORASIS) (Bowles et al., 1995), convex cone analysis (CCA) (Ifarraguerri and Chang, 1999), iterative error analysis (IEA) (Neville et al., 1999), automated morphological endmember extraction (AMEE) (Plaza et al., 2002), iterated constrained endmembers (ICE) (Berman et al., 2004), and vertex component analysis (VCA) (Nascimento and Dias, 2005).

Typically, linear SMA is applied to each pixel using the endmember set obtained from the full image. The number of endmembers in this set can vary substantially (Gillespie, 1992) depending on the spectral complexity of a scene, the spatial scale, spectral resolution, and the number of bands in the image. Commonly this number is greater than the number of endmembers required to unmix a single pixel in the scene.

---

[2] A version of this chapter has been published. Rogge D., Rivard, B., Zhang, J., & Feng, J. (2006). Iterative spectral unmixing for optimizing per-pixel endmember sets. *IEEE Transactions on Geoscience and Remote Sensing*, 44, 3725-3736.

Abundances predicted using linear SMA are most accurate when only the endmembers that comprise a given pixel are used, with larger abundance errors occurring when either too few or too many endmembers are used (Heinz and Chang, 2001; Sabol et al., 1992). Fractional abundance errors owing to an excess of endmembers can be reduced if the image endmember set can be optimized on a per-pixel basis, where this optimized endmember subset, or pixel endmember set, is more representative for the given pixel. Adapting linear SMA to account for variability in the number of endmembers on a per-pixel basis is the focus of this study and should not be confused with endmember spectral variability, which is addressed in papers by (Bateson et al., 2000; Petrou and Foschi, 1999).

To account for variability in the number of endmembers on a per-pixel basis the method presented in this paper makes use of an iterative spectral mixture analysis (ISMA) to optimize the image endmember set on a per-pixel basis. We first apply the ISMA to a simulated image comprising randomly generated mineral mixtures generated with a known image endmember set and with a range of signal to noise ratios (SNR). The use of simulated data allows us to directly determine the accuracy of the per-pixel sets predicted. The results show that the ISMA can effectively select the most appropriate endmember set for each pixel. This, in turn, results in more accurate abundance estimations than achieved when the full image endmember set is used to unmix every pixel. Finally we apply the ISMA to a real hyperspectral data set collected by the AVIRIS sensor over Cuprite, Nevada.

3.2 Background

Linear spectral mixture analysis is based on the premise that a given mixture can be modeled using a set of linearly independent endmember spectra. To deconvolve a spectrum into fractional abundances of its constituent endmember spectra the following equation can be solved using a least squares approach,

$$R_b = \sum_{i=1}^{n} F_i S_{ib} + E_b \qquad (1)$$

where R_b is the reflectance of the pixel at band b, F_i is the fractional abundance of the endmember i, S_{ib} describes the reflectance of endmember i at band b, n equals the number of endmembers, and E_b is the error of the fit at band b. The least squares estimator used to solve equation 1 can generate fractional abundances that are positive or negative. In this case the linear unmixing solution is said to be unconstrained and is computationally simplistic. Unconstrained unmixing is particularly sensitive to the use of endmembers that are not part of the given mixture, resulting in solutions that are not physically realistic (e.g. negative fractions). If constraints are imposed, such that fractional abundances sum-to-one (ASC), and fractional abundances are non-negative (ANC), unmixing is computationally more complex. The simultaneous implementation of ASC and ANC is usually recommended to produce fractional abundances that are physically realistic (Heinz and Chang, 2001). The root-mean-square (RMS) error representing the "goodness of fit" for the modeled spectrum compared to the image spectrum can be calculated as:

$$RMS = \left(\frac{\sum_{b=1}^{k} (r_b - p_b)^2}{k} \right)^{\frac{1}{2}} \qquad (2)$$

where r_b and p_b are the modeled and image spectrum values at band b, respectively. k is the number of bands.

The concept of unmixing each pixel based on an optimal per-pixel endmember set has been presented in papers such as, (Adams et al., 1993; Roberts et al., 1998; Roessner et al., 2001; Gross, 1996; Ramsey and Christensen, 1998). In Adams et al (1993) and Roessner et al (2001) the authors made use of the spatial association of pixels to that of endmembers in the image and in Gross (1996) a hierarchial and stepwise spectral unmixing was presented. In Roberts et al (1998) and Ramsey and Christensen (1998), the unmixing process was used to determine which endmembers from a candidate endmember set are most appropriate to unmix a given mixture. The multiple endmember spectral mixture analysis (MESMA) described in Roberts et al (1998) made use of a candidate endmember set comprising spectra of vegetation and soils measured in the field and laboratory. For each pixel MESMA examined all possible combinations of models of 2 and 3 endmembers from the candidate endmember set. Endmember models were retained if they met three criteria: 1) the RMS error was below a pre-set threshold, 2) the unmixing model had physically reasonable fractions between –0.01 and 1.01; and, 3) each band residual did not exceed a predetermined threshold. It is possible that more than one endmember model can meet the 3 criteria of MESMA. This warrants additional steps to determine which of the combinations is most appropriate. In Roberts et al (1998) a subset of models was selected, which provided an optimal areal coverage. A problem arising from this approach is that multiple fractional output maps can result from models with different numbers of endmembers. In Okin et al (1999) and Li and Mustard (2003) a different approach was suggested whereby the endmember model with the lowest RMS error would be retained. This approach is reasonable if the number of endmembers are fixed for each model (Okin et al., 1999). However, if the number of endmembers is to be variable then the minimum RMS error cannot be used. This is because as additional endmembers are added to the model the RMS error will decrease, even if the endmember is not in the mixture (Ramsey and Christensen, 1998; Okin et al., 1999; Li and Mustard, 2003). To address this problem Li and Mustard (2003) suggested that the model with the fewest endmembers be used if the RMS error is lower than the noise. In (Roberts et al., 2003) the higher order endmember model is retained if the RMS error is 0.8% lower for models with more endmembers. Evaluating all possible combinations, verifying if each model meets the 3 criteria, and determining which of the candidate endmember models is optimal, makes MESMA computationally intensive (Roberts et al., 1998; Okin et al., 1999; Li and Mustard, 2003; Roberts et al., 2003; Okin et al., 2001; Painter et al., 2003; Dennison and Roberts, 2003).

In Ramsey and Christensen (1998) high resolution laboratory thermal emission spectra were used to test a number of factors that affect the applicability of SMA, notably blind endmember input. It was recognized that endmembers with negative fractional abundances are physically unrealistic, and likely not part of the mixture. Thus, their approach was to remove all endmembers with negative abundance fractions and repeat the unmixing process on the remaining endmember set until no negative abundances remain. This iterative approach is computationally less intensive than MESMA, but it cannot detect endmembers with positive fractions that are not part of the mixture. ISMA is an alternative approach that integrates the iterative concepts used in Ramsey and Christensen (1998) and the change in RMS as a function of the number of endmembers (Ramsey and Christensen, 1998; Okin et al., 1999; Li and Mustard, 2003; Roberts et al., 2003). The method does not require an examination of all possible endmember combinations thereby reducing the computational complexity; and, it can remove endmembers with positive, as well as negative abundances that are not part of a mixture, thus obtaining the optimal per-pixel endmember set. The following section describes the ISMA.

3.3 Iterative spectral mixture analysis

Once an image endmember set has been determined using one of the endmember extraction methods listed in section 1, the ISMA can be implemented to determine the optimal per-pixel endmember set and produce fractional abundance images for each endmember. To account for changes in the geometry of incident light caused by topography, a shade endmember was used in papers by Adams et al (1986), Keshava and Mustard (2002), Roberts et al (1998), and, Lu et al (2004). In Roberts et al (1998) a uniform reflectance/shade endmember was used, which can be considered a neutral multiplicative scaling factor (Keshava and Mustard, 2002). For the ISMA a shade endmember is also included with the image endmember set, as it is assumed that each mixture has some degree of shade. For each pixel in the image the implementation of the ISMA is in two parts: 1) iterative unmixing to remove endmembers one at a time; and, 2) determining the optimal endmember set by analyzing the change in RMS as a function of the number of endmembers (Figure 3.1). The first step of part 1 is to apply unconstrained linear unmixing using the pixel endmember set (step 2, Figure 3.1). From the unconstrained unmixing solution, the endmember with lowest abundance (positive or negative) is removed, excluding the shade endmember, which is retained for all iterations (step 3, Figure 3.1). If the number of pixel endmembers remaining is > 1, excluding the shade endmember, a new unmixing solution is calculated with the remaining endmembers. The process is repeated until one endmember and the shade endmember remain. Unconstrained unmixing is used instead of constrained unmixing because as the endmember set for a given mixture approaches the endmembers that actually comprise it, the predicted abundances should be similar to the actual abundances and should sum close to 1.

The second part of the ISMA involves an examination of the change in RMS error over all iterations to determine the critical iteration that uses too few endmembers (steps 5 - 7, Figure 3.1). The RMS error should be variable, but low, as long as the actual endmembers that comprise the mixture have not been discarded. However, once one of the actual endmembers is removed during the iterative process the RMS will increase substantially because too few endmembers are available to effectively model the mixture. This is the critical iteration and is determined automatically by calculating the change in the RMS error (ΔRMS) starting from the last iteration until ΔRMS is below a preset threshold. ΔRMS is calculated as,

$$\Delta RMS = 1 - \left(RMS_{it-1} / RMS_{it} \right) \qquad (3)$$

where RMS_{it} is the nth iteration RMS value. The search process begins with the last iteration because: 1) the actual number of endmembers necessary to unmix each mixture is likely much smaller than the maximum available and can be reached quickly; and 2) minor RMS variability observed for the first few iterations may exceed the ΔRMS threshold and prematurely stop the process. ISMA also requires the ΔRMS value to be below the threshold for a predetermined number of successive iterations before the process is halted. The optimal endmember set is then determined to be the first of these successive iterations and is used to calculate the pixel fractional abundances (step 8, Figure 3.1). The final outputs are endmember fractional abundance images.

For the ISMA the maximum number of necessary unmixing iterations per-pixel is defined by the endmember set. For example, a set of 10 image endmembers would require 10 unmixing iterations per-pixel. In comparison, 375 unmixing calculations would be required for each pixel to test all possible 2, 3, and 4 endmember combinations using MESMA. If the candidate endmember set becomes larger, the number of unmixing calculations for ISMA increases linearly, whereas for MESMA the number increases significantly faster.

3.4 Testing methodology

To assess the applicability of the ISMA we first examine the accuracy of the selected optimal endmember set and the resulting fractional abundances for simulated data described in the next section. For this data set per-pixel endmember sets and fractional abundances are known since they are used to generate the mixed spectrum of each pixel, thus, enabling a direct comparison with estimated pixel endmember sets and abundances. The average fractional abundance error (f_{avg}) is calculated as:

$$f_{avg} = \frac{\sum_{i=1}^{m} \sum_{j=1}^{n} \left| a_j - e_j \right|}{m} \qquad (4)$$

where n is the number of endmembers, m is the number of mixtures in the image; and, a_j and e_j are the actual and estimated fractions for endmember j, respectively. The number of endmembers in equation (4) can be variable, such that f_{avg} can be calculated for a group, or a single endmember. Equation (4) can also be adjusted for m, such that f_{avg} can be calculated for simulated mixtures that comprise any number of mixtures. Errors in the fractional abundances estimated with the ISMA are then compared with those obtained from least squares unconstrained and constrained unmixing using all available image endmembers; and, using the approach of (Ramsey and Christensen, 1998). The fully constrained unmixing approach of (Haskell and Hanson, 1981) was implemented using the Imaging Spectrometer Data Analysis System (ISDAS) (Staenz et al., 1998). A direct comparison with MESMA is not warranted, as it will be demonstrated that ISMA can effectively select the correct per-pixel endmember sets and obtain accurate abundance fractions, without the computational complexity of MESMA.

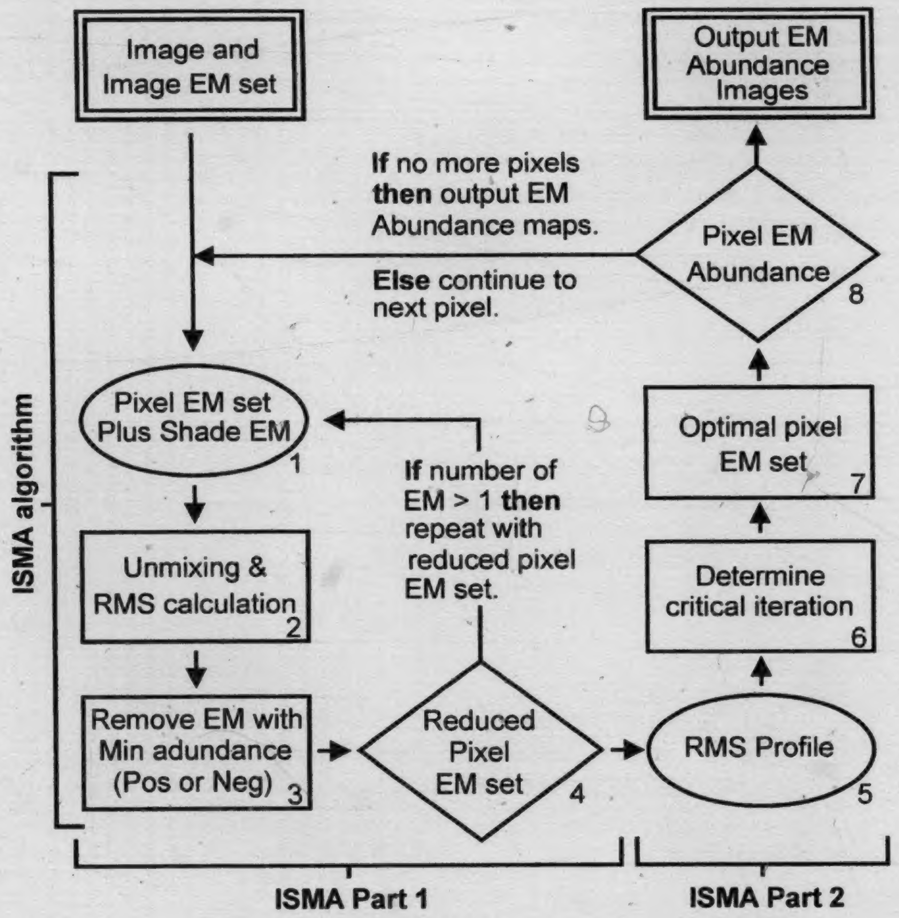
Image and Image EM set
Output EM Abundance Images
If no more pixels then output EM Abundance maps.
Else continue to next pixel.
Pixel EM Abundance
8
ISMA algorithm
Pixel EM set Plus Shade EM
1
If number of EM > 1 then repeat with reduced pixel EM set.
Optimal pixel EM set
7
Unmixing & RMS calculation
2
Determine critical iteration
6
Remove EM with Min adundance (Pos or Neg)
3
Reduced Pixel EM set
4
RMS Profile
5
ISMA Part 1
ISMA Part 2

Figure 3.1 Schematic representation of the ISMA. Input data sets include the hyperspectral image and the derived image endmember set. Steps 1 through 8 are applied pixel by pixel. Part 1 (steps 1 through 4) of the ISMA iteratively removes endmembers from the pixel endmember set based on minimum abundance until only 1 endmember and shade remain. Part 2 (steps 5 through 8) of the ISMA determines the critical iteration from the RMS profile generated in Part 1. The optimal pixel endmember set is used to unmix the given pixel spectrum, with results for all pixels output as endmember fractional abundance images.

A second test is presented using AVIRIS hyperspectral data for Cuprite, Nevada, an area where spectral endmembers have been reasonably well documented (e.g. Clark et al., 2003), but where fractional abundances are not known. To asses the fractional abundance maps generated using the ISMA, results should be physically realistic: 1) sum to 1 and 2) be non-negative. Histograms of the distribution of fractional abundances for individual endmembers, and for pairs of endmembers, are analyzed. These are compared with results from a fully constrained unmixing using all available endmembers.

3.5 Hyperspectral data sets

3.5.1 Simulated data set

The simulated data set comprises 10000 random linear mixtures generated from 29 mineral spectra obtained from the USGS spectral library (Clark et al., 1993) and a shade spectrum (Table 3.1). The 420 bands of each spectrum span 0.4 to 2.56 µm with an average spectral resolution of 0.005 µm (~0.002 in the visible to ~0.01 in the short-wave infrared). Spectra for common rock-forming minerals were chosen, including multiple spectra for actinolite, calcite, goethite, kaolinite, and muscovite (Table 3.1). The latter were used to test the robustness of the methodology to minor spectral variations of the same mineral.

For each mixture the combination of endmembers was randomly chosen. A shade endmember with uniform reflectance was included in all mixtures (1% of absolute reflectance). The simulated data has an average number of ~3.5 endmembers for all mixtures. The minimum and maximum number of endmembers for the mixtures are 1 and 12, respectively (excluding the shade endmember). The mixtures generated are mathematically correct, but are not necessarily geologically realistic (e.g. occurrence of magnesium rich olivine and quartz).

Noise was added to the random mixtures using a standard normal distribution of randomly generated numbers. SNR of 12:1, 25:1, 50:1, and 100:1 were used, assuming 50% absolute reflectance. The outcome was four data sets, each containing 10000 mixtures at a specific SNR. The noise was added using the following equation:

$$r'_b = r_b + \left(M * \left(\frac{q(0,1)}{SNR} \right) \right) \qquad (5)$$

where, r is reflectance, and q is a randomly generated number with a mean of 0 and a standard deviation of 1, and M is the assumed reflectance for the spectrum. For example, if reflectance is given as a value between 0 and 1, we can assign additive noise based on an assumed reflectance of 50%, or M = 0.5. The SNR values used in this paper are consistent with those used by Ifarraguerri and Chang (1999) and Harsanyi and Chang (1994), who used simulated data to test constrained unmixing methods with SNR ranging from 5:1 to 40:1; and, Plaza et al (2002) who used SNR of 10:1 to 110:1 to test endmember extraction algorithms. When we test the unmixing approaches with this data set, we use the same endmember set as used for the creation of the simulated mixtures (Table 3.1).

3.5.2 AVIRIS Cuprite hyperspectral data set

The Airborne Visible/Infrared Imaging Spectrometer (AVIRIS) sensor has 224 channels over the 0.37 to 2.51 µm spectral range with an average spectral resolution of ~10 nm. We use a 500 x 500 pixel subset of the June 19th, 1997 Cuprite calibrated data set available from the USGS. This data set has an average SNR of 100:1 at most wavelengths (Kruse, 2002). Of the 224 atmospherically corrected channels, we use 167 over the 0.4 to 2.42 µm spectral range. Channels not used are primarily associated with H_2O and OH absorption features near 1.4 and 1.9 µm.

Table 3.1: List of endmember spectra (from USGS Spectral Library (Clark et al., 1993)) used to generate the simulated data set. Minerals with multiple endmembers (EM) spectra are in bold.

EM no.	Library Name	Mineral Name	Library Details
1	**actinol1.spc**	**Actinolite**	**HS116.3B**
2	**actinol3.spc**	**Actinolite**	**HS315.4B**
3	albite3.spc	Albite	HS66.3B
4	almand1.spc	Almandine	HS114.3B
5	alunite1.spc	Alunite	GDS84 Na03
6	anorthi2.spc	Anorthite	HS201.3B
7	budding1.spc	Buddingtonite	GDS85 D-206
8	**calcite1.spc**	**Calcite**	**WS272**
9	**calcite2.spc**	**Calcite**	**HS48.3B**
10	chlorit5.spc	Chlorite	SMR-13.d 30-45um
11	dickite1.spc	Dickite	NMNH106242
12	epidote2.spc	Epidote	GDS26.b <75um
13	**goethit3.spc**	**Goethite**	**WS219 (limonite)**
14	**goethit4.spc**	**Goethite**	**WS220**
15	hematit2.spc	Hematite	GDS27
16	hornble1.spc	Hornblende_Mg	NMNH117329
17	**kaolini1.spc**	**Kaolinite**	**CM9**
18	**kaolini8.spc**	**Kaolinite**	**CM7**
19	montmor1.spc	Montmorillonite	SWy-1
20	**muscovi1.spc**	**Muscovite**	**GDS107**
21	**muscovi2.spc**	**Muscovite**	**GDS108**
22	olivine1.spc	Olivine	NMNH137044.a 160u
23	opal2.spc	Opal	TM8896 (hyalite)
24	quartz2.spc	Quartz	GDS31 0-74um fr
25	sphaler4.spc	Sphalerite	S26-34
26	sulfur.spc	Sulfur	GDS94 Reagent
27	talc1.spc	Talc	GDS23 74-250um fr
28	tremoli1.spc	Tremolite	HS18.3
29	zoisite.spc	Zoisite	HS347.3B
30	dark	1% of absolute reflectance	

3.6 Results

3.6.1 Example for one mixture

For the simulated data multiple ΔRMS values over successive iterations were tested, with a ΔRMS threshold of 5% over 2 successive iterations giving the best results. Figure 2 shows the spectrum of a single mixture and the spectra of the 5-endmember mineral spectra at a SNR of 500:1 (Figure 3.2A) that comprise it. The first unmixing iteration (it_1) with the ISMA uses the 29 endmembers listed in Table 1 as image endmembers, plus shade. Fractional abundances for each endmember for it_1 are shown in Figure 2b. Although there is a reasonable estimation of the abundances for the actual endmembers comprising the mixture, the endmembers that are not part of the mixture, have positive and negative abundances. The RMS error is calculated for it_1 (Figure

3.2C), followed by the removal of the endmember with the lowest abundance, in this case endmember 24 (refer to Figure 3.2B). The process continues until one endmember remains, excluding shade. Given the iterative nature of the ISMA, erroneous endmembers are removed first and those endmembers that comprise the mixture are retained. Examination of the change in RMS error through all iterations (Figure 3.2C) shows that RMS is relatively stable until it_{25}. After it_{25} the endmembers that comprise the actual mixture begin to be removed and the RMS error increases substantially. Iteration 25 is labeled the critical point on Figure 3.2C and marks the critical iteration between having too many and too few endmembers, which defines the optimal endmember set for the mixture. Requiring ΔRMS to be below the given threshold for 2 successive iterations ensures that the critical point is not mistaken as it_{28}, a local minimum. A comparison of the predicted abundances at it_1 (Figure 3.2B, 30 endmembers) and it_{25} (Figure 3.2D, critical point with optimal set of 5 endmembers plus shade) illustrates the impact of an appropriate selection of endmembers on the error in endmember fractional abundance. The fractional abundances at it_{25} are within 0.01 of the actual abundances and sum to 0.98.

3.6.2 Results for simulated data

3.6.2.1 *RMS profile characteristics*

Figure 3.3 displays the average RMS error as a function of iteration for all mixtures at each SNR. This Figure illustrates the consistent characteristics (e.g. critical point) of the RMS profiles. The profiles show that the predicted average number of endmembers required to unmix each mixture is between 3 and 4, which is consistent with the actual average for the simulated data sets. The profiles for the individual mixtures have 3 principle characteristics: 1) minor RMS variability over the first few iterations; 2) stable RMS over the mid-range iterations until the critical point; and, 3) substantial increase in RMS after the critical point. We observe two exceptions to the characteristic RMS error profile: 1) instances with no substantial increase in RMS; and, 2) a local minimum after the RMS increases substantially (refer to Figure 3.2C). The first case is observed for mixtures that comprise only 1 endmember. The second may be attributed to the order of endmember removal and the actual abundance fraction of a given endmember to the mixture.

3.6.2.2 *Proportion of correctly selected endmembers*

For each mixture the endmembers selected by ISMA and the method of Ramsey and Christensen (1998) are compared with the actual endmembers used in the simulation, and a proportion of correctly selected endmembers calculated (proportion correct = #correct / #selected). At high SNR (100:1) the average proportion of correctly selected endmembers for all mixtures was 96% using ISMA (Table 3.2). This value drops to 83.8% at a SNR of 12:1. The method of Ramsey and Christensen (1998) resulted in values ranging from 46.3 to 38.9% for these SNR values. On average, the number of endmembers underestimated by the ISMA was 0.24 to 1.31 at SNR of 100:1 and 12:1, respectively. The method of Ramsey and Christensen (1998) fared more poorly and overestimated the actual number of endmembers by a factor of 2 at each SNR. For both methods the number of endmembers missed increases with decreasing SNR. Unconstrained and fully constrained unmixing methods are not included in Table 3.2, as each uses all 30 endmembers to process the data.

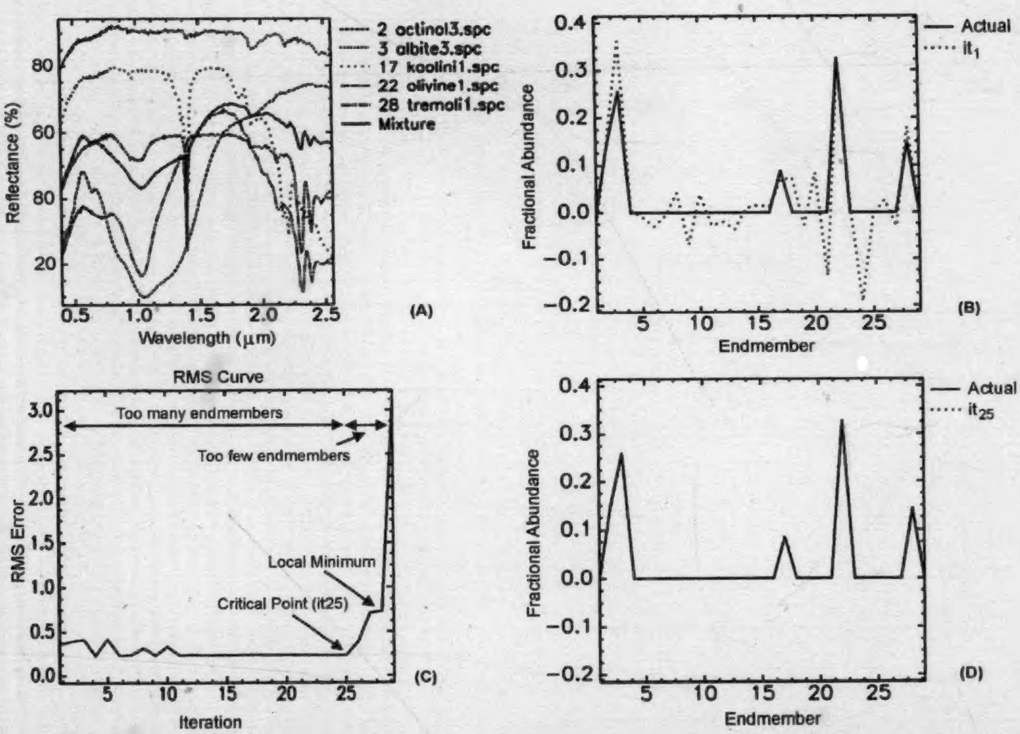

Figure 3.2 Graphical representation of the RMS error as a function of the number of iterations for a mixture of 5 endmembers (A) showing critical point at iteration 25 (it_{25}) and local minima at it_{27}-it_{28} (C). Note the RMS variability for the early iterations where an excess of endmembers are used to unmix the given mixture. (B) and (D) show a comparison between actual endmember abundance (solid line) and estimated abundance for it_1 (all endmembers) and it_{25} (critical point), respectively. Note negative and false positive abundances in (B) for the endmember set used in it_1, which is equivalent to results from an unconstrained unmixing using the 29 available endmembers and shade listed in Table 1. Note that the abundances using the endmembers at it_{25} (D) are within <0.01 of the actual fractions and sum to 0.98.

Table 3.2: Average number of endmembers selected, proportion correctly selected, and average number of endmembers missed for ISMA and the method given in (Ramsey and Christensen, 1998). Values are reported as averages for all mixtures at a given SNR.

	ISMA			R&C, 1998		
SNR	# selected	proportion correct	# missed	# selected	proportion correct	# missed
100	3.23	96.0	0.32	7.20	46.3	0.17
50	3.02	94.1	0.61	7.04	44.8	0.35
25	2.65	90.7	1.06	6.67	42.8	0.67
12	2.16	83.8	1.67	6.14	38.9	1.13

Actual average number of endmembers = 3.47

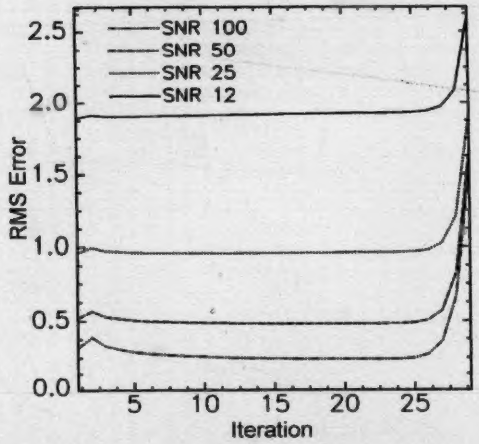

Figure 3.3 Average RMS profile for all mixtures at SNR of 100:1, 50:1, 25:1, and 12:1. On average each pixel can be effectively modeled with 3 to 4 endmembers.

3.6.2.3 *Average fractional abundance errors*

Equation (4) was used to calculate the average fractional abundance error (f_{avg}) for the simulated data at each SNR, where n = 29 (all endmembers excluding shade) and m = 10000 (all pixels). ISMA resulted in lower f_{avg} at all SNR compared with the method of Ramsey and Christensen (1998) and fully constrained unmixing, with the exception of constrained unmixing at a SNR of 12:1 (Figure 3.4). All three methods have average fractional abundance errors that are significantly less than that of the unconstrained unmixing method at all SNR (Figure 3.4 inset). The results demonstrate the impact of unmixing using the correct endmembers for each mixture.

When f_{avg} is calculated for each endmember (n = 1, m = 10000) the average fractional abundance error for all mixtures shows a dependency with respect to the given endmember (Figure 3.5). The largest error is observed for endmembers with few or no spectral features (#3 albite, # 6 anorthite, and # 24 quartz) (Figure 3.6). This is consistent with least squares theory in that in cases where endmembers are similar or featureless, the endmember matrix will be ill conditioned. For these three endmembers the results do not enable the selection of a better method amongst the constrained, ISMA or the method of Ramsey and Christensen (1998). Endmembers with numerous spectral features consistently display a low fractional abundance error (e.g. #4 almandine, #5 alunite, #29 zoisite). These endmembers have a lower error for the ISMA than for the fully constrained approach and the method of Ramsey and Christensen (1998). Similar characteristics are observed for the three methods at all SNR investigated, with errors increasing as SNR decreases.

At a SNR of 100:1 the sum of fractional abundances obtained from the ISMA ranged from 0.95-1.05 for 89% of the mixtures and this value fell to 76%, 58% and 37% at a SNR of 50:1, 25:1, and 12:1 respectively (Figure 3.7). The number of mixtures that had negative fractional abundances was 9, 6, 7, and 7 for data sets with SNR of 100:1, 50:1, 25:1, and 12:1, respectively. Of these, only one mixture showed a negative fractional abundance exceeding 0.01. These results show that ISMA can produce physically realistic abundance fractions for the majority of pixels by correctly selecting per-pixel endmember sets, particularly at higher SNR. This is accomplished without the need to impose abundance non-negative and sum to 1 constraints (ANC and ASC).

3.6.2.4 *Dependency of the error on the number of endmembers in the mixture*

Figure 3.8 shows the average fractional abundance error as a function of the number of endmembers in the simulated mixtures. Pixels that comprise 10, 11, and 12 endmembers were excluded from this analysis because they are represented by too few mixtures (7, 2, and 1 respectively). For the constrained unmixing method and the ISMA, f_{avg} increases as more endmembers are included in the mixture. For the unconstrained unmixing method the error remains stable (Figure 3.8A inset), but is significantly larger than for the other two methods. At higher SNR the ISMA performs better than the constrained unmixing method when fewer than 7 endmembers comprise a mixture, with half the error when mixtures comprise 3-5 endmembers. At a SNR of 12:1 the only improvement observed is for mixtures with fewer than 3 endmembers. For both methods the lowest error occurs if a single endmember comprises the mixture regardless of the SNR. These results clearly demonstrate the direct influence of the number of endmembers on the predicted fractional abundances.

3.6.2.5 *Dependency of the error on multiple endmembers for the same mineral*

The average fractional abundance errors obtained from the constrained and ISMA methods were compared for mixtures that included multiple endmembers of the same mineral (e.g. muscovi1.spc and muscovi2.spc). Overall, the constrained unmixing method resulted in lower fractional abundance errors than the ISMA method at low SNR (<50:1). At higher SNR the difference in the errors between both methods was small and on the order of 0-0.01 (Figure 3.9). For the ISMA method the highest errors occur when one or both of the similar endmembers have low fractional abundance (e.g < 0.05). For larger abundances (e.g. > 0.1) the error decreases and approaches that of the constrained unmixing method. This change in error as a function of actual abundance is not observed in the constrained unmixing results.

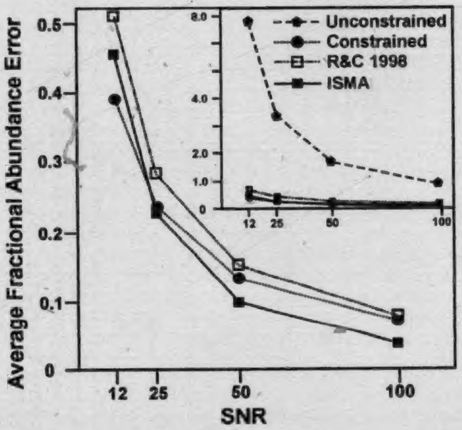

Figure 3.4 Average fractional abundance error between actual and estimated abundances for all endmembers and pixels calculated for the method of [29] (R&C 1998); constrained and unconstrained (inset) unmixing using all 30 endmembers; and, the ISMA.

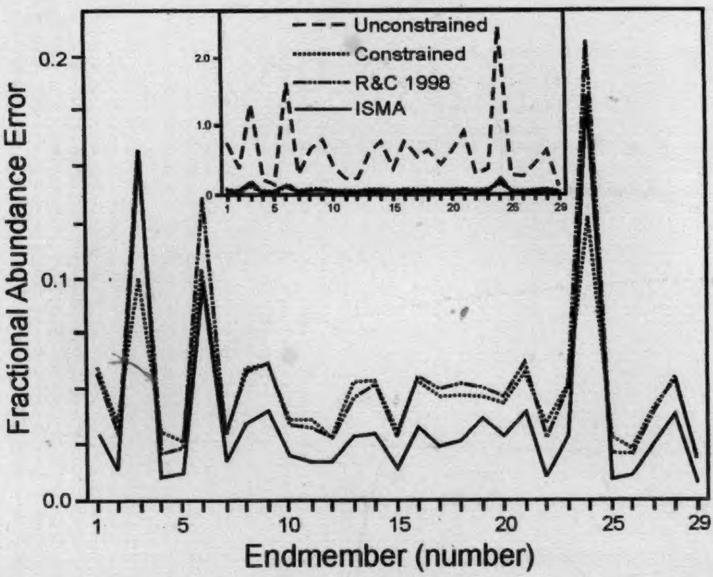

Figure 3.5 Average fractional abundance error at a SNR of 50:1 for each endmember for all mixtures for the method of [29] (R&C 1998); constrained and unconstrained unmixing using all endmembers; and the ISMA. The inset includes results for the unconstrained unmixing approach. Refer to Table 1 for the mineral corresponding to the endmember number.

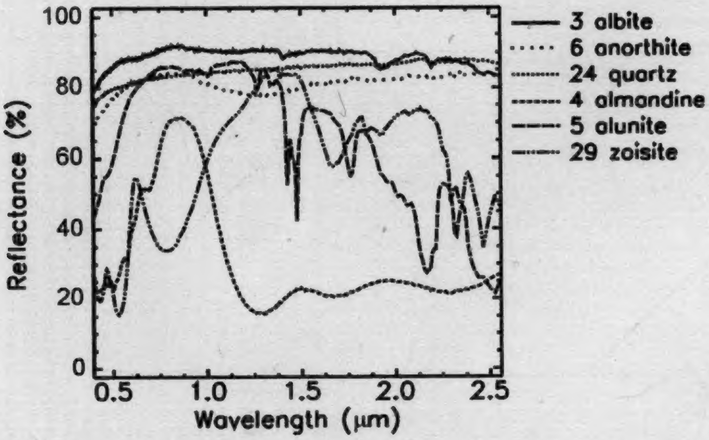

Figure 3.6 Selection of endmember spectra with differing spectral contrast. Endmembers with numerous spectral features (almandine, alunite, zoisite) result in low fractional abundance errors (Figure 5), whereas high fractional abundance error is associated with endmembers with few spectral features (albite, anorthite, quartz).

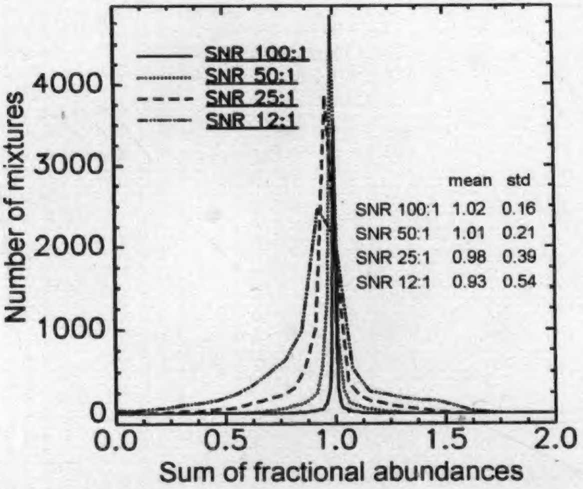

Figure 3.7 Histograms distribution of the sum of fractional abundances obtained from the ISMA for each of the 10000 mixtures at SNR of 100:1, 50:1, 25:1, and 12:1.

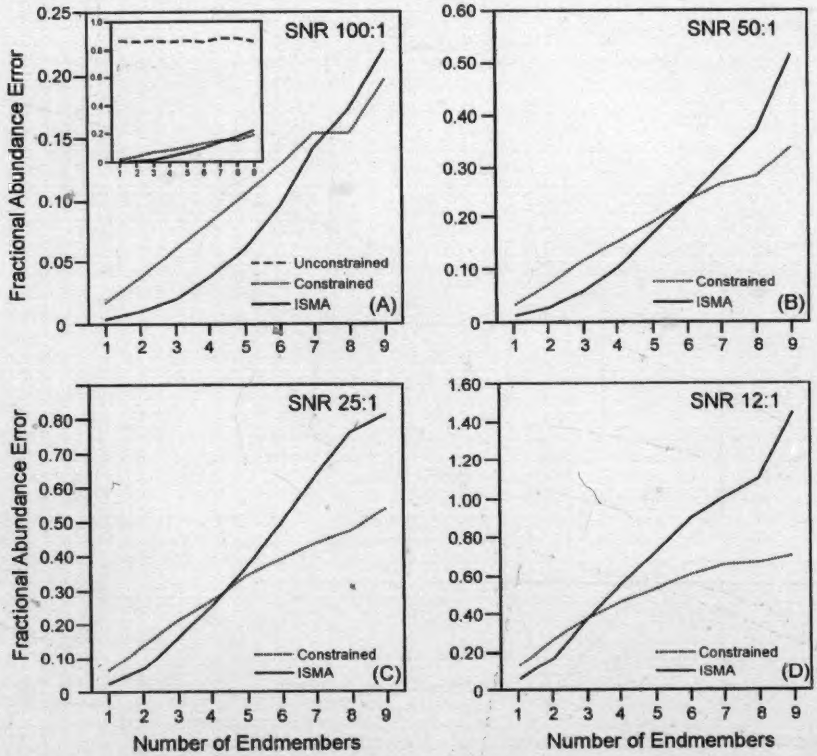

Figure 3.8 Average fractional abundance error as a function of the number of endmembers in a given mixture for SNR of (a) 100:1, (b) 50:1, (c) 25:1, and (d) 12:1. Unconstrained unmixing included in inset of (a) for SNR of 100:1.

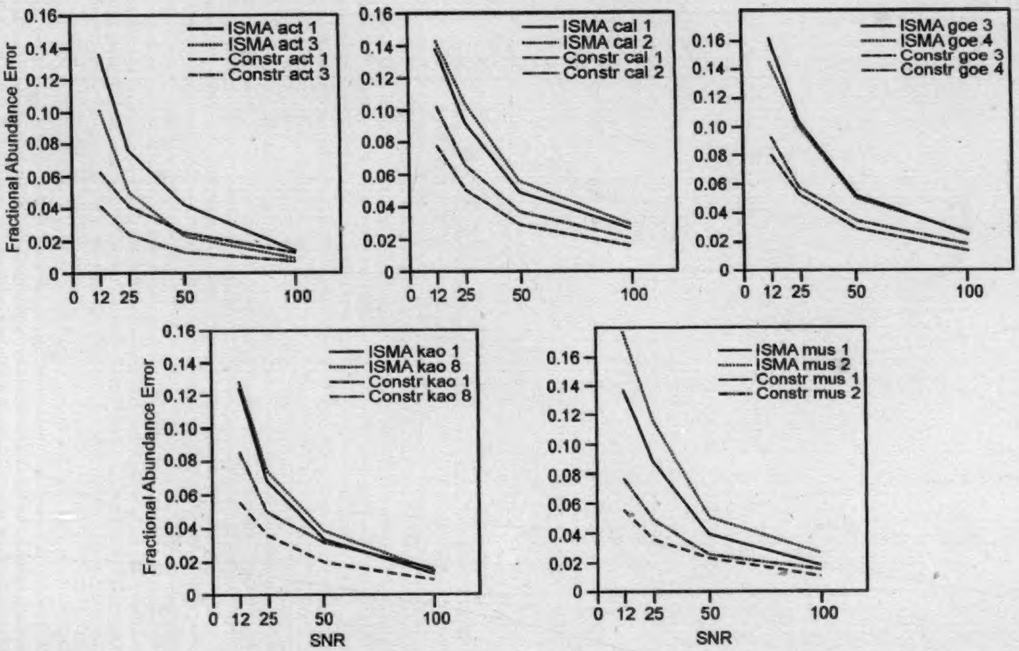

Figure 3.9 Average fractional abundance error for mixtures containing multiple endmembers for the same mineral (refer to Table 1). Act=actinolite, cal=calcite, goe=goethite, kao=kaolinite, mus=muscovite.

3.6.3 Results for the AVIRIS Cuprite data set

A total of 30 endmembers were extracted from the AVIRIS Cuprite data set using the IEA (Neville et al., 1999) extraction tool available in ISDAS (Staenz et al., 1998). Of the 30 endmembers, two were noisy spectra and were removed from the list. A shade endmember with uniform reflectance of 1% absolute reflectance was used rather than the darkest pixel in the image because the later had an average reflectance of 14% and a notable spectral shape. The remaining endmembers were used to unmix the data, including spectra with similar overall shape, but with subtle variations over specific spectral regions. For the Cuprite data a number of ΔRMS threshold values were tested, including the 5% value used for the simulated data. However, a ΔRMS threshold of 15% over 2 successive iterations was found to be more appropriated for the real data set.

A visual comparison of the fractional abundance maps generated using ISMA and a fully constrained unmixing shows similarity in the broad spatial distribution of abundance fractions, with more noticeable differences occurring locally, or between endmembers with similar spectral features (Figure 3.10). The ISMA fractional abundance maps are also consistent with validated mineral maps produced using Tetracorder for the data set (Clark et al., 2003). For the ISMA fractional abundance maps, 98.9% of the pixels are non-negative and 93% sum to < 1.01 (excluding shade) (Figure 3.11). Of the pixels that sum > 1.01, only 1.4% (3565 pixels) sum to > 1.1. Histograms of the fractional abundances for each endmember show that low abundance values dominate the fully constrained unmixing solution (Figure 12a). These low abundances are attributed to endmembers being used to improve the goodness of fit of the model, but that are likely not part of a given mixture. This is based on knowledge of the spatial distribution and characteristics of the known minerals and mineral assemblages in the area derived from existing work, such as Clark et al (2003). For example, a number of known minerals in the region are spatially confined to alteration zones (e.g. buddingtonite and chalcedony), and not distributed evenly throughout the image. Yet analysis of the abundance histograms and abundance images, for fully constrained unmixing, indicate a large number of pixels with low abundance values (e.g. < 10%) that are distributed outside these alteration zones. For fully constrained unmixing 96% of the pixels are modeled by ≥5 endmembers, in contrast with 37% using IMSA. Figure 3.12 also shows that the frequency distributions of endmember fractions is not truncated when calculated using ISMA. For ISMA multimodal distribution are observed and there is also a distinctive shift to higher mean fractional abundances. This may be attributed to fewer endmembers being used to model each mixture, where each endmember contains spectral information that is relevant to the given mixture.

Geological map units are defined in part based on characteristics of their mineralogy and mineral abundance. The fractional abundance maps show the nonrandom spatial distribution of minerals (Figure 3.10). Scatter plots of fractional abundances for the selected region are shown in Figure 3.13 and reveal useful information for mapping, particularly for results obtained from the ISMA. In the case of the ISMA results, the scatter plots reveal clusters of pixels with similar mineral abundances corresponding to mappable units (e.g. Figure 3.13C). The same scatter plots for the fully constrained results lack well-defined clusters and the abundances are predominantly low reducing their value as a mapping tool.

3.7 Discussion

The results of this study provide a comparison of per pixel endmember sets and abundance determination obtained from the ISMA and other unmixing approaches. For the simulated data, the variable of greatest impact on each of the unmixing methodologies is SNR, which is not unexpected. The ISMA outperformed the other methods at SNR > 50:1, a value exceeded by current airborne systems (e.g. AVIRIS, HyMAP), which have published SNR averaging > 1000:1 in the visible and > 500:1 in the SWIR (Kruse, 2002; Cocks et al., 1998). SNR for the Hyperion satellite hyperspectral sensor is as high as 100:1 in the visible, but ranging from 50:1 to 25:1 in the SWIR, depending on the date of acquisition (Kruse, 2002). With a SNR approximating 50:1 ISMA should still be effective for selecting the optimal endmember set and reducing errors in fractional abundances. The simulated data results also indicate the impact of the number of endmembers that comprise a given mixture on the errors in the estimated fractional abundances. At SNR > 50:1, the ISMA has lower errors in fractional abundances if fewer than 6 endmembers comprise the mixture, with the greatest improvement for 3 – 4 endmembers. The number of image endmembers comprising a pixel will fluctuate as a function of the scene and the spatial resolution of the image. However, it is reasonable to assume that this number will typically be less than 7 endmembers (excluding shade), but likely closer to 3 or 4. As such, ISMA is particularly well suited to unmix the majority of pixels using existing hyperspectral sensors.

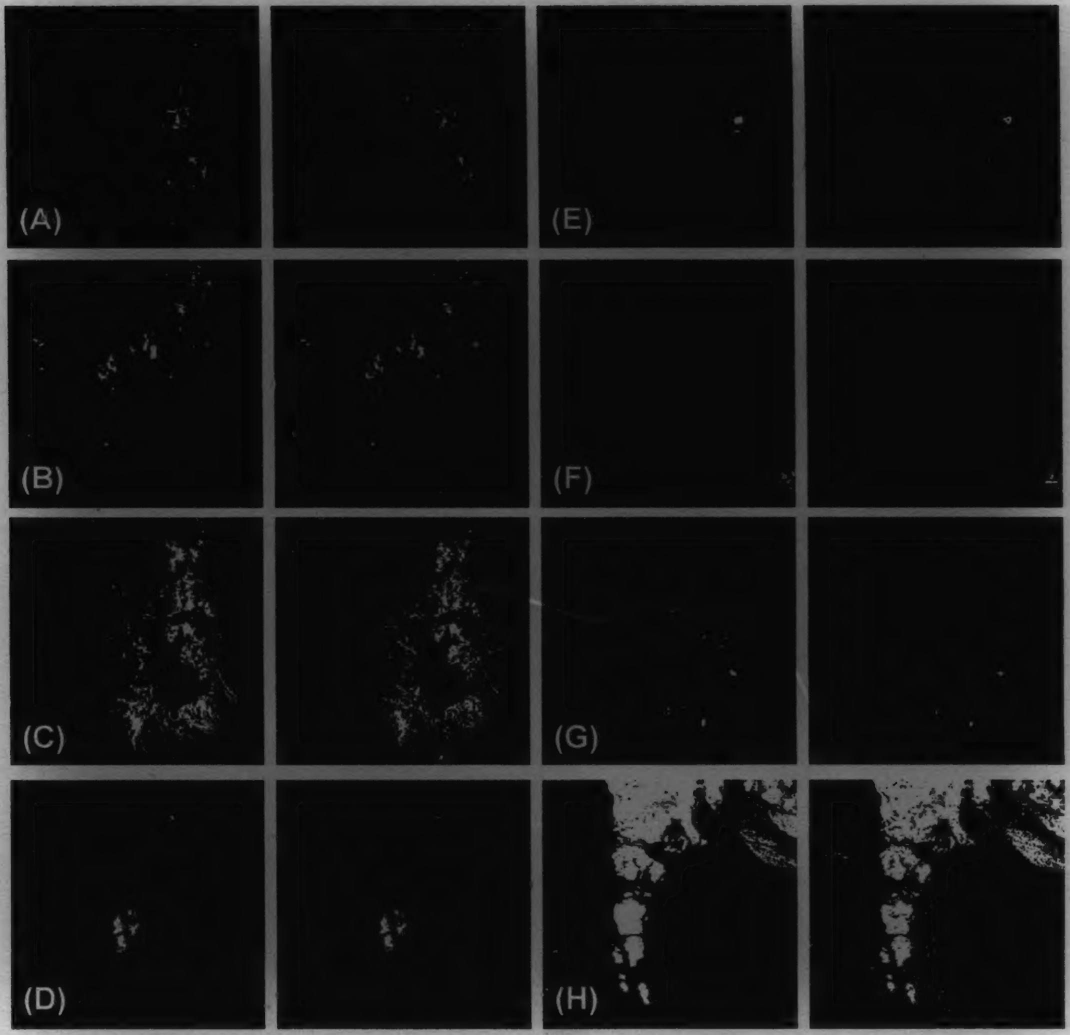

Figure 3.10 Selected endmember fractional abundance maps for a subset of the image. Fully constrained unmixing (left column), ISMA (right column). (A) Chalcedony 1, (B) Kaolinite, (C) Alunite 1, (D) Buddingtonite, (E) Chalcedony 2, (F) Montmorillonite, (G) Alunite 2, (H) desert varnish. Images are linearly stretched from 0 – 0.5.

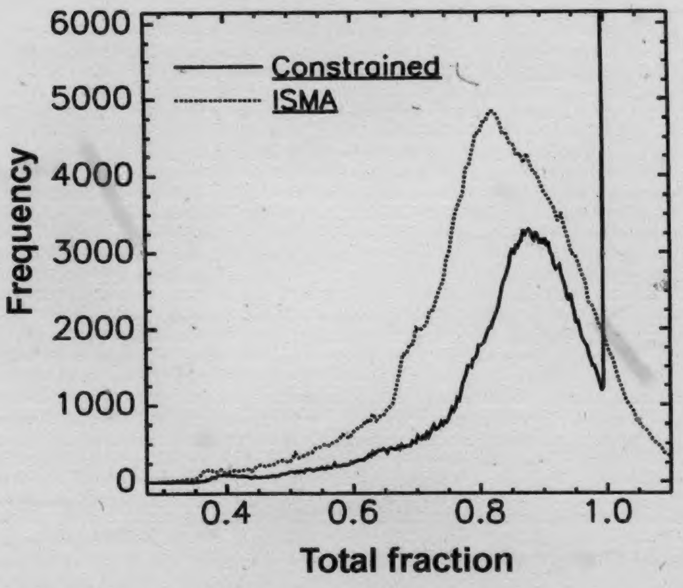

Figure 3.11 Histogram showing the distribution of total fractional abundance (excluding shade) for fully constrained and ISMA unmixing methods using the Cuprite hyperspectral data.

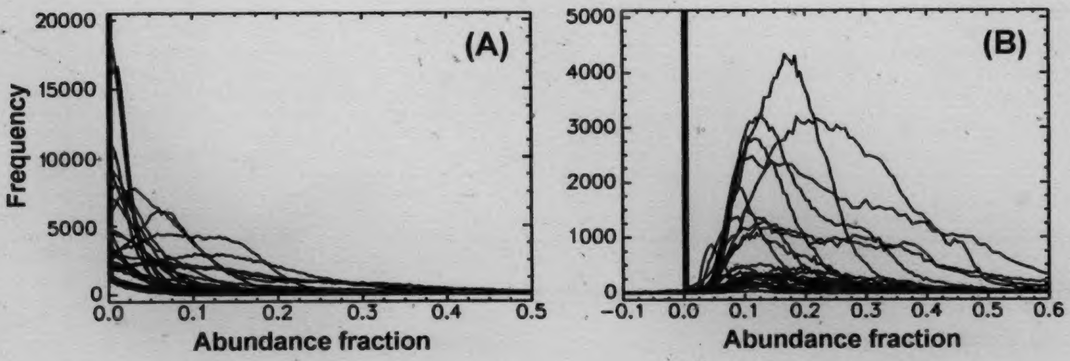

Figure 3.12 Histograms of fractional abundance values for each endmember for fully constrained (A) and ISMA (B) unmixing results of the Cuprite data set. Note vertical and horizontal scales are different for the two plots.

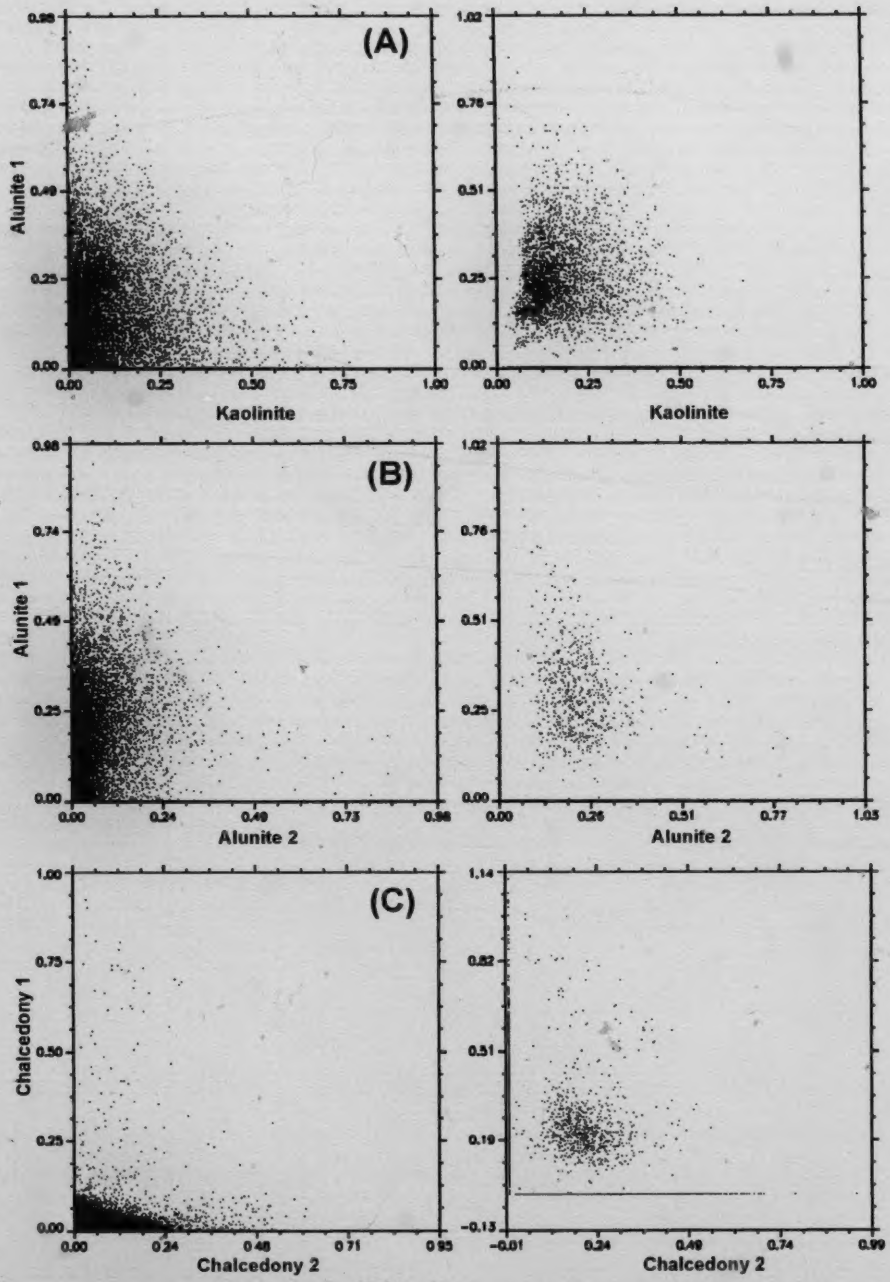

Figure 3.13 Scatter plots of fractional abundances obtained using fully constrained unmixing (left column) and ISMA (right column). (A) Kaolinite and Alunite 1; (B) Alunite 1 and 2; (C) Chalcedony 1 and 2 (refer to Figure 10). Note the vertical and horizontal scales in the left and right columns and ISMA results that include a few negative and > 1 values.

The ISMA exploits the characteristic variation in RMS errors as a function of the numbers of endmembers utilized to solve a mixture. The RMS error profiles have consistent characteristics independent of SNR, specifically the critical point, which rarely corresponds to the lowest RMS error. The consistent pattern of the RMS error profiles allows for a high degree of confidence in using the ΔRMS for selecting the critical point, and in turn, the optimal endmember set. However, based on the analysis of simulated data, if endmembers have very low fractional abundances, the RMS error increase after the critical point may be minimal and may impact the search for the critical point. In such circumstances if the ΔRMS parameter is set too high the ISMA will underestimate the number of endmembers. On the other hand, decreasing the ΔRMS may cause an overestimation of the number of endmembers in other mixtures. The parameters used for the simulated data gave accurate results, though on average slightly underestimated the number of endmembers. For the real data set it was observed that a slightly higher ΔRMS performed best. Thus, further analysis is required to determine what parameters are optimal for most data sets. However, based on the design of ISMA, once an RMS profile has been generated, multiple fractional abundance maps can be created for various ΔRMS without the necessity of repeating the iterative unmixing process.

The RMS profiles also show that the RMS error is low for the midrange of iterations prior to the critical point suggesting that the corresponding endmembers do not have a great influence on the modeled mixture, but do minimize the RMS error by adjusting for subtle spectral detail and noise. This characteristic may explain why the method of Ramsey and Christensen (1998) consistently overestimates the number of endmembers, where for each mixture there exists a set of endmembers with positive fractional abundances that reduce the RMS error, but are not part of the mixture. If incorrect endmembers are retained, the error in fractional abundance increases for the correctly selected endmembers. Thus, we suggest that the critical point is a better representation of the optimal endmember set than just considering negative abundance fractions.

Determining the critical point from the RMS profiles is computationally insignificant compared to the unmixing process. For ISMA, the computational load is controlled by the number of unconstrained unmixing iterations required to build the RMS profile. Thus, the computational load is directly dependent on the number of endmembers in the given scene. This is also the case for MESMA but as the number of endmembers increases, the number of mixing combinations increases substantially, whereas for ISMA the increase is linear. In addition, MESMA is affected by the number of endmembers comprising a pixel, such that if endmember combinations ≥4 (excluding shade) are required the computational complexity becomes a burden. For ISMA, the number of endmembers in each pixel has no effect on computational efficiency. ISMA represents an alternative to MESMA, in which ISMA has the capability of correctly selecting per-pixel endmember sets and produce accurate abundance fractions, while at the same time significantly increasing computational efficiency and operational simplicity. It is noted here that MESMA was originally designed to run using an appropriate endmember library derived from field and laboratory spectra (Roberts et al., 1998), whereas ISMA is designed to run using image endmembers.

Endmember extraction algorithms commonly retrieve a larger number of endmembers that include noisy spectra and spectra with similar overall shape. Noisy spectra are generally easy to identify and can be removed from the list. In the case of similar spectra, determining which endmembers should be retained for unmixing can be more problematic. Inherent to ISMA is its ability to complete this task automatically, but more importantly it is designed to do this on a per-pixel basis.

Depending on the image a complete endmember set may not be possible. Missing endmembers will have a similar effect on the ISMA RMS profile as the removal of actual endmembers through the iterative process. However, the increase in RMS attributed to the missing endmember will occur across the profile. Missing endmembers will likely reduce fractional abundance accuracy, regardless of the unmixing approach. Missing endmembers may in part explain the necessity in this study to increase ΔRMS for the real data. However, additional simulated tests are necessary to verify the full effects of missing endmembers.

In order to obtain physically realistic fractional abundances (non-negative and summing to 1) unmixing methodologies have focused on imposing ANC and ASC. However, using the ISMA no constraints were required to obtain physically realistic fractional abundances for both the simulated and real data sets. This is a result of effectively selecting the optimal per-pixel endmembers sets and demonstrates the importance of using the correct endmembers to unmix individual pixels.

The results for the Cuprite data set are interesting in that both fully constrained and ISMA result in physically realistic abundance fractions (sum to 1 and non-negative) and show similar map patterns of abundances, yet the two differ with respect to abundance values and their histogram distributions. Most notable are 2 interrelated differences: 1) the number of endmembers used to model each pixel; and, 2) a shift to higher mean abundances for ISMA results. The first difference is key, in that for fully constrained unmixing additional endmembers are used to reduce the residual error. This results in a high proportion of pixels with low abundance fractions. For ISMA, endmembers are only retained if their spectra contain information that can significantly reduce the RMS error, which results in each endmember comprising a reasonable fraction of the mixture. Although the fractional abundances cannot be verified without ground truth data, ISMA allows for a better discrimination of those endmembers that are likely to occur within a given pixel, as opposed to those that simply reduce the residual error. Selecting accurate per-pixel endmember sets is particularly important for minimizing errors in mapping. The abundance and presence of endmembers that comprise a large fraction of a given pixel are easily determined, but an endmember that comprises a small fraction of a pixel is more problematic and its presence may be missed. These cases are of particular interest to users as the accurate selection of per-pixel endmember sets can significantly impact the ability to map the spatial distribution of an endmember of interest.

One topic that was not addressed in this study, but should be briefly mentioned, is the issue of endmember uniqueness and variability in the context of multispectral systems. For hyperspectral and multispectral systems the number of possible unique endmembers is determined as the number of bands plus 1. For multispectral systems such as Landsat, which generally have less than 7 statistically independent dimensions, the number of unique endmembers is restricted, and will likely be fewer than what occurs in the scene. The forced restriction to a few spectral components does not allow for proper consideration of the spectral variability related to intraclass differences. Thus, the solution for ISMA, as with any other unmixing algorithms, will be under-determined.

3.8 Conclusions

The results of this study illustrate that the ISMA methodology developed in this paper is an effective tool to account for the per pixel variability in image endmembers necessary to unmix individual pixels. Based on analysis of simulated data the method correctly selects the optimal endmember set 96% and 83.8% of the time for SNR of 100:1 and 12:1, respectively. The accurate selection of an optimal endmember set at high SNR (100:1) reduces errors in fractional abundances compared to that obtained from unmixing using the full endmember set. At SNR > 50:1 the ISMA produced results with fractional abundances that sum close to 1 and are not negative. Compared with an unconstrained unmixing, the ISMA significantly reduces fractional errors. The ISMA produces lower abundance errors compared with a fully constrained unmixing for physically realistic mixtures (e.g. < 7 endmembers) at SNR lower than that of available airborne sensors and consistent with that of satellite hyperspectral sensors. Compared with the method of Ramsey and Christensen (1998), the ISMA removes endmembers with low positive abundance fractions that are not part of a given mixture, thus minimizing false detection.

The results for the Cuprite data set show that both fully constrained and ISMA result in physically realistic abundance fractions with similar map patterns, yet they differ with respect to the abundance values and their detailed distribution. This difference is a result of ISMA only retaining endmembers that contain spectral information that is relevant to the given mixture, and not noise. This impacts the ability to map the spatial distribution of an endmember of interest.

ISMA and MESMA are designed with the same objective in mind, with the key difference between the two being computational complexity. Although MESMA has been shown to produce good results, the computational complexity of the method (Roberts et al., 1998; Okin et al., 1999; Li and Mustard, 2003; Roberts et al., 2003; Okin et al., 2001; Painter et al., 2003; Dennison and Roberts, 2003) is a major drawback. The results from this study have demonstrated that selecting the correct per-pixel endmember set and produce accurate abundance fractions can be accomplished using the less computationally intensive ISMA method. It has also shown that imposing constraints on the unmixing process to obtain physically realistic solutions is not a necessity if an accurate per-pixel endmember set is used. The ISMA method is straightforward, easy to implement and has minimal user input.

REFERENCES

Adams, J.B., Smith, M.O., & Johnson, P.E. (1986). Spectral mixture modeling: a new analysis of rock and soil types at the Viking Lander 1 site. *Journal of Geophysical Research*, 91, 8098-8112.

Adams, J.B., Smith, M.O., & Gillespie, A.R. (1993). Imaging spectroscopy: Interpretation based on spectral mixture analysis, In: C.M. Pieters & P.A. Englert (Eds.), *Remote Geochemical Analysis: Elemental and Mineralogical Composition,* Cambridge University Press, Cambridge, 145-166.

Asner G.P., & Heidebrecht, K.B. (2002). Spectral unmixing of vegetation, soil and dry carbon cover in arid regions: comparing multispectral and hyperspectral observations. *International Journal of Remote Sensing*, 23, 3939-3958.

Bateson A., and Curtiss, B. (1996). A method for manual endmember selection and spectral unmixing. *Remote Sensing of Environment,* 55, 229-243.

Bateson, C.A., Asner, G.P., & Wessman, C.A. (2000). Endmember bundles: A new approach to incorporating endmember variability into spectral mixture analysis. *IEEE Transactions on Geoscience and Remote Sensing*, 38, 1083-1094.

Berman, M., Kiiveri, H., Lagerstrom, R., Ernst, A., Dunne, R., & Huntington, J.F. (2004). ICE: A statistical approach to identifying endmembers in hyperspectral images. *IEEE Transactions on Geoscience and Remote Sensing*, 42, 2085-2095.

Bierwirth, P., Blewett, R., & Huston, D. (1999). Finding new mineral prospects with HYMAP: early results from a hyperspectral remote-sensing case study in the west Pilbara, *AGSO Research Newsletter*, 31, November.

Boardman, J.W. (1993). Automating spectral unmixing of AVIRIS data using convex geometry concepts. *Summaries of the fourth Annual JPL airborne Geoscience Workshop*, JPL Publication 93-26, 1, 11-14.

Bowles, J., Palmadesso, P.J., Antoniades, J.A., Baumback, M.M., & Rickard, L.J. (1995). Use of filter vectors in hyperspectral data analysis. *Proceedings SPIE Infrared Spaceborne Remote Sensing III*, 148-157.

Clark, R.N., Swayze, G.A., Gallagher, A.J., King, T.V.V., & Calvin, W.M. (1993). The U. S. Geological Survey, Digital Spectral Library: Version 1: 0.2 to 3.0 microns. *U.S. Geological Survey,* Open File Report 93-592.

Clark, R.N., Swayze, G.A., Livo, K.E., Kokaly, R.F., Sutley, S.J., Dalton, J.B., McDougal, R.R., & Gent, C.A. (2003). Imaging spectroscopy: Earth and planetary remote sensing with the USGS Tertracorder and expert systems. *Journal of Geophysical Research*, 108(E12), 5-1 to 5-44.

Cocks, T., Jensen, R., Stewart, A., Wilson, I., & Shields, T. (1998). The HYMAP^{TM} Airborne hyperspectral sensor: The system, calibration and performance. *Presented at 1st EARSEL Workshop in Imaging Spectroscopy*, October, Zurich, Switzerland.

Dennison, P.E., & Roberts, D.A. (2003). Endmember selection for multiple endmember spectral mixture analysis using endmember average RMSE. *Remote Sensing of Environment,* 87, 123-135.

Gillespie, A.R. (1992). Spectral mixture analysis of multispectral thermal infrared images. *Remote Sensing of Environment*, 42, 137-145.

Gross, H., *An image fusion algorithm for spatially enhancing spectral mixture maps* (1996). Unpublished doctoral dissertation, U.S. Air Force, Rochester Institute of Technology, New York.

Harsanyi J.C., & Chang, C-I., (1994). Hyperspectral image classification and dimensionality reduction: An orthogonal subspace projection approach. *IEEE Transactions on Geoscience and Remote Sensing*, 32, 779-785.

Haskell K. H., & Hanson, R. J. (1981). An algorithm for C linear least squares problems with equality and C nonnegativity constraints. *Mathematical Programming*, C 21, 98-118.

Heinz, D.C., & Chang, C-I. (2001). Fully constrained least squares linear spectral mixture analysis method for material quantification in hyperspectral imagery. *IEEE Transactions on Geoscience and Remote Sensing*, 39, 529-545.

Ifarraguerri, A., & Chang, C-I. (1999). Multispectral and hyperspectral image analysis with convex cones. *IEEE Transactions on Geoscience and Remote Sensing,* 37, 756-770.

Keshava, N., & Mustard, J.F. (2002). Spectral unmixing. *IEEE Signal Processing Magazine*, January, 44-57.

Kruse, F.A. (2002). Comparison of AVIRIS and Hyperion for hyperspectral mineral mapping. *Presented at the 11th JPL Airborne Geoscience Workshop*, 4-8 March, Pasadena, California.

Li, L., & Mustard, J. F. (2003). Highland contamination in lunar mare soils: Improved mapping with multiple end-member spectral mixture analysis (MESMA). *Journal of Geophysical Research*, 108(E6), 5053, 7-1 to 7-14.

Lu, D., Batistella, M., Moran, E., & Mausel, P. (2004). Application of spectral mixture analysis to Amazonian land-use and land cover classification. *International Journal of Remote Sensing,* 25, 5345-5358.

Nascimento, J.M.P., & Dias, J.M.B. (2005). Vertex component analysis: a fast algorithm to unmix hyperspectral data. *IEEE Transactions on Geoscience and Remote Sensing*, 43, 898-910.

Neville, R.A., Staenz, K., Szeredi, T., Lefebvre, J., & Hauff, P. (1999). Automatic Endmember Extraction from Hyperspectral Data for Mineral Exploration. *Fourth International Airborne Remote Sensing Conference and Exhibition / 21st Canadian Symposium on Remote Sensing*, Ottawa, Ontario, Canada, 21-24 June.

Neville, R.A., Levesque, J., Staenz, K., Nadeau, P., Hauff, P., & Borstad, G.A. (2003). Spectral unmixing of hyperspectral imagery for mineral exploration: comparison of results from SFSI and AVIRIS. *Canadian Journal of Remote Sensing*, 29, 99-110.

Okin, W.J., Okin, G.S., Roberts, D.A., & Murray, B. (1999). Multiple endmember spectral mixture analysis: endmember choice in an arid shrubland. In: R.O. Green (ed.) *1999 AVIRIS Workshop*, JPL, Pasadena, California, 323-332.

Okin, G.S., Roberts, D.A., Murray, B., & Okin, W.J. (2001). Practical limits on hyperspectral vegetation discrimination in arid and semiarid environments. *Remote Sensing of Environment,* 77, 212-225.

Painter, T.H., Dozier, J., Roberts, D.A., Davis, R.E., & Green, R.O. (2003). Retrieval of subpixel snow-covered area and grain size from imaging spectrometer data. *Remote Sensing of Environment,* 85, 64-77.

Petrou, M., & Foschi, P.G. (1999). Confidence in linear spectral unmixing of single pixels. *IEEE Transactions on Geoscience and Remote Sensing*, vol. 37, no. 1, pp. 624-626.

Plaza, A., Martinez, P., Perez, R., & Plaza, J. (2002). Spatial/spectral endmember extraction by multidimensional morphological operations", *IEEE Transactions on Geoscience and Remote Sensing*, 40, 2025-2041.

Ramsey M.S., & Christensen, P.R. (1998). Mineral abundance determination: Quantitative deconvolution of thermal emission spectra. *Journal of Geophysical Research,* 103, 577-596.

Roberts, D.A., Gardner, M., Church, R., Ustin, S., Scheer, G., & Green, R.O. (1998). Mapping chaparral in the Santa Monica Mountains using multiple endmember spectral mixture models. *Remote Sensing of Environ*ment, 65, 267-279.

Roberts, D.A., Dennison, P.E., Gardner, M., Hetzel, Y.L., Ustin, S.L., & Lee, C. (2003). Evaluation of the potential of Hypersion for fire danger assessment by comparison to the airborne visible infrared spectrometer. *IEEE Transactions on Geoscience and Remote Sensing*, 14, 1297-1310.

Roessner, S., Segl, K., Heiden, U., & Kaufmann, H. (2001). Automated differentiation of urban surfaces based on airborne hypersepctral imagery. *IEEE Transactions on Geoscience and Remote Sensing*, 39, 1525-1532.

Sabol, D.E., Adams, J.B., & Smith, M.O. (1992). Quantitative sub-pixel spectral detection of targets in multispectral images. *Journal of Geophysical Research*, 97, 2659-2672.

Sabol Jr., D. E., Gillespie, A. R., Adams, J.B., Smith, M.O., & Tucker, C.J. (2002). Structural stage Pacific Northwest forests estimated using simple mixing models of multispectral images. *Remote Sensing of Environ*ment, 80, 2002.

Settle, J.J., & Drake, N.A. (1993). Linear mixing and the estimation of ground cover proportions. *Inernational Journal of Remote Sensing*, 14, 1159-1177.

Settle, J.J., (1996). On the relationship between spectral unmixing and subspace projection. *IEEE Transactions on Geoscience and Remote Sensing*, 34, 1045-1046.

Small, C. (2001). Estimation of urban vegetation abundance by spectral mixture analysis. *International Journal of Remote Sensing*, 22, 1305-1334.

Staenz, K., Szeredi, T., & Schwarz, J. (1998). ISDAS - A System for Processing/Analyzing Hyperspectral Data; Technical Note. *Canadian Journal of Remote Sensing*, 24, 99-113.

Winter, M.E. (1999) Fast autonomous spectral endmember determination in hyperspectral data. *Proceedings of the Thirteenth International Conference on Applied Geologic Remote Sensing*, Vancouver, B.C., Canada, II, 337-344.

CHAPTER 4
APPLICATION OF HYPERSPECTRAL DATA FOR REMOTE PREDICTIVE MAPPING, BAFFIN ISLAND, CANADA[3]

4.1 Introduction

Regional geological mapping in the Arctic is time intensive and costly, primarily owing to poor accessibility, but is essential for subsequent geological investigations and mineral exploration. Extensive budget cuts in geological surveys have resulted in the necessity to pursue effective reconnaissance mapping methods. Air photos and airborne magnetic data (if available) are used to locate bedrock exposure and map structural trends related to the geology. These data sets are essential tools to assist the field geologist in producing accurate geological maps. Visible and near-infrared reflectance multi- and hyperspectral data have also been used to support geological mapping (e.g. Podwysocki et al., 1983; Smith et al., 1985; Sultan et al., 1987; Griffiths et al., 1987; Kaufmann, 1988; Loughlin, 1991; Crowley, 1993; Rowan et al., 1995; Sabins, 1999; Yang et al., 1999; Bierwirth et al., 2002; Clark et al., 2003; Rowan et al., 2004; and Harris et al., 2005). Unlike multispectral sensors, such as Landsat TM, hyperspectral sensors collect data over hundreds of contiguous channels with spectral resolution on the order of 10 - 20 nm. This allows the identification of specific absorption features associated with common rock-forming and alteration minerals (e.g. Hunt, 1977; Clark et al., 1990; Vitorello and Galvao, 1996). In arid regions such as Cuprite, Nevada, the lack of vegetation allows for detailed spatial mapping of mineral outcroppings and the dispersion of those minerals in alluvial fans (e.g. Clark et al., 2003).

Bedrock mapping using hyperspectral data presents different challenges compared with target detection, which focuses on searching the image for specific spectral features related to minerals of interest. For example, target detection is particularly useful for locating specific minerals with diagnostic absorption features occurring within alteration zones (e.g. Yang et al., 1999; Bierwirth et al., 2002; Clark et al., 2003). For bedrock mapping, the pixel spectra are compared to the reflectance of the mineral assemblages that make up individual rock units (e.g. Rowan et al., 2004; Harris et al., 2005). Units are mapped based on spatial continuity of surface composition, rather than occurrence of individual minerals. Bierwirth et al. (2002) showed that hyperspectral data could be used to effectively map mineral assemblages associated with gold mineralization in poorly exposed terrain in the Central Pilbara, as long as the surface material was dominantly in-situ soil and residual rock. In a study by Rowan et al. (2004) vegetation comprised about 50 percent of the area complicating identification, but also allowed for mapping of bedrock units based on subtle differences in spectral shape owing to variations in vegetation cover. A similar relationship was observed by Harris et al. (2005) in an analysis of hyperspectral data in the Canadian Arctic, where vegetation was used as a proxy for gabbroic units in specific localities.

The objective of this study is to demonstrate the application of airborne hyperspectral data for the generation of accurate remote predictive lithological maps in the Arctic setting. These maps can be used to: 1) assist regional mapping by giving detailed spatial and spectral information; 2) focus future mapping projects; or, 3) highlight areas of economic potential. The study area is located in southern Baffin Island, about 80 km south of Iqaluit, and is part of a larger hyperspectral survey undertaken by the Geological Survey of Canada to assess this technology for regional mapping in the Canadian Arctic. This particular area comprises a diverse assemblage of lithologies and is characterized by excellent bedrock exposure and in-situ boulder fields and regolith. From an economic stand point the region includes mafic and ultramafic rocks that are contemporaneous with rocks in Raglan, Quebec, and Thompson, Manitoba that host Cu-Ni and PGE mineralization, all of which are part of the larger Trans-Hudson Orogen (Dillon-Leitch et al., 1986; Lewry and Stauffer, 1990; St-Onge and Lucas, 1994). The carbonate rocks in the region are also known to contain gem-quality minerals in some localities.

---

[3] Portions of this chapter have been published. Rogge, D., Rivard, B., Zhang, J. & Harris, J. (2005). Remote predictive geological mapping using airborne hyperspectral data, Baffin Island. *Annual Meeting of Geological Association of Canada.* Halifax, Nova Scotia, May 15-18.

Harris et al (2005) applied a minimum noise fraction transform and matched filtering to map lithology for a portion of the data set used in this study. This study expands on the work by Harris et al. (2005) to: 1) obtain a more complete representation of the lithological units present in the study area, specifically those that have economic potential (e.g. mafic-ultramafic rocks and carbonates); 2), generate a predictive lithological map that is similar in format to recent regional lithological maps; and 3) consider the impact of rock encrusting lichen for mapping.

4.2 Study Area

The study area (Figure 4.1) is part of the northeastern segment of the Paleoproterozoic Trans-Hudson Orogen (Lewry and Stauffer, 1990), which comprises tectonostratigraphic assemblages accreted to the northern margin of the Archean Superior Province. The tectonostratigraphic assemblages in southern Baffin Island are characterized by stacked tectonic elements comprising the lower Superior Province and Povungnituk Group, the Narsajuaq arc (1.83 Ga), and the upper Lake Harbour Group, Ramsay River orthogneiss, and Blanford Bay assemblage. The upper group is intruded by the Cumberland batholith (1.86 Ga) (St-Onge et al., 1999; St-Onge et al., 2002). The study area lies within the Lake Harbour Group and comprises upper amphibolite to granulite grade metamorphosed granodiorite, monzonite, tonalite, syenite, peridotite, gabbro, carbonate, and clastic sedimentary units (Figure 4.1). The mafic and ultramafic rocks within the Lake Harbour Group are considered sills, and are 10 – 100's of meters thick and trend several kilometers along strike. These rocks have a potential for magmatic Cu-Ni sulfide mineralization. Trace disseminated graphite, pyrite and chalcopyrite characterize the weathered rusty garnetiferous psammite, pelite and semi-pelite rocks of the Lake Harbour Group. Calcareous rocks trend 5 to 25 km along strike, and are commonly interlayered with siliciclastic rocks. Within the metasedimentary rocks orthoquartzite occurs as discrete layers and garnet-rich monzogranite outcrops as tabular bodies 100's of meters thick. The intruding Cumberland batholith is dominated by pink weathered orthopyroxene-biotite monzogranite that is massive to weakly foliated (St-Onge et al., 1999). Vegetation cover is limited (~25%), comprising primarily moss and grass, with dwarf shrub willows. Rock encrusting lichens covering a few percent to almost 100 percent of the rock are common to the majority of rock units. The region also includes numerous small lakes and year-round snow cover in gullies and shaded areas.

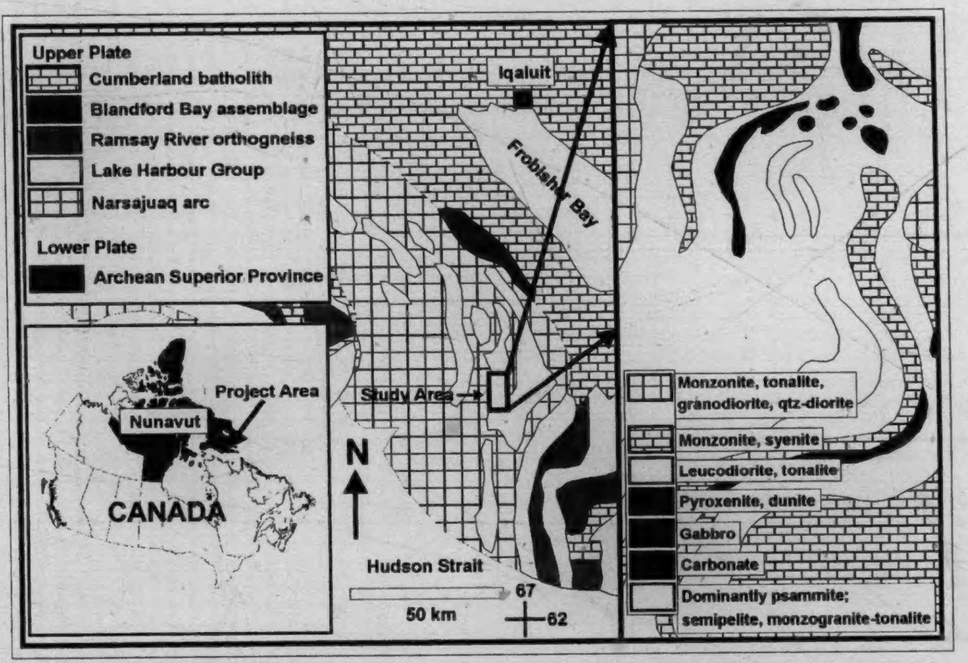
Upper Plate
Cumberland batholith
Blandford Bay assemblage
Ramsay River orthogneiss
Lake Harbour Group
Narsajuaq arc
Lower Plate
Archean Superior Province
Project Area
Nunavut
CANADA
Iqaluit
Frobisher Bay
Study Area
N
Hudson Strait
50 km
67
62
Monzonite, tonalite, granodiorite, qtz-diorite
Monzonite, syenite
Leucodiorite, tonalite
Pyroxenite, dunite
Gabbro
Carbonate
Dominantly psammite; semipelite, monzogranite-tonalite

Figure 4.1 Regional geology of south-western Baffin Island and zoom of local geology of the study area (1:100 000) (modified from St-Onge et al., 1999).

4.3 Hyperspectral Data Set

Airborne hyperspectral data (~3.5 x 7 km) were acquired with the Probe I sensor, which comprises 128 channels from 446 - 2543 nm with an average spectral resolution of ~15 nm and a spatial resolution of ~7 m (Figure 4.2). The spectral range of the Probe sensor allows for the discrimination of spectral features associated with transition elements (e.g. Fe^{2+}, Fe^{3+}, Ni, Cr, Co) and H_2O, CO_3, OH, Al-OH, Fe-OH, and Mg-OH vibrational absorption features (Hunt, 1977; Clark et al., 1990). A vicarious atmospheric correction of the data was performed by the Canadian Centre for Remote Sensing using field spectra acquired at the Iqaluit airport concurrently with the overflight. A number of the 128 channels available were not used (874-991, 1082-1171, 1271-1537, 1755-2073, and 2465-2543 nm) for this analysis owing to atmospheric water-absorption and excessive noise. No additional preprocessing (e.g. smoothing filter) was applied to the remaining 86 bands.

Field sampling and collection of spectra took place along traverses oriented perpendicular to the dominant structural and stratigraphic trends (Figure 4.2). The spectra were acquired with a portable ASD® field spectrometer that has 2151 bands covering the 350 – 2500 nm spectral range. A total of 217 spectral measurements were acquired for 56 of 188 sites visited, some of which lie outside, but proximal to the study area, and are representative of the geology shown in Figure 4.2. Multiple measurements were taken at each site for fresh, weathered, polished, and partial to fully lichen coated surfaces. Thin section, X-ray diffraction (XRD) and major- and trace-element geochemical analysis were performed on 24 rock samples that were considered to be representative of the regional geology.

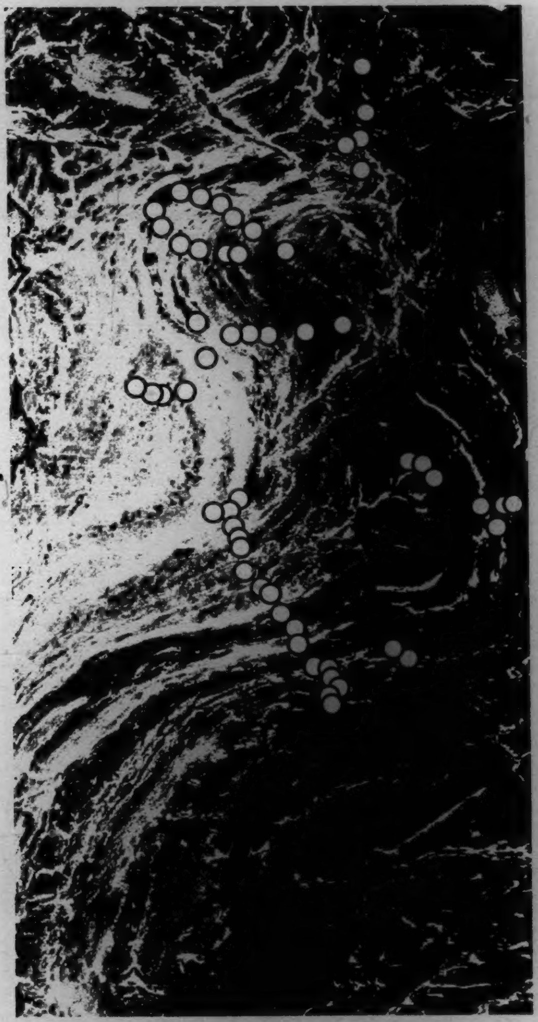

Figure 4.2 Probe I hyperspectral data of the study area. Circles represent ground locations for field spectra and sample collection.

4.4 Generating a Remote Predictive lithological Map

Two steps were required to generate the remote predictive lithological map from the Probe I hyperspectral image: 1) the extraction of image endmembers and the application of spectral mixture analysis (SMA) to generate fractional abundance maps (Step A); and, 2) converting the fractional abundance maps into predictive lithological maps (Step B). Figure 4.3 is a flow chart of the various steps involved in each of the two main parts.

4.4.1 Spectral mixture analysis

The spectrum of each image pixel is the combined reflectance of each of the surface components within the sensors field of view. The consequence of spectral mixing is that few image pixels display "pure" spectra (Settle and Drake, 1993), which makes identification and classification difficult. SMA was designed to address the problems associated with mixed pixels by deconvolving each pixel spectrum into fractional abundances of its surface components, or end member spectra (Adams et al., 1986; Adams et al., 1993). To produce accurate predictive lithologic maps we aim to locate pixels that contain rock, even in the presence of other materials (e.g. snow, vegetation). Examples of SMA for geological mapping can be found in studies by Mustard and Pieters (1987), Kruse et al. (1990), Zamudio and Atkinson (1990), Blount et al. (1990), Murphy (1995), Bierwirth et al. (1999), Asner and Heidebrecht (2002), and Neville et al. (2003).

For SMA the extraction of spectral endmembers from an image is commonly preferred over the use of field or laboratory spectra for two main reasons: 1) library and field spectra may not represent all relevant endmember spectra of the surface components, or are inadequate representations; and, 2) image endmembers have the advantage of directly sampling surfaces in the scene. Image endmembers are assumed to be "pure", or relatively "pure" spectra, meaning that little or no mixing with other endmembers has occurred within a given pixel and for this assumption to be met, a careful selection of endmembers is required.

Linear spectral mixture analysis is based on the premise that a given mixture can be modeled using a set of linearly independent endmember spectra. Applying linear SMA to a given mixture requires that endmembers occur as spatially segregated patterns (Keshava and Mustard, 2002), with multiple scattering involving several endmembers (non-linear mixing) being negligible. To deconvolve a spectrum into abundances of its constituent endmember spectra the following equation can be solved using a least squares approach,

$$R_b = \sum_{i=1}^{n} F_i S_{ib} + E_b \qquad (1)$$

where R_b is the reflectance of the pixel at band b, F_i is the fractional abundance of the endmember i, S_{ib} describes the reflectance of endmember i at band b, n equals the number of endmembers, and E_b is the error of the fit at band b. Equation 1 can produce endmember fractional abundances that are negative, which are mathematically correct, but physically unrealistic. Thus, equation 1 can be solved so that: 1) fractional abundances sum-to-one (ASC); and, 2) fractional abundances are non-negative (ANC). Simultaneous implementation of ASC and ANC (e.g. constrained unmixing) is usually recommended in order to produce fractional abundances that are physically realistic (Heinz and Chang, 2001). However, abundances predicted using linear SMA are most accurate when only the endmembers that comprise a given pixel are used, with larger abundance errors occurring when either too few or too many endmembers are used (Sabol et al., 1992; Heinz and Chang, 2001). In this paper we made use of the iterative spectral mixture analysis (ISMA) of Rogge et al. (2006), which is designed to unmix each pixel using an optimal per-pixel endmember set. The result is a fractional abundance map for each endmember, which can subsequently be used to generate a remote predictive geological map.

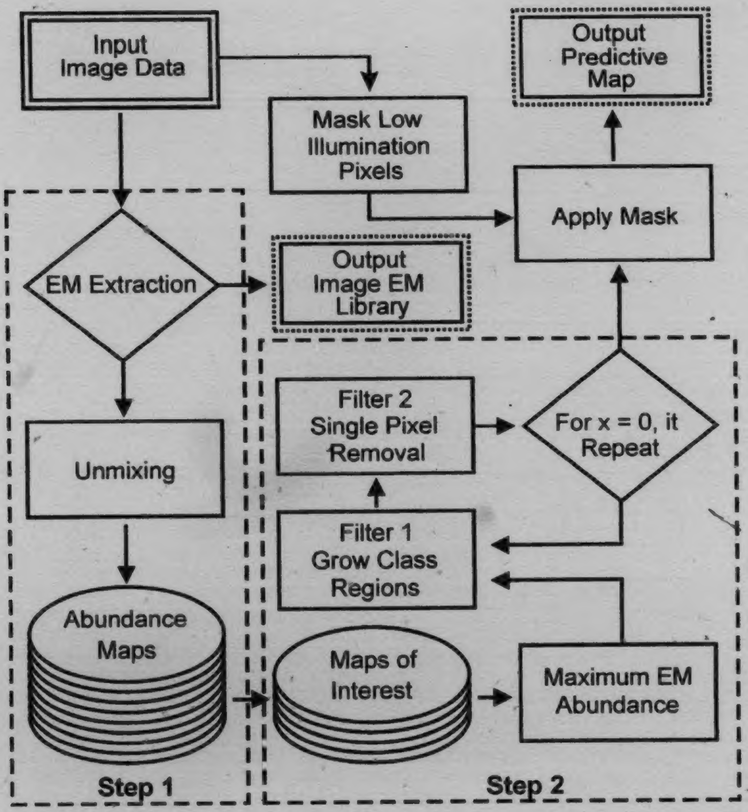
Input
Image Data
Mask Low
Illumination
Pixels
Output
Predictive
Map
Apply Mask
EM Extraction
Output
Image EM
Library
Filter 2
Single Pixel
Removal
For x = 0, it
Repeat
Unmixing
Filter 1
Grow Class
Regions
Abundance
Maps
Maps of
Interest
Maximum EM
Abundance
Step 1
Step 2

Figure 4.3 Schematic representation of processing steps involved in generating fractional abundance maps using SMA (Step 1), and subsequent steps to generate a predictive geological map (Step 2).

4.4.2 Endmember extraction

For the extraction of image endmembers we examined the results from four image endmember extraction tools. The first two methods, iterative error analysis (IEA) (Neville et al., 1999) and SMACC, are available in the Imaging Spectrometer Data Analysis System (ISDAS) (Staenz et al., 1998) and ENVI^{TM} software packages, respectively. The other two methods, spatial-spectral endmember extraction (SSEE) (Rogge et al., 2006) and sequential projection algorithm (SPA) (J. Zhang, unpublished, 2005) have been developed at the Earth Observation Systems Laboratory, University of Alberta.

Multiple tools were used as each may result in slightly different endmember sets, specifically with respect to endmembers that are defined by more subtle absorption features. Image endmembers derived from the endmember extraction tools were combined into a single endmember set. The image endmembers were subsequently labeled based on the analysis of spectral features and comparison with field and laboratory spectra. A comparison of geological image endmembers with field and laboratory spectra was also used to test how well the endmember spectra, acquired at ~ 7 m spatial resolution, represent field and laboratory spectra (of field samples) acquired at ~ 25 cm and ~ 2 cm spatial resolution, respectively. Spectral similarity was determined visually and by measuring the spectral angle (Kruse et al., 1993) between the two spectra of interest.

4.4.3 Predictive map generation

Pixels in the original hyperspectral image that comprise <10% average reflectance were masked, as these low illumination pixels comprise limited spectral information causing errors in fractional abundance and should not be retained in the predictive map. The masked regions also included water, which has low overall reflectance and can easily be distinguished from other surface components. Snow was also masked as it has diagnostic high reflectance in the visible and occurs as spatially well-defined regions.

Combining the information from the fractional maps into a single map that is similar to traditional geological maps is a more practical approach for predictive mapping. A preliminary predictive map was generated by determining the endmember with the maximum fractional abundance for each pixel and assigning that pixel to the given endmember class. In order for a pixel to be assigned to a given endmember, the endmember must have a minimum fractional abundance (confidence level) otherwise the pixel was assigned a null class. The minimum fractional abundance set for this study was 0.5. The preliminary map was then filtered to grow the assigned class regions into null class regions. This was done to extrapolate between clusters of pixels of the same class where non-geological classes dominate (e.g. snow, vegetation); and, to allow spatially limited geological pixel clusters to be viewed in the final predictive map. For each null class pixel the adjacent area (nxn window) is searched for the dominant endmember class. This endmember class must have a minimum of m pixels within the window region in order for the null class pixel to be assigned to that class. A second filter is then applied to remove single pixels of any given class that are not spatially associated (nxn window) with a minimum number (m) of nearby pixels of the same class. Both filters can be applied iteratively to fill more of the null class space. However, the number of growing iterations should be kept to a minimum, as the emerging map patterns will not necessarily conform to the natural trend of the rock units. The result is a predictive lithological map that is similar to a traditional geological map, but that contains regions that are not labeled (null class regions). For filter 1 and 2 a window size of n = 5 was used, with a minimum number of similar endmember class pixels (m) within the window set to 5. The number of iterations (it) for growing and removing single pixels was set to 3.

4.5 Results

4.5.1 Image endmember set and spectral identification

The final image endmember set comprises twenty endmembers, including three snow/ice, one water, three vegetation, one rock encrusting lichen, and twelve geological endmember spectra. The three snow/ice endmembers (Figure 4.4) are interpreted to represent different stages of melting of the snow on land and ice. The vegetation endmembers represent the limited vegetation cover in the study area, which comprises wet/dry grass, moss, and dwarf shrub willows.

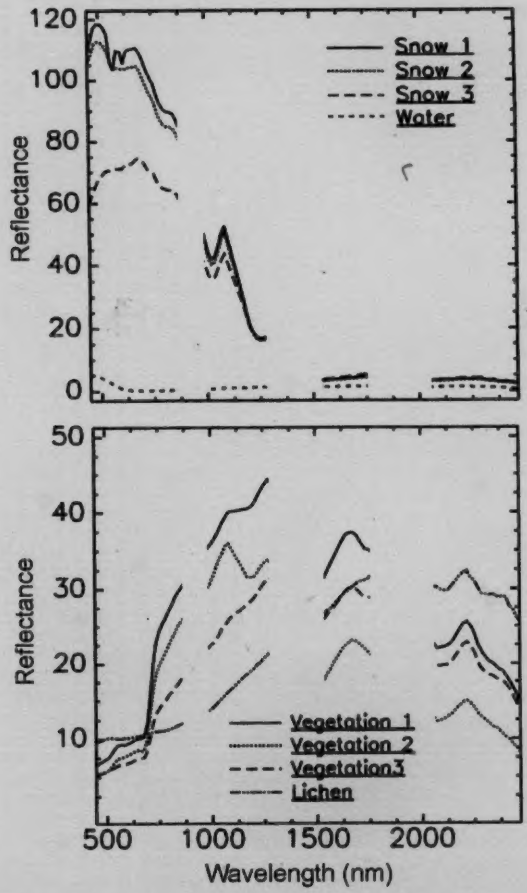

Figure 4.4 Reflectance spectra of snow, water, vegetation, and lichen endmembers. Blank areas represent bands excluded owing to noise or water absorption features.

The twelve geological endmembers can be grouped into: 1) peridotites, 2) iron oxide/hydroxide weathering, 3) clastic metasediments, 4) carbonate rocks, 5) lichen-rock mixtures, and 6) varnish; based on spectral features (e.g. Fe^{2+}, Fe^{3+}, Fe-OH, Mg-OH, Al-OH, CO_3) and comparisons with field and laboratory spectra (Figure 4.5). Spectral measurements in the field were limited for some regions of the study area. Thus, some image endmembers do not include comparable field and laboratory spectra.

Two peridotite endmember spectra were found, but collection of samples and field spectra was limited to localities subsequently mapped as peridotite 1. Both peridotite endmembers show a broad ferrous-iron absorption feature at ~1006 nm that is consistent with an iron absorption feature observed in spectra of clino-pyroxene and amphiboles (Clark et al., 1993). These two minerals are observed in the thin sections of samples (Table 4.1) whose spectra match well with the endmember spectra (Figure 4.5). Peridotite 1 differs from peridotite 2 with the occurrence of two diagnostic absorption features at ~2320 and 2400 nm that can be attributed to Fe,Mg-OH vibrational features. These features may result from alteration of pyroxene to an amphibole (King and Clark, 1989), a common mineral of metamorphosed ultramafic rocks occurring up to lower granulite facies. Alternatively serpentinization of olivine may also be associated with the 2320 nm feature (King and Clark, 1989; Hunt and Evarts, 1981). Samples of peridotite 1 show hornblende and serpentine in XRD and thin section. Similar ferrous-iron and Fe, Mg-OH features were observed in spectra of peridotites of the Morden ultramafic complex, Australia (Rowan et al., 2004). The absence of such features in the peridotite 2 endmember may be attributed to limited alteration of pyroxene to hornblende. However, it is also possible that the two endmembers represent distinct primary mineral assemblages and thus, two distinct ultramafic units.

The iron oxide/hydroxide endmember displays iron absorption features at ~650 and 900 nm, consistent with the minerals hematite and goethite (Clark et al., 1993). These minerals are commonly a product of surface weathering of pyrite and magnetite, which are observed in thin section of samples with best corresponding spectra (Figure 4.5). Iron absorption features are also seen in the metased 3 endmember, and to a lesser extent in the two other metasedimentary endmembers. The metased 2 and the metased 3 endmembers show an absorption feature at ~2215 nm commonly attributed to an Al-OH absorption feature associated with the presence of Fe-muscovite (Duke, 1994). However, muscovite is absent in samples collected and thin sections are rich in feldspar. Thus, the feature at ~2215 nm may result from weathering of feldspars producing minerals such as kaolinite and sericite. Kaolinite has a doublet absorption feature at ~2165 nm and ~2200 nm seen in the metased 2 endmember. This feature is not well defined in metased 3.

Interlayered with clastic metasediments is the unit labelled c.g. quartzite/granite, which forms one spectral endmember. There are no diagnostic spectral features associated with this endmember, except for a weak absorption feature at ~2215 nm. Based on the mineralogy observed in thin section this feature is likely associated with the alteration of feldspar.

Both carbonate image endmember spectra are observed in the spectra acquired in the field for individual site locations (Figure 4.5), suggesting variability in the mineralogy at the scale of ~10x10 m. The two carbonate endmembers display absorption features at 2145 and ~2330 nm, which are consistent with CO_3 vibrational absorption features present in carbonate rocks. The narrow absorption feature at ~2330 nm is slightly shifted from 2319 to 2336 nm for carbonate 1 and 2, respectively. Such a shift in carbonate rocks has been attributed to the presence of dolomite (~2320 nm) and calcite (~2335 nm) (Crowley, 1986). Analysis of the thin section data and XRD results show that only remnant calcite and/or dolomite is present, with the samples consisting predominantly of diopside and phlogopite, both of which occur in metamorphosed carbonate rocks at amphibolite grade. Phlogopite has narrow absorption features at ~2250, 2325 and 2380 nm, whereas diopside shows a broad iron related feature at ~1050 nm and 2 narrow features at ~2315 and 2386 nm (Clark et al., 1993). The broad feature at ~1050 nm of diopside can be correlated with a broad feature at 1036 nm observed in carbonate 2. In the short-wave infrared features observed in carbonate 2 at ~2251 and 2336 nm can be attributed to phlogopite, with diopside likely also impacting the ~2336 nm feature. The weak feature at ~2380 nm characteristic of phlogopite and diopside is not well defined in our endmember spectra. However, the spectral resolution of the Probe sensor may limit our ability to detect this feature.

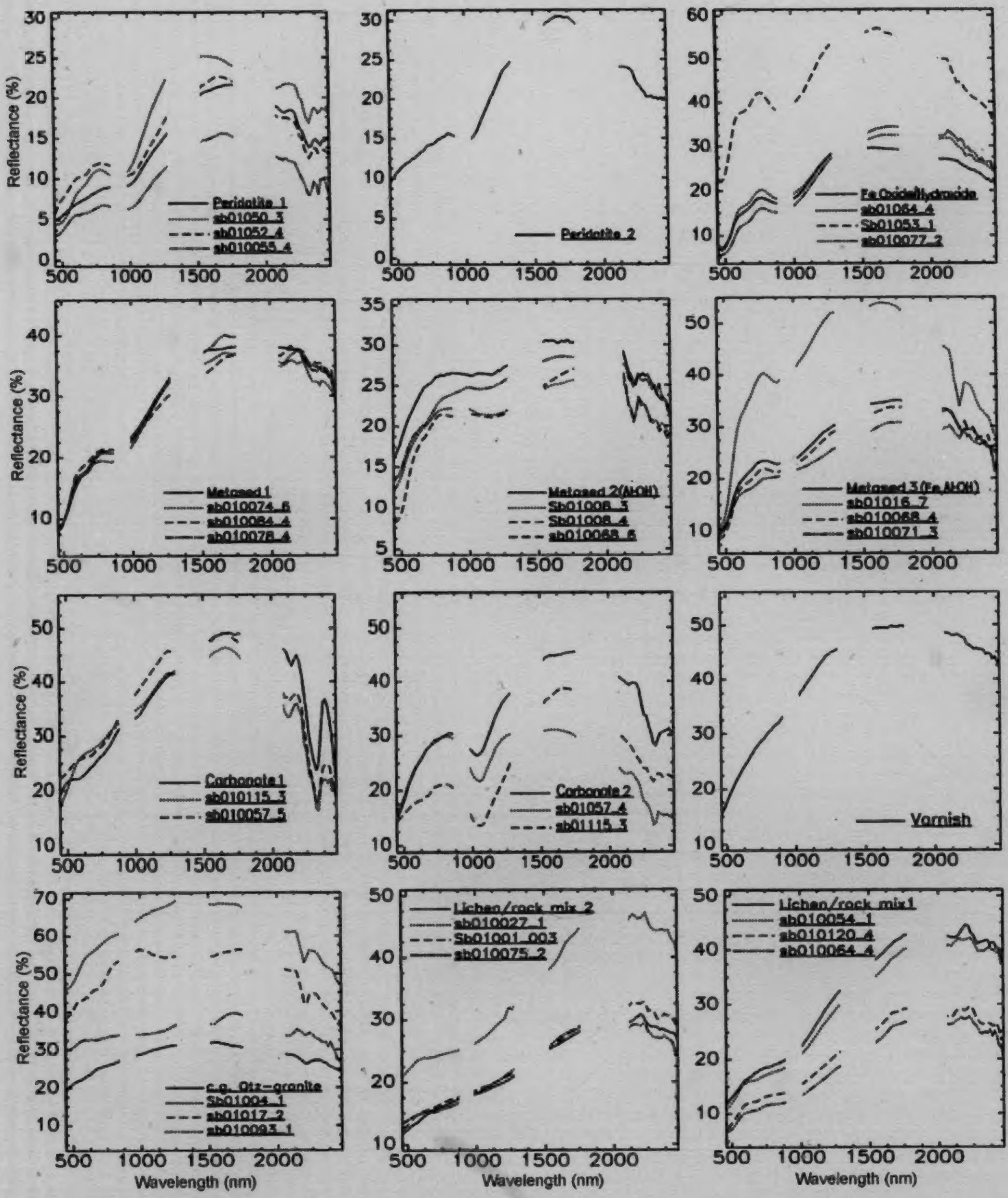

Figure 4.5 Geological image endmember spectra (solid line in each graph) and best corresponding sample field/laboratory spectra. Refer to Table 1 for details about sample spectra. Blank areas represent bands excluded owing to noise or water absorption features.

Table 4.1 Details of image endmembers with best corresponding field and laboratory spectra.

Endmember	Spectrum (1)	Sample details	Rock type	Mineraloigy based on thin section and XRD analysis
Peridotite 1	L sb01050_3	weathered, rusted	altered peridotite	55% hbl (after cpx,opx), 40% srp (after ol), 5% srp/goe
	L sb01052_4	weathered, mild rust < 10% lichen	altered peridotite	60% hbl (after cpx,opx), 35% srp (after ol), tr. spl, py, hem
	F sb010055_4	broken	mafic intrusion	40% hbl (after cpx,opx), 5% cpx/opx, 40% srp (after ol), 5% spl, tr. mag, py
Peridotite 2		No sample available		
Oxide/hydroxide weathering	L sb01064_7	broken, well rusted	Seriate metagranite	7% bt, 7% grt, tr. py, mag, 15% crd, 20% plag, 25% kspar, 25% qtz
	L sb01053_1	cut	granulite gneiss	3% bt, tr. grt, py, 8% crd, 3%plag, 15% kspar, 60% qtz
	F sb010077_2	rusted	clastic metasediment	
Metased 1	F sb010074_6	insitu rubble < 20 cm, rusted	garnet granulite gneiss	10% grt, 10% bt, 5% crd, 20% plag, 20% kspar, 30% qtz
	F sb010084_4	broken, rusty, sandstone	clastic metasediment	
	F sb010078_4	10% lichen	clastic metasediment	
Metased 2 (Al-OH)	L sb01008_3	weathered < 10% lichen	garnet granulite gneiss	7% bt, 10% grt, tr. py, 5% sil, 10% plag, 30% kspar, 30% qtz
	L sb01008_4	broken, < 10% lichen	garnet granulite gneiss	7% bt, 10% grt, tr. py, 5% sil, 10% plag, 30% kspar, 30% qtz
	F sb010068_6	banded, insitu fine material, rusted	clastic metasediment	
Metased 3 (Fe,Al-OH)	L sb01016_7	broken, rusted	clastic metasediment	
	F sb010068_4	banded, rusted zone	clastic metasediment	
	F sb010071_3	rusted zone, < 10% lichen	clastic metasediment	
c.g. Quartzite /granite	L sb01004_1	cut, c.g. < 5% grt	granular granite	1% bt, 3% grt, 20% plag, 60% kspar, 15% qtz
	L sb01017_2	cut, c.g. 1-2% grt	qtz-rich granular granite	1% bt, 3% grt, 20% plag, 20% kspar, 50% qtz
	F sb010093_1	glacial polish	qtz-monzonite/quartzite	
Carbonate 1	L sb010057_5	weathered	Calc-silicate	10-15% phl, 0-20 plag (50% ser), 60% di, tr. scp
	L sb010115_3	weathered	Calc-silicate	>95% di, tr. scp, cal remnants
Carbonate 2	L sb01057_4	weathered	Calc-silicate	10-15% phl, 0-20 plag (50% ser), 60% di, tr. scp
	F sb01115_3	weathered < 10% lichen	Calc-silicate	>95% di, tr. scp, cal remnants
Lichen-rock mixture 1	F sb010054_1	minor lichen	granite (mafic lenses)	10% plag, 40% kspar, 35% c.g. qtz (mafic lenses 5%hbl and cpx)
	F sb010064_4	insitu c.g. rubble	seriate metagranite	7% bt, 7% grt, tr. py, mag, 20% plag, 25% kspar, 25% qtz
	F sb010120_4	insitu c.g. rubble	clastic metasediment	
Lichen-rock mixture 2	L sb01001_3	weathered, 10-20% lichen	garnet granulite gneiss	5% bt, 5% grt, tr. py, 2% crd, 1% sil, 25% plag, 30% kspar, 30% qtz
	F sb010027_1	minor lichen	quartz monzonite	
	F sb010075_2	glacial polish	clastic metasediment	

(1) L – lab spectra, F – field spectra; the file name relates to sample#_spectrum#

Minerals: hbl-hornblende;cpx-clinopyroxene;opx-orthopyroxene;srp-serpentine;ol-olivine;goe-goethite;spl-spinel;py-pyrite;hem-hematite;mag-magnetite;bt-biotite;grt-garnet;crd-corderite;plag-plagioclase;kspar-potassium feldspar;qtz-quartz;sil-sillimanite;phl-phlogopite;di-diopside;scp-scapolite;cal-calcite

The next group of endmembers include two spectra interpreted as lichen-rock mixtures (Figure 4.5). These two endmembers show absorption features visible at 1730 and 2100 nm also seen in the lichen endmember (Figure 4.6) and documented in spectra of foliose and crustose lichens (Bechtel et al., 2002; Rees et al., 2004). The two endmember spectra also show increased reflectance in the visible, which is likely attributed to a rock component. Lichen-rock mixture 1 displays a greater increase in reflectance between ~1000 – 1270 nm, higher reflectance in the short wave infrared, and two subtle absorption features at ~2286 and 2369 nm.

The last geological endmember is not represented by the field and laboratory spectra, and does not show diagnostic spectral features. This endmember has been tentatively labeled as varnish, or a surficial geological component, owing to its spatial distribution (see next section).

4.5.2 Fractional abundance and maps

Figure 4.7 show the abundance maps for the three vegetation endmembers and the lichen endmember. Vegetation 1 and 2 show limited spatial extent, whereas vegetation 3 is widely distributed and conforms to lithologic trends visible in the original hyperspectral image (Figure 4.2). This characteristic is also observed for the distribution of lichen (Figure 4.7D), which follows predominantly the quartzofeldspathic units of the existing 1:100 000 geological map (Figure 4.1). However, the distribution of these endmembers cannot be used as a proxy for mapping specific units as each cross multiple lithological units, and in turn, are not included in the generation of the predictive maps.

Fractional abundance maps for the geological endmembers are shown in Figure 4.8. The peridotite and carbonate endmember maps show occurrences with limited spatial extent (Figure 4.8 A,B,I,J) and relatively uniform abundances. Although the two carbonate endmember spectra appear to occur locally at the scale of site locations, spatial mapping of these endmembers show that they dominate spatially distinct carbonate outcrops in the study area. The distribution of the iron oxide/hydroxide weathering unit is also limited (Figure 4.8C), but shows more variable abundances. The remaining geological endmembers are spatially extensive and show a range of abundances, indicating variable sub-pixel mixing with other rock units, and/or vegetation and lichen. The varnish endmember (Figure 4.8D) display low abundances distributed throughout the study area, excluding areas occupied by vegetation.

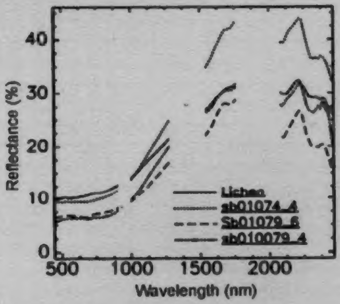

Figure 4.6 Lichen image endmember spectra (solid line) and best corresponding sample field/laboratory spectra. Blank areas represent bands excluded owing to noise or water absorption features.

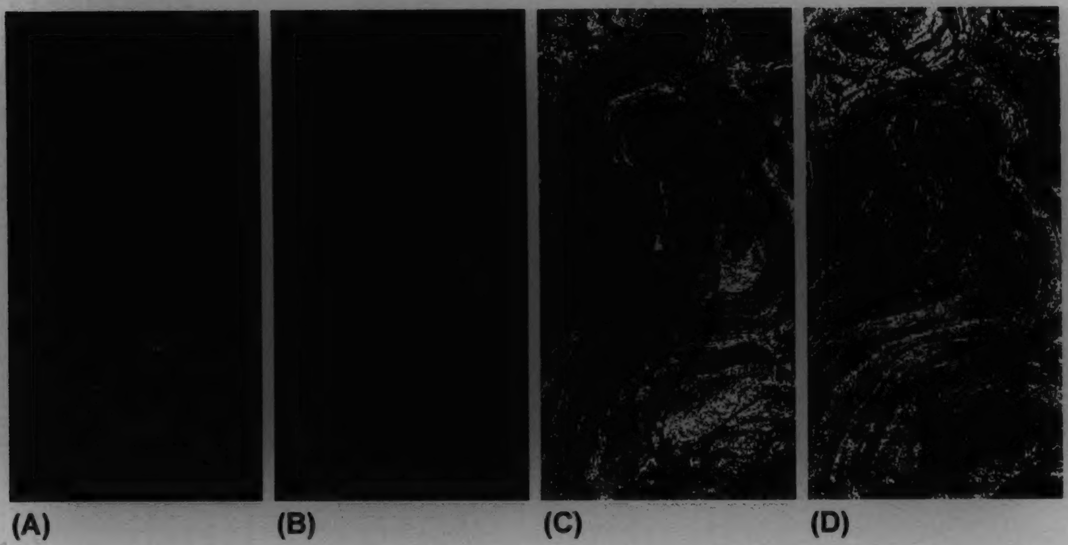

Figure 4.7 Fractional abundance maps for vegetation 1 (A), vegetation 2 (B), vegetation 3 (C), and lichen (D) endmembers. Black – low abundance; white – high abundance. Images are linearly scaled to best show abundance variation and spatial distribution.

4.5.3 Predictive geological maps

Predictive geological maps (Figure 4.9) were generated using 11 of the geological endmember fractional abundance maps. The varnish endmember is interpreted to be a surficial material and thus was excluded from the bedrock geology compilation. The existing published map (Figure 4.9C) comprises seven units. Comparison with the predictive map (Figure 4.9D) shows good overall correlation, excluding unit 1 (monzonite, tonalite, granodiorite, quartz diorite) and 4 (gabbro, amphibolite), which do not have equivalent image endmembers.

Lichen rock mixture 1 shows good spatial correlation with the curvilinear regions of unit 2 (monzonite-syenite) shown in Figure 9C. However, the larger regions of unit 2 in the top-left and bottom-right corners are dominated by vegetation and lichen (refer to Figure 4.7C and D), and are thus, poorly mapped using imagery. Lichen rock mixture 2 correlates with unit 3 (leucodiorite, tonalite) and shows additional regions to the centre-left and top right corner, indicating that this unit is more prominent within the metasediments. The predictive map also highlights the documented interlayered nature of units 3 and 5 (dominantly psammite) (St-Onge et al., 1999).

The predictive map shows small outcrops of peridotite in the bottom half of the study area, which mimics the distribution of unit 6 (peridotite, dunite). In the top part of the study area, the predicted distribution of peridotite is greater than that of the existing map. This is not to be confused with exposures of unit 4 (gabbro) in the same area.

Unit 7 (carbonate) occurs in only one location in the existing map, but is more spatially extensive in the predictive map, specifically in the bottom third of the study area. The iron oxide/hydroxide weathering is not part of the published map and occurs in spatial association with the metasediments and quartzofeldspathic intrusive rocks.

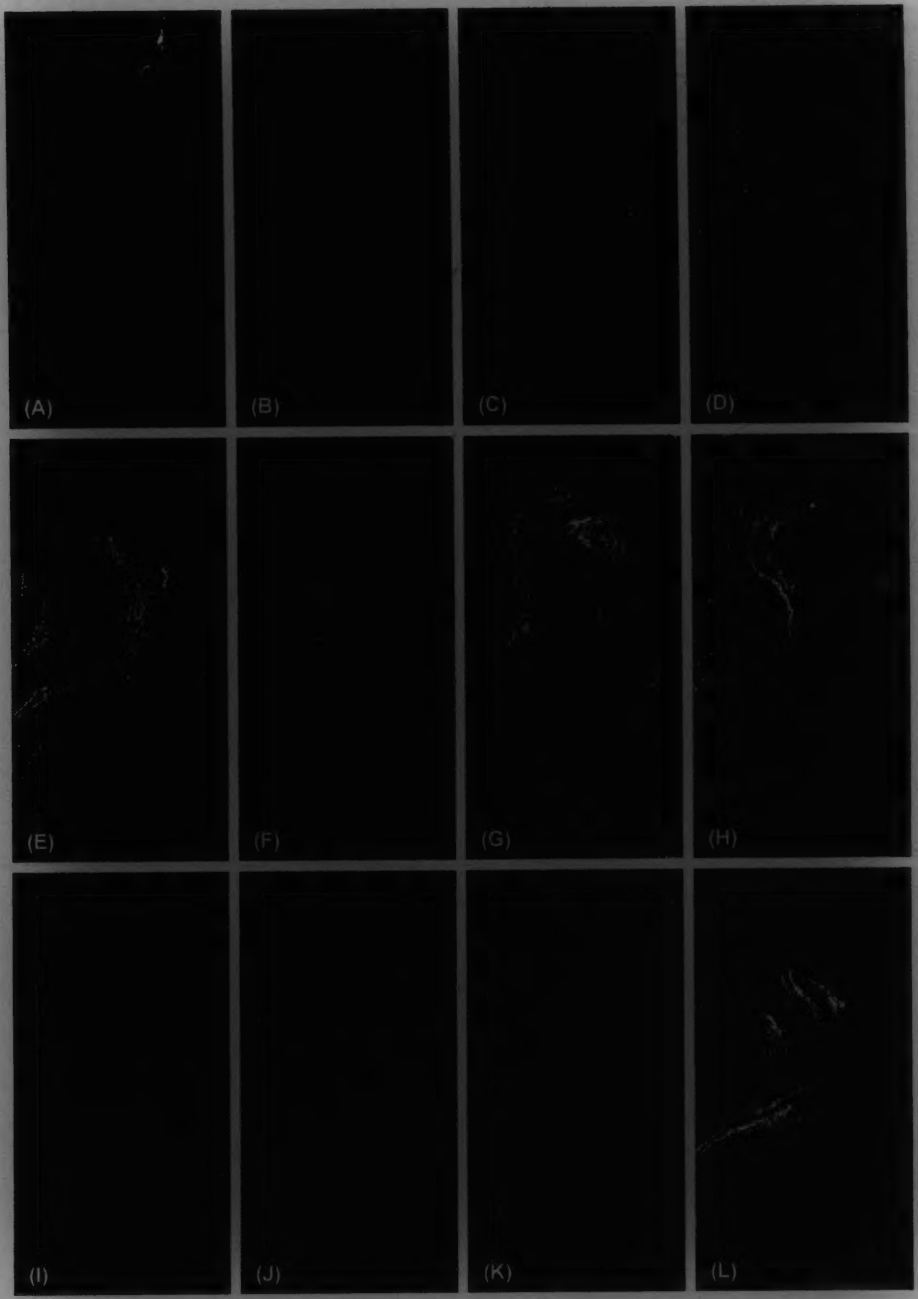

Figure 4.8 Fractional abundance maps for peridotite 1 and 2 (A, B), Fe oxide/hydroxide (C), varnish (D), metased 1 - 3 (E - G), c.g. quartzite/granite (H), carbonate 1 and 2 (I, J), and lichen-rock mixtures 1 and 2 (K, L) endmembers. Black – low abundance; white – high abundance. Images are linearly scaled to best show abundance variation and spatial distribution.

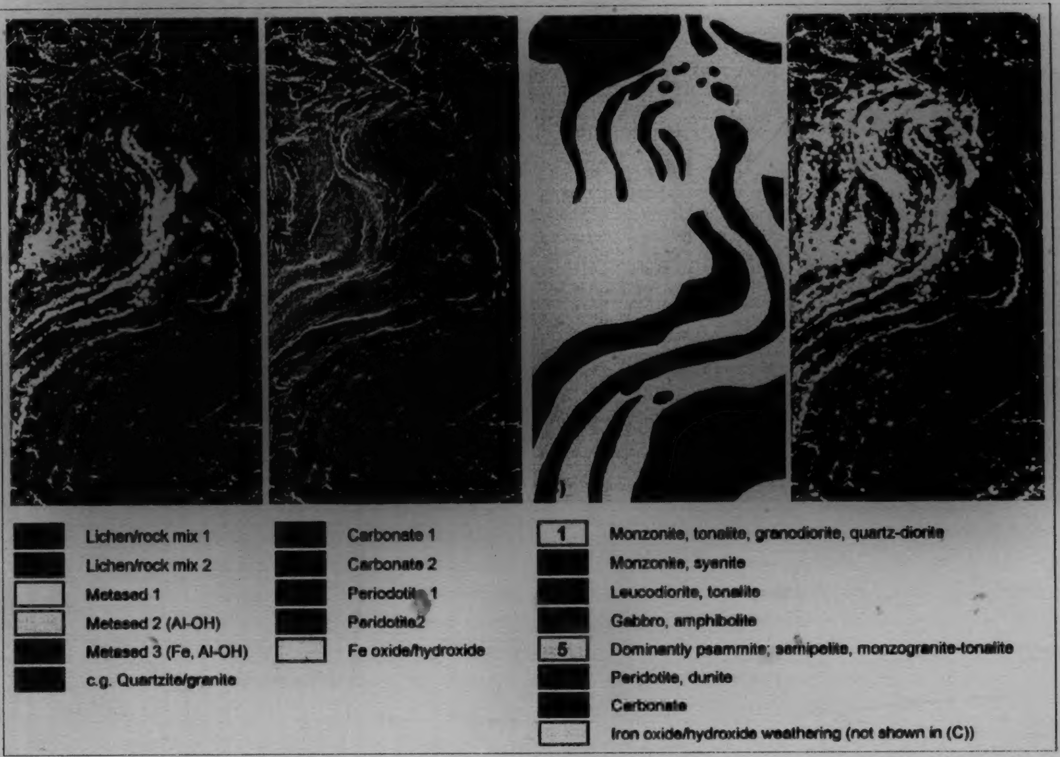
Lichen/rock mix 1
Lichen/rock mix 2
Metased 1
Metased 2 (Al-OH)
Metased 3 (Fe, Al-OH)
c.g. Quartzite/granite
Carbonate 1
Carbonate 2
Periodotite 1
Peridotite2
Fe oxide/hydroxide
1
Monzonite, tonalite, granodiorite, quartz-diorite
Monzonite, syenite
Leucodiorite, tonalite
Gabbro, amphibolite
5
Dominantly psammite; semipelite, monzogranite-tonalite
Peridotite, dunite
Carbonate
Iron oxide/hydroxide weathering (not shown in (C))

Figure 4.9 Predictive geological map showing all eleven geological endmember units (A); units of economic interest shown separately (B); the existing 1:100 000 geological map (St-Onge et al., 1999) (C); and, (D) predictive map with units grouped for comparison with the existing 1:100 000 geological map (e.g. metased 1, 2, 3, and c.g. quartzite/granite grouped into 1 unit representing the psammite, semipelite, monzogranite-tonalite unit (yellow)).

4.6Discussion

4.6.1 Quality of geological endmembers

This study has expanded the list of geological endmembers presented by Harris et al., (2005) to include subtle spectral variability in the metasediments, lichen-rock mixtures that correlate with quartzofeldspathic units, and three endmembers of economic interest, namely the carbonates, peridotites and the iron-oxide/hydroxide endmembers. Overall, a good correlation was observed between the derived geological image endmembers and spectra of corresponding bedrock and samples measured in the field and laboratory. Absorption features associated with Fe, CO_3, Fe-OH, Al-OH, and Mg-OH, allowed for ease in endmember extraction and identification. The good spectral matches indicate that the image endmembers are relatively pure and have geological relevance, increasing the mapping value of the predicted abundance maps. Rock units dominated by quartz and feldspar show little or no diagnostic features in the 500 – 2500 nm range

(Hunt and Salisbury, 1971) and thus, their separation was not possible (e.g. coarse-grained granite/quartzite endmember). It appears that, at least for this study area, one can obtain reasonable spectral representations of most rock units from imagery acquired at a spatial resolution of 7 m.

4.6.2 Lichen and mixtures as endmembers

It is perhaps surprising that one image endmember provided a good match with published spectra (Bechtel et al., 2002) and field spectra of rock encrusting lichens (Figure 4.6), implying that bedrock surfaces can be completely covered by lichen over surfaces exceeding 7x7 m. Having an image endmember for lichen removes the requirement to cross calibrate the image data with field or laboratory spectra of lichen in order to use such spectra for SMA.

The lichen-rock endmembers are partial mixtures with insufficient unique rock spectral information to allow for identification and unmixing of rock and lichen. However, the abundance maps of these endmembers define spatial distributions that are correlative with known rock units, and thus, they can have value for geological mapping. Gabbroic rocks in the study area are covered by thick vegetation and lichen. Harris et al. (2005) noted that vegetation (in this paper vegetation endmember 3) could be used locally as a proxy for the occurrence of gabbro. However, at regional scale vegetation cover crosses multiple lithologic units.

4.6.3 Mapping with abundance fractions

The spectral diversity of endmembers has a direct impact on the resulting endmember fractional abundance maps. Generally endmembers that include diagnostic spectral features results in well-defined abundances with minimal confusion with other endmembers. The minimum fractional abundance threshold that determines the dominant per-pixel geological endmember for the predictive map is a subjective process. The spatial extent of the endmember abundances varies with the threshold value used. This step is followed by an extrapolation of the mapped units to fill the gaps between clusters of labeled pixels. The later task has been automated and is designed to mimic extrapolation between field traverses during traditional mapping. However, the input parameters used to control the growth of the labeled pixels, particularly the number of growing iterations, are also somewhat subjective. Reducing the subjectivity of these decisions remains a topic of research aimed at improving the accuracy of the predictive maps. This study illustrates valuable and reliable predictive mapping information can be achieved despite these limitations.

4.6.4 Spectroscopic imaging

Predictive maps generated from spectroscopic imaging provide a continuous mapping coverage at a detailed spatial resolution. Consequently it is feasible to map outcrops that are of interest for exploration but sufficiently sparse and small to be missed during regional field mapping (e.g. 1-2 km traverse spacing). The improved detail is an outcome of the spatial resolution of the image and the sensitivity of the sensor to detect subtle variability in spectral information. The use of hyperspectral data has the advantage to allow the user to generalize the map information for regional mapping (e.g. Figure 4.9D) as is shown in the published map (Figure 4.9C), but also easily revert to the level of detail available at the resolution of the sensor (Figure 4.9A and B). This is illustrated in the predictive map by the intricate interlayered nature of the clastic metasedimentary and tonalite units.

4.6.5 Economic context

The application of hyperspectral imaging to mineral exploration typically targets the detection of alteration indicator minerals. With the exception of the iron oxide/hydroxide endmember this study has focused on mapping bedrock geology revealing a more extensive distribution of peridotite and carbonate outcrops than shown on published maps. The successful extraction of quality endmembers has allowed the identification and mapping of these units. There are suggestions in the data that sub units of peridotites and carbonates can be defined on spatial and spectral grounds but whether these have geological or exploration significance has not yet been assessed by fieldwork. The occurrence of iron-alteration within the metasediments and in some cases within the quartzofeldspathic unit indicates that the iron-alteration is not randomly distributed, but constrained to specific horizons.

4.7 Conclusions

There exist a limited number of geological mapping studies using hyperspectral data in the Arctic environment. This study has demonstrated the useful application of hyperspectral data for generating accurate predictive geological maps in this type of environment. The ability to capture the spectral diversity related to the bedrock geology, and not just mineral mapping, is evident and consequently the resulting predictive maps are comparable with the published 1:100 000 geological maps. This work was particularly successful at mapping the potentially economic peridotite and carbonate units.

The Arctic environment is known for extensive lichen cover, which is a challenge for remote mapping. This study has shown that a lichen endmember can be extracted from the image and compares well with lichen spectra measured in the field and in the laboratory. This lichen image endmember can be successfully integrated into the unmixing process to produce abundance maps of lithologies that are the building blocks of the predictive map. Quartzofeldspathic rocks, which commonly have a high percentage of lichen cover, were successfully mapped using lichen-rock endmembers derived from the image.

REFERENCES

Adams, J.B., Smith, M.O., & Johnson, P.E. (1986). Spectral mixture modeling: a new analysis of rock and soil types at the Viking Lander 1 site. *Journal of Geophysical Research*, 91, 8098-8112.

Adams, J.B., Smith, M.O., & Gillespie, A.R. (1993). Imaging spectroscopy: Interpretation based on spectral mixture analysis, In: C.M. Pieters & P.A. Englert (Eds.), *Remote Geochemical Analysis: Elemental and Mineralogical Composition,* Cambridge University Press, Cambridge, 145-166.

Asner G.P., & Heidebrecht, K.B. (2002). Spectral unmixing of vegetation, soil and dry carbon cover in arid regions: comparing multispectral and hyperspectral observations. *International Journal of Remote Sensing*, 23, 3939-3958.

Bechtel, R., Rivard, B., & Sanchez-Azofeifa, A. (2002). Spectral properties of foliose and crustose lichens based on laboratory experiments. *Remote Sensing of Environment*, 82, 389-396.

Bierwirth, P., Blewett, R., & Huston, D. (1999). Finding new mineral prospects with HYMAP: early results from a hyperspectral remote-sensing case study in the west Pilbara, *AGSO Research Newsletter*, 31, November.

Bierwirth, P., Huston, D., & Blewett, R. (2002). Hyperspectral mapping of mineral assemblages associated with gold mineralization in the Central Pilbara, Western Australia. *Economic Geology*, 97, 819-826.

Blount, G., Smith, M.O., Adams, J.B., Greeley, R., & Christensen, P. R. (1990). Regional Aeolian dynamics and sand mixing in the Gran Desierto: Evidence from Landsat Thematic Mapper images. *Journal of Geophysical Research*, 95, 15463-15482.

Clark, R.N., King, T.V.V., Klejwa, M., & Swayze, G.A. (1990). High spectral resolution reflectance spectroscopy of minerals. *Journal of Geophysical Research*, 95, 12653-12680.

Clark, R.N., Swayze, G.A., Gallagher, A.J., King, T.V.V., & Calvin, W.M. (1993). The U. S. Geological Survey, Digital Spectral Library: Version 1: 0.2 to 3.0 microns. *U.S. Geological Survey,* Open File Report 93-592.

Clark, R.N., Swayze, G.A., Livo, K.E., Kokaly, R.F., Sutley, S.J., Dalton, J.B., McDougal, R.R., & Gent, C.A. (2003). Imaging spectroscopy: Earth and planetary remote sensing with the USGS Tertracorder and expert systems. *Journal of Geophysical Research*, 108(E12), 5-1 to 5-44.

Crowley, J.K. (1986). Visible and near-infrared spectra of carbonate rocks: reflectance variations related to petrographic texture and impurities. *Journal of Geophysical Research,* 91(B5), 5001-5012.

Crowley, J.K. (1993), Mapping playa evaporate minerals with AVIRIS Data: A first report from Death Valley, California. *Remote Sensing of Environment*, 44, 337-356.

Dillon-Leitch H.C.H., Watkinson, D.H., & Coats, C.J.A. (1986). Distribution of platinum-group elements in the Donaldson West Deposit, Cape Smith Belt, Quebec. *Economic Geology*, 81, 1147-1158.

Duke, E.F. (1994). Near infrared spectra of muscovite, Tschermak substitution, and metamorphic reaction progress: Implication for remote sensing. *Geology*, 22, 621-624.

Griffiths, P.S., Curtis, P.A.S., Fadul, S.E.A., & Scholes, P.D. (1987). Reconnaissance geological mapping and mineral exploration in northern Sudan using satellite remote sensing. *Geology Journal*, 22, 225-249.

Harris, J.R., Rogge, D.M., Hitchcock, R., Ijewliw, O., & Wright, D. (2005). Mapping lithology in Canada's high Arctic: Application of Hyperspectral Data using the Minimum Noise Fraction Transformation and Matched Filtering. *Canadian Journal of Earth Sciences*, 42, 2173-2193.

Heinz, D.C., & Chang, C-I. (2001). Fully constrained least squares linear spectral mixture analysis method for material quantification in hyperspectral imagery. *IEEE Transactions on Geoscience and Remote Sensing*, 39, 529-545.

Hunt, G.R., & Salisbury, J.W. (1971). Visible and near-infrared spectra of minerals and rocks, II, Carbonates. *Modern Geology*, 2, 23-30.

Hunt, G. R. (1977). Spectral signatures of particulate minerals in the visible and near infrared. *Geophysics*, 42, 501-513.

Hunt, G.R., & Evarts, R.C. (1981). The use of near-infrared spectroscopy to determine the degree of serpentinization of ultramafic rocks. *Geophysics*, 46, 316-321.

Kaufmann, H., (1988). Mineral exploration along the Aqaba-Levant structure by use of TM data; concepts, processing, and results. *International Journal of Remote Sensing*, 9, 1639-1658.

Keshava, N., & Mustard, J.F. (2002). Spectral unmixing. *IEEE Signal Processing Magazine*, January, 44-57.

King T.V.V., & Clark, R.N. (1989). Spectral characteristics of chlorites and Mg-serpentines using high-resolution reflectance spectroscopy. *Journal of Geophysical Research*, 94, 13997-14008.

Kruse, F. A., Kierein-Young, K.S., & Boardman, J.W. (1990). Mineral mapping at Cuprite, Nevada with a 63 channel imaging spectrometer. *Photogrammetric Engineering and Remote Sensing*, 56, 83-92.

Kruse, F. A., Lefkoff, A. B., Boardman, J. B., Heidebrecht, K. B., Shapiro, A. T., Barloon, P. J., & Goetz, A. F. H. (1993) The Spectral Image Processing System (SIPS) - Interactive Visualization and Analysis of Imaging spectrometer Data. *Remote Sensing of Environment*, 44, 145 - 163.

Lewry, J.F., & Stauffer, M.R. (1990). The early Proterozoic Trans-Hudson Orogen of North America. *Geological Association of Canada*, Special Paper, 37.

Loughlin, W.P. (1991). Principal component analysis for alteration mapping. *Photogrammetric Engineering and Remote Sensing*, 57, 1163-1169.

Murphy, R.J. (1995). Mapping of jasperiod in the Cedar Mountains, Utah, U.S.A., using imaging spectrometer data. *International Journal of Remote Sensing*, 16, 1021-1041.

Mustard J.F., & Pieters, C.M. (1987). Abundance and distribution of ultramafic microbreccia in Moses Rock dike - Quantitative application of mapping spectroscopy. *Journal of Geophysical Research*, 92, 10376-10390.

Neville, R.A., Staenz, K., Szeredi, T., Lefebvre, J., & Hauff, P. (1999). Automatic Endmember Extraction from Hyperspectral Data for Mineral Exploration. *Fourth International Airborne Remote Sensing Conference and Exhibition / 21st Canadian Symposium on Remote Sensing*, Ottawa, Ontario, Canada, 21-24 June.

Neville, R.A., Levesque, J., Staenz, K., Nadeau, P., Hauff, P., & Borstad, G.A. (2003). Spectral unmixing of hyperspectral imagery for mineral exploration: comparison of results from SFSI and AVIRIS. *Canadian Journal of Remote Sensing*, 29, 99-110.

Podwysocki, M.H., Segal, D.B., & Abrams, M.J. (1983). Use of Multispectral Scanner images for assessment of hydrothermal alteration in the Marysvale, Utah, Mining Area. *Economic Geology*, 78, 675-687.

Rees, W. G., Tutubalina O. V., & Golubeva, E. I. (2004). Reflectance spectra of subarctic lichens between 400 and 2400 nm. *Remote Sensing of Environment*, 90, 281– 292.

Rogge, D., Rivard, B., Zhang, J., Feng, J., & Harris, J. (2006). Integration of spatial-spectral information for endmember extraction. *International Association for Mathematical Geology*, 11th International Congress, University de Leige, Belgium, September 3-8.

Rogge, D.M., Rivard, B., Zhang, J., Feng, J (2006). Iterative spectral unmixing for optimizing per-pixel endmember sets. *IEEE Transactions on Geoscience and Remote Sensing*, 44, 3725-3736.

Rowan, L.C., Bowers, T.L., Crowley, J.K., Anton-Pacheco, C., Gumiel, P., & Kingston, M.J. (1995). Analysis of airborne visible-infrared imaging spectrometer (AVIRIS) data of the Iron Hill, Colorado, carbonatite-alkalic igneous complex. *Economic Geology*, 90, 1966-1982.

Rowan, L.C., Simpson, C.J., & Mars, J.C. (2004). Hyperspectral analysis of the ultramafic complex and adjacent lithologies at Mordor, NT, Australia. *Remote Sensing of Environment*, 91, 419-431.

Sabins, F.F. (19[illegible]9). Remote sensing for mineral exploration. *Ore Geology Reviews*, 14, 157-183.

Sabol, D.E., Adams, J.B., & Smith, M.O. (1992). Quantitative sub-pixel spectral detection of targets in multispectral images. *Journal of Geophysical Research*, 97, 2659-2672.

Settle, J.J., & Drake, N.A. (1993). Linear mixing and the estimation of ground cover proportions. *Inernational Journal of Remote Sensing*, 14, 1159-1177.

Smith, M.O., Jonhson, P.E., & Adams, J.B. (1985). Quantitative determination of mineral types and abundances from reflectance spectra using principal component analysis. *Proceedings of the Fifteeth Lunar and Planetary Science Conference, Part 2, Journal of Geophysical Research*, 90, Supplement, C797-C804.

Staenz, K., Szeredi, T., & Schwarz, J. (1998). ISDAS - A System for Processing/Analyzing Hyperspectral Data; Technical Note. *Canadian Journal of Remote Sensing*, 24, 99-113.

St-Onge, M.R., & Lucas, S.B. (1994). Controls on the regional distribution of iron – nickel – copper – platinum-group element sulfide mineralization in the eastern Cape Smith Belt, Quebec. *Canadian Journal of Earth Sciences*, 31, 206-218.

St-Onge, M.R., Wodicka, N., & Lucas, S.B. (1999). Geology of McKeller Bay-Wight Inlet – Frobisher Bay area, southern Baffin Island, Northwest Territories. *Current Research*, 1998-C, Geological Survey of Canada, 43-53.

St-Onge, M.R., Wodicka, N., & Scott, D.J. (2002). Review of crustal architecture and evolution in the Ungava Peninsula – Baffin Island area: connection to the lithoprobe ECSOOT transect. *Canadian Journal of Earth Sciences*, 39, 589-610.

Sultan, M., Arvidson, R.E., Sturchio, N.C., & Guiness, E.A. (1987). Lithologic mapping in arid regions with Landsat Thematic Mapper data: Meatiq dome, Egypt. *Geological Society of America Bulletin*, 99, 748-762.

Vitorello, I., & Galvao, L.S. (1996). Spectral properties of geologic materials in the 400- to 2500 nm range: Review for applications to mineral exploration and lithological mapping. *Photo-Interpretation*, 2, 77-96.

Yang, K., Huntington, J.F., Boardman, J.W., & Mason, P. (1999). Mapping hydrothermal alteration in the Comstock mining district, Nevada, using simulated satellite-borne hyperspectral data. *Australian Journal of Earth Sciences*, 46, 915-922.

Zamudio, J.A. and Atkinson, W.W. Jr. (1990). Analysis of AVIRIS data for spectral discrimination of geologic materials in the Dolly Varden Mountains, Nevada. *JPL AVIRIS Workshop Proceedings*, 162-166.

CHAPTER 5
CONCLUSIONS

5.1 Summary and Contributions

This thesis has explored the feasibility of applying spectral mixture analysis (SMA) (Adams et al., 1986; Adams et al., 1993) to hyperspectral data for mapping geology in the Canadian Arctic. This work has been, in part, a collaboration with the Geological Survey of Canada, with the goal of developing methodologies that can improve and assist regional geological surveys in the Arctic. The application of SMA was chosen as it allows the user to obtain sub-pixel information which allows for a more accurate representation of the distribution of geological materials in areas where vegetation and particularly lichen, can dominate each pixel spectra.

Three key research themes were explored in this thesis. The first was the integration of spatial, as well as, spectral information in the search for image endmembers, where these endmembers can then be used to identify the rock types and map their distribution. Next was an analysis of the unmixing procedure, with the goal of improving the accuracy of the abundance fractions for each endmember by optimizing the endmember set on a per-pixel basis. The last part of this thesis addressed a more practical problem, namely the generation of a predictive lithological map from the abundance fractions and an assessment of image endmembers in relation to field and sample spectral, thin section and XRD data.

The research presented in Chapters 2 through 4 address 3 independent problems and together provides the necessary tools to transform imagery to a predictive lithological map. Thus, this thesis has advanced the analysis of hyperspectral imaging data for lithological identification and mapping in the Canadian Arctic. The principle contributions of this thesis are summarized below.

1) The first step of applying SMA to hyperspectral imagery is the selection of endmembers. The search for image endmembers has been primarily approached from a spectral standpoint (e.g. Boardman et al., 1995; Bateson and Curtiss, 1996; Winter, 1999; Bowles et al., 1995; Ifarraguerri and Chang, 1999; Neville et al., 1999; Berman, et al., 2004; Nascimento and Dias, 2005; Chang and Plaza, 2006), ignoring the spatial characteristics of the endmembers. This has particular consequences for geological mapping, because spectrally similar endmembers may be treated as a single endmember, when in fact they represent spatially independent regions of the scene and possibly distinct lithological units. Limited studies have made use of both spectral and spatial information (e.g. Plaza et al., 2002) in the search for image endmembers. In Chapter 2 a new spatial-spectral endmember extraction tool (SSEE) was presented and evaluated using two real hyperspectral data sets. Unlike the approach developed by Plaza et al (2002), which uses a morphological approach, SSEE uses spatial neighborhoods to accomplish two key tasks: 1) selecting a set of eigenvectors that relate to both high (spectrally distinct) and low (spectrally similar) contrast endmembers; and, 2) average only spectrally similar endmembers that are also spatially related. The results from this work showed that SSEE was successful in extracting physically significant endmembers with subtle spectral distinctions that were not selected by other well known spectral-based methods. This has important consequences, for the search of endmembers

representative of all geological materials within a given region and is critical for producing accurate geological maps, which in turn, allows for a better interpretation of the given area.

2) Once a set of endmembers has been selected for a region they can be used to unmixed each pixel and generate a set of fractional abundance maps. Common unmixing algorithms make use of the complete endmember set to unmix each pixel within the scene. However, this can cause errors in abundance fractions, because many of the endmembers do not occur within the given pixel (Heinz and Chang, 2001; Sabol et al., 1992). For mapping purposes, incorrect fractions lead to errors in the spatial distribution of geological materials, complicating map genertation. Adapting linear SMA to account for variability in the number of endmembers on a per-pixel basis was the focus of the ISMA approach developed in Chapter 3. The ISMA integrates an iterative approach to unmixing discussed in Ramsey and Christensen (1998) and the change in residual error as a function of endmembers as noted in papers by Roberts et al (1998), Okin et al (1999), Li and Mustard (2003), Roberts et al (2003), Okin et al (2001), Painter et al (2003), and Dennison and Roberts, (2003). Tests using ISMA on simulated data showed that the approach reduced errors in fractional abundance compared with other published unmixing methodologies. ISMA was also shown to produce physically realistic abundance fractions for real hyperspectral data, where imposing constraints on the unmixing process (fractions sum to 1 and non-negative) to obtain physically realistic solutions is not a necessity if an accurate per-pixel endmember set is used. The end result is a novel approach to unmixing that produced more accurate abundance fractions, which in turn, can significantly impact the ability to map the spatial distribution of endmembers of geological interest.

3) The SSEE and ISMA methodologies developed in Chapters 2 and 3 were subsequently applied to hyperspectral data of an area in southern Baffin Island, with the resulting fractional abundance maps used to generate a predictive lithological map. The study area was chosen as it comprises a diverse selection of rock types and represents a typical Arctic environment with extensive lichen cover, which is a challenge for remote mapping. This work included the field sampling and collection of spectra that were considered representative of the regional geology. Comparison of the image endmembers with field and laboratory spectra showed that, at least for this study, one can obtain reasonable spectral representations of most rock units from the imagery, which was acquired at a spatial resolution of 7 m. This allowed for the identification of most endmembers from a comparison with field spectra and analysis of key absorptions features. However, quartzofeldspathic rocks, which show little or no diagnostic features in the 500 – 2500 nm range (Hunt and Salisbury, 1971), were more problematic as these rocks have extensive lichen-coatings. Image analysis identified a lichen endmember that compares well with lichen spectra measured in the field and the laboratory (e.g. Bechtel et al., 2002) and a set of endmembers that were termed lichen-rock mixtures. These endmember spectra had insufficient unique rock spectral information to allow for identification, but the abundance maps defined spatial distributions that are correlative with the known distribution of quartzofeldspathic units in the study area. The predictive lithological map generated from the fractional abundance maps was shown to

successfully capture the spectral diversity related to the bedrock geology and map their spatial distribution in high detail. The resulting map also shows a more extensive distribution of potentially economic peridotite and carbonate rock units as compared with the published 1:100 000 geological maps of St-Onge et al (1999).

5.2 Avenues for future work

Opportunities for future research related to work conducted in this thesis include the optimization of ISMA and SSEE, and the application to other hyperspectral data sets. For optimization, the subset size in SSEE could be determined using methods such as semi-variograms or quadtree decomposition to reflect better the spatial complexity and homogeneity within a given scene. Quadtree decomposition would allow for subsets of different sizes and shapes, thus minimizing the total number of subsets and resulting eigenvectors. For ISMA, a spatial component that could be used to improve the optimization of the per-pixel endmember sets if one assumes that adjacent pixels will likely share common endmembers. Thus, for spectrally similar endmembers that are spatially independent, comparing the optimized endmember set with the local surrounding can reduce errors in the spatial distribution of those endmembers. There are also other opportunities to reduce the number of user defined input variables. In the case of SSEE the number of averaging iterations used to collapse spectrally and spatially similar candidate endmember spectra to a single spectrum could be controlled by the spectral variance between them, rather that a finite number. For ISMA the ΔRMS value that determines the critical point and the optimal per-pixel endmember set could also be linked to the statistical parameters of the RMS curves for all mixtures. This would allow the algorithm to define a ΔRMS value that takes into account such parameters as absolute change. Meaning that a percent ΔRMS for one mixture may not necessarily be effective for another.

Applying SSEE, ISMA, and the generation of predictive maps to other hyperspectral data sets presents an important opportunity to test the robustness of the methodologies under different scenarios. These algorithms have been applied to data sets that could be significantly smaller than that of a regional mapping project. Thus, there is subsequent work necessary to adapt SSEE and ISMA to run on these larger data sets effectively and efficiently. It would be particularly interesting to apply SSEE and ISMA to studies that are non geological in their focus, such as vegetation/canopy studies. For vegetation/canopy studies intra-species spectral variability caused by factors such as leaf maturation and senescence, and water and nutrient stresses could cause significant confusion for species recognition using hyperspectral data (Cochrane, 2000). If the influence of these factors is spatially controlled, SSEE may be particularly useful to identify endmembers for species with respect to local regions where the intra-species variability may be minimal. As for the application of ISMA the key problem is that mixing in these forest environments is likely non-linear. How ISMA will perform requires further tests.

REFERENCES

Adams, J.B., Smith, M.O., & Johnson, P.E. (1986). Spectral mixture modeling: a new analysis of rock and soil types at the Viking Lander 1 site. *Journal of Geophysical Research*, 91, 8098-8112.

Adams, J.B., Smith, M.O., & Gillespie, A.R. (1993). Imaging spectroscopy: Interpretation based on spectral mixture analysis, In: C.M. Pieters & P.A. Englert (Eds.), *Remote Geochemical Analysis: Elemental and Mineralogical Composition,* Cambridge University Press, Cambridge, 145-166.

Bateson A., and Curtiss, B. (1996). A method for manual endmember selection and spectral unmixing. *Remote Sensing of Environment,* 55, 229-243.

Bechtel, R., Rivard, B., & Sanchez-Azofeifa, A. (2002). Spectral properties of foliose and crustose lichens based on laboratory experiments. *Remote Sensing of Environment,* 82, 389-396.

Berman, M., Kiiveri, H., Lagerstrom, R., Ernst, A., Dunne, R., & Huntington, J.F. (2004). ICE: A statistical approach to identifying endmembers in hyperspectral images. *IEEE Transactions on Geoscience and Remote Sensing*, 42, 2085-2095.

Boardman, J.W. (1993). Automating spectral unmixing of AVIRIS data using convex geometry concepts. *Summaries of the fourth Annual JPL airborne Geoscience Workshop*, JPL Publication 93-26, 1, 11-14.

Bowles, J., Palmadesso, P.J., Antoniades, J.A., Baumback, M.M., & Rickard, L.J. (1995). Use of filter vectors in hyperspectral data analysis. *Proceedings SPIE Infrared Spaceborne Remote Sensing III*, 148-157.

Chang, C-I., & Plaza, A. (2006). A fast iterative algorithm for implementation of Pixel Purity Index. *IEEE Transactions on Geoscience and Remote Sensing Letters*, 3, 63-67.

Cochrane, M.A. (2000). Using vegetation reflectance variability for species level classification of hyperspectral data. *International Journal of Remote Sensing*, 21, 2075-2087.

Dennison, P.E., & Roberts, D.A. (2003). Endmember selection for multiple endmember spectral mixture analysis using endmember average RMSE. *Remote Sensing of Environment,* 87, 123-135.

Heinz, D.C., & Chang, C-I. (2001). Fully constrained least squares linear spectral mixture analysis method for material quantification in hyperspectral imagery. *IEEE Transactions on Geoscience and Remote Sensing*, 39, 529-545.

Hunt, G.R., & Salisbury, J.W. (1971). Visible and near-infrared spectra of minerals and rocks, II, Carbonates. *Modern Geology*, 2, 23-30.

Ifarraguerri, A., & Chang, C-I. (1999). Multispectral and hyperspectral image analysis with convex cones. *IEEE Transactions on Geoscience and Remote Sensing,* 37, 756-770.

Li, L., & Mustard, J. F. (2003). Highland contamination in lunar mare soils: Improved mapping with multiple end-member spectral mixture analysis (MESMA). *Journal of Geophysical Research*, 108(E6), 5053, 7-1 to 7-14.

Nascimento, J.M.P., & Dias, J.M.B. (2005). Vertex component analysis: a fast algorithm to unmix hyperspectral data. *IEEE Transactions on Geoscience and Remote Sensing*, 43, 898-910.

Neville, R.A., Staenz, K., Szeredi, T., Lefebvre, J., & Hauff, P. (1999). Automatic Endmember Extraction from Hyperspectral Data for Mineral Exploration. *Fourth International Airborne Remote Sensing Conference and Exhibition / 21st Canadian Symposium on Remote Sensing*, Ottawa, Ontario, Canada, 21-24 June.

Okin, W.J., Okin, G.S., Roberts, D.A., & Murray, B. (1999). Multiple endmember spectral mixture analysis: endmember choice in an arid shrubland. In: R.O. Green (ed.) *1999 AVIRIS Work*[illegible] JPL, Pasadena, California, 323-332.

Okin, G.S., Roberts, D.A., Murray, B., & Okin, W.J. (2001). Practical limits on hyperspectral vegetation discrimination in arid and semiarid environments. *Remote Sensing of Environment,* 77, 212-225.

Painter, T.H., Dozier, J., Roberts, D.A., Davis, R.E., & Green, R.O. (2003). Retrieval of subpixel snow-covered area and grain size from imaging spectrometer data. *Remote Sensing of Environment,* 85, 64-77.

Plaza, A., Martinez, P., Perez, R., & Plaza, J. (2002). Spatial/spectral endmember extraction by multidimensional morphological operations", *IEEE Transactions on Geoscience and Remote Sensing*, 40, 2025-2041.

Ramsey M.S., & Christensen, P.R. (1998). Mineral abundance determination: Quantitative deconvolution of thermal emission spectra. *Journal of Geophysical Research,* 103, 577-596.

Roberts, D.A., Gardner, M., Church, R., Ustin, S., Scheer, G., & Green, R.O. (1998). Mapping chaparral in the Santa Monica Mountains using multiple endmember spectral mixture models. *Remote Sensing of Environ*ment, 65, 267-279.

Sabol, D.E., Adams, J.B., & Smith, M.O. (1992). Quantitative sub-pixel spectral detection of targets in multispectral images. *Journal of Geophysical Research*, 97, 2659-2672.

St-Onge, M.R., Wodicka, N., & Lucas, S.B. (1999). Geology of McKeller Bay-Wight Inlet – Frobisher Bay area, southern Baffin Island, Northwest Territories. *Current Research*, 1998-C, Geological Survey of Canada, 43-53.

Winter, M.E. (1999) Fast autonomous spectral endmember determination in hyperspectral data. *Proceedings of the Thirteenth International Conference on Applied Geologic Remote Sensing*, Vancouver, B.C., Canada, II, 337-344.